Republic of Iraq

Ministry of Higher Education

and Scientific Research

University of Kerbala

College of Science

Department of Physics

# Preparation and characterization of PbS films doped by Cd and Cr via pulsed laser deposition for gas sensor applications

A Thesis

Submitted to Council of the College of Science

University of Kerbala in Partial Fulfillment of the Requirements for the Degree of Master of Science in Physics

By
**Khudhair Obayes Mahmood**

B.Sc. in Physics (2010-2011)

Supervisors

Assist. Prof .Dr. Majed H. Dwech

Prof. Dr. Kadhim A.adim

2021A.D.

1443 A.H.

بِسْمِ اللَّهِ الرَّحْمَنِ الرَّحِيمِ

(لاَ يُكَلِّفُ اللَّهُ نَفْساً إِلاَّ وُسْعَهَا لَهَا مَا كَسَبَتْ وَعَلَيْهَا
مَا أَكْتَسَبَتْ رَبَّنَا لاَ تُؤَاخِذْنَا إِنْ نَسِينَا أَوْ أَخْطَأْنَا
رَبَّنَا وَلاَ تَحْمِلْ عَلَيْنَا إِصْراً كَمَا حَمَلْتَهُ عَلَى الَّذِينَ مِنْ
قَبْلِنَا رَبَّنَا وَلاَ تُحَمِّلْنَا مَا لاَ طَاقَةَ لَنَا بِهِ وَاعْفُ عَنَّا
وَاغْفِرْ لَنَا وَارْحَمْنَا أَنْتَ مَوْلَنَا فَانْصُرْنَا عَلَى الْقَوْمِ
الْكَفِرِينَ)

صَدَقَ اللَّهُ العلي الْعَظِيمِ

**سورة البقرة: (الايه٢٨٦)**

# Supervisors Certificate

we certify that this thesis, entitled " **Preparation and characterization of PbS films doped by Cd and Cr via pulsed laser deposition for gas sensor applications"** has been prepared under our supervision , by " **Khudhair Obayes Mahmood**" at the department of physics ,College of science, University of Kerbala in a partial fulfillment of the requirements for the degree of Master of Science in physics.

| | |
|---|---|
| Signature: | Signature: |
| Name: Majed H. Dwech | Name: Kadhim A.adim |
| Title: Assist. Prof. Dr. | Title: Prof. Dr. |
| Address: Department of Physics<br>College of science, University of<br>Kerbala | Address: Department of Physics<br>College of science, University<br>of Baghdad |
| Date: 2021 \ \ | Date: 2021\ \ |

In view of the available recommendations, I forward thesis for debate by the examination committee .

Signature :

Name: Dr. Rajaa Abdul Al-Ameer Madlool

Title: Professor

Head of Physics Department, College of Science, University of Kerbala

Data: / / 2021

# Examination Committee Certification

We certify that we have read this thesis entitled " **Preparation and characterization of PbS films doped by Cd and Cr via pulsed laser deposition for gas sensor applications**" as the examining committee, examined the student " **Khudhair Obayes Mahmood** " on its contents, and that in our opinion, it is adequate for the partial fulfillment of the requirements for the Degree of Master in Science of Physics.

Signature:
Name: **Dr.** Ahmed Mehmood Abdul-Lettif
Title: **professor**
Address: Department of physics, college of science/University of Kerbala
Date: / / 2021
**(Chairman)**

Signature:
Name: **Dr.** Uday Muhsin Nayef
Title: **professor**
Address: Department of Applied science, college of science/University of Technolog
Date: / / 2021
**(Member)**

Signature:
Name: **Dr.** Falah A- H. Mutlak
Title: **Assist. Prof. Dr.**
Address:Department of physics, College of Science, University of Baghdad
Date: / / 2021
**(Member)**

Signature:
Name: **Dr.** Majed H. Dwech
Title: **Assist. Prof. Dr.**
Address: Department of physics, college
science/University of Kerbala
Date: / / 2021
**(Supervisor)**

Signature:
Name: **Dr.** Kadhim A. adim
Title: **professor**
Address: Department of physics, College of Science, University of Baghdad
Date: / / 2021
**(Supervisor)**

Signature:
Name: **Dr.**Jasem Hanoon Hashim Al-Awadi
Title: Assist. Professor
**Dean of the college of science/ University of Kerbala**
Of science

Date: / / 2021

# Dedication

For those who separated us in his body, but his soul still flutters in the sky of my life

My Father

To the spring that never stops giving,

My mother

To those whose love flows in my veins and my heart always remember them,

My wife and children

To those who support me,

My sisters and brothers

For those who encourage and support me

My Friends

Khudhair

# *Acknowledgements*

*First of all , I thank God for helping me to complete this thesis , and best prayers and peace on his best messenger Mohammed , his pure descendants and his noble companions.*

*I would like to express my sincere appreciation and deep gratitude to my supervisors, Asst. Prof. Dr. Majed Hussein. and Prof. Dr. Kadhim A.adim, for suggesting the topic of this thesis, guidance, advice and continuous encouragement throughout the research. My thanks go to all the staff members of the department of physics University of Karbala .I could hardly find any words to express my sincere gratitude to the staff of the plasma laboratory ,in the department of physics, college of science, university of Baghdad .*

*I wish I had a better word than thanks for expressing my feelings to mother for their patience and unlimited support with my brothers, sisters and friends for their prayers and kindness.*

# Abstract

In this work, cadmium-chromium-doped(X=2,4,6)Wt% lead sulfide PbS thin films were deposited on a glass substrate at room temperature by means of a pulsed laser deposition (PLD) technique. The effect of laser energy and different doping ratios on the structural and optical properties of PbS films were studied using Nd:YAG laser with different laser energies from (200 – 350) mJ in increments of 50 mJ per step. The number of laser pulses was fixedly set to 100 pulses per sample.

The structures of (PbS, PbS:Cd and PbS:Cr) powder and thin films were studied using X-ray diffraction technique. X-ray study showed that the structure is polycrystalline and monoclinic with a preferred orientation plane (200) and that the crystal size increases with increasing laser energy and increases at different doping ratio .

Atomic force microscopic measurements (AFM) confirmed that the films grown by PLD technique have good crystalline and homogeneous surface. The average particle diameter for all prepared films is less than 100 nm ,so it is in the range of nanomaterial's.

The optical measurements were studied using UV-ViS- spectrophotometer. The results showed that the (PbS, PbS:Cd and PbS:Cr) thin films have direct allowed energy gap transition and the absorbance of films increases with the increasing of laser energy and increases at different doping ratio . Also, the optical constants such as the refractive index(n), absorption coefficient (α), extinction coefficient(k) and dielectric constant real and imaginary parts($\varepsilon_r$,$\varepsilon_i$) have been calculated. The energy gap increases with increases of laser energy and increases at different doping ratio (1.5 - 2.8) eV by doping with cadmium and (1.6 -1.8) eV by doping with Chrome.

The gas sensor measurements showed that the best sensor for $NO_2$ gas was for the sample with a percentage of 5% PbS:Cd X = 4% with a sensitivity of 137% at 523 K and the sensitivity of the sample was decreased for PbS and for $NH_3$ gas at an energy of 250 mJ at 523 K to 19%.

# *List of symbol and abbreviations*

| **Symbols and abbreviations** | **Terms** | **Units** |
|---|---|---|
| A | Absorbance | |
| AFM | Atomic Force Microscope | |
| B | Full width at half maximum | Degree |
| PbS | Lead sulfide | |
| Cd | Cadmium | |
| Cr | Chromium | |
| $D_{av}$ | Average crystal size | nm |
| $E_c$ | Conduction band | eV |
| $E_g$ | Optical energy gap | eV |
| $E_V$ | Valence band | eV |
| C.S | Crystallite size | nm |
| hυ | Photon energy | eV |
| K | Wave vector | |
| $k_o$ | Extinction coefficient | |
| $n_o$ | Refractive index | |
| PLD | Pulsed laser deposition | |
| R | Reflectance | |
| t | Thickness | nm |
| T | Transmittane | |
| XRD | X-ray diffraction | |
| hkl | Miller indices | (hkl) |
| $\varepsilon$ | Dielectric constant | |
| $\varepsilon_i$ | Imaginary part of dielectric | |
| $\varepsilon_r$ | Real part of dielectric | |
| $\alpha$ | Absorption coefficient | $cm^{-1}$ |
| $\lambda$ | Wavelength | nm |
| $\Theta$ | Diffraction angle | Degree |

# *Contents*

## Chapter Four :Results and Discussion

# Chapter One

## Introduction and Literature Review

# 1-1 Introduction

Solids are classified according to their electrical conductivity to conductors, insulators, and semiconductors based on the fixation ranges of the material and the amount of energy gap separating the conduction band to the valence band.

Semiconductors are an insulating material at a temperature (0 $K^0$) and have good electrical conductivity when the temperature is raised. Semiconductors are widely used in electronic applications, where they are available in large quantities and their properties are influenced by heat, light and magnetic fields [1,2].

Chalcogenide semiconductors are considered nanoscale as a component of nanotechnology, due to their physical and chemical properties, which depend mostly on their shape and size [3]. It is clear that the chemical composition, shape, and size control the properties of the semiconducting nanomaterials [4]. The nanostructure of the semiconductor exhibits good electrical, photoemagnetic and photochemical properties and differs significantly from those of the micro-bulk materials due to quantum size effects, resulting from a predominant number.Of surface atoms in nanoscale materials [5]. Metal chalcogen transition compounds are important semiconductor materials, especially in nanoscale due to their excellent properties in photoelectronic transformation and potential applications in physics, chemistry, biology, medicine, materials sciences and their various fields such as solar cells, sensitive sensors, and photon computers [6]. Sensors are a type of device that detects or measures physical and chemical quantities such as temperature, pressure, sound, and concentration. and in it, the measurements are converted into an electrical signal through which we know that there is something like a high percentage of gas or the presence of toxic gas, etc. [7].

## 1-2 Thin Film Phenomena

Thin film technology is distinguished because it is one of the most important techniques that contribute to the development of the study of semiconductors. Thin-membrane physics is an important and unique branch of solid state physics that is concerned with the study of materials in general and semiconductors in particular. Thin film technology has effectively contributed to the development of thin films manufacturing processes by giving a clear idea of its physical and chemical properties [8].

Thin films are materials that consist of one or several layers of atoms, the thickness of which is no more than (1 micrometer). It is thin and fragile (easy to break), and must be deposited on solid bases of glass, silicon, polymer and other materials according to the nature of the study [9].

There are many different industrial applications of thin films as they are used in electronic devices in resistors, capacitors, transistors and electronic circuits. All the technologies that people use for electronic devices are accurate and intelligent and the are mainly the result of advances in the field of the thin film industry. Thin films are also involved in the manufacture of solar cells and photoelectric detectors, which operate in a specific range of the electromagnetic spectrum. Also, thin films are mainly used to protect materials from corrosion by coating them with thin films [10]. The development of thin films contributed to their entry into the world of nanotechnology and the study of the properties of materials on the nanometer scale special thin films of nanotechnology[11].

## 1-3 **Lead Sulfide (PbS)**

Lead sulfide is a chemical compound with the formula PbS, which is in the form of a black crystalline powder. The metal, lead sulfide, galena is the main source of lead PbS which has a tiny direct band gap (0.4 eV at ambient temperature) and a high activation Bohr diameter as just an IV–VI semiconducting element combination (approximately 18 nm) [12]. It has a configurable band gap energy, and also high temperature and corrosion resistance. [13] . PbS thin films have been used in the past due to their high response rates, ease of preparation, and stable operation at room temp, they were extensively used in the field of optical and electronic devices [14]. The table (1-1) shows some properties of lead sulfide.

**Table (1-1) some physical and chemical properties of PbS [12].**

| **Property** | **PbS** |
|---|---|
| Lattice constant | a = 5.930 A° |
| Crystal Structure | cubic |
| Appearance | black crystalline powder |
| Density | 7.5 g / $cm^3$ |
| Melting point | 1114 ° C |
| Solubility in water | Insoluble |
| Molecular Mass | 239.28 g / mol |
| Conductivity type | n-type |

## 1-4 Cadmium (Cd)

A silver-white metallic element that is easily ductile and knocked[15], with chemical symbol Cd, atomic number 48; Its atomic weight is 112.411. It is one of the transition elements in Group 12 (or IIB) of the periodic table[16].
Cadmium was discovered in 1817 by German pharmacist Friedrich Stroemier. This element is described by the number sixty-fifth in terms of its natural presence in the earth's crus[17]. Cadmium has a melting point of 321C ° .Its boiling point is 764.85 C ° , and its density is 8.64 grams / cm$^3$. When cadmium is heated, it combusts in atmospheric air with incandescent light, forming CdO oxide[18]. The highest form of the main constituent is a rare mineral known as greenocite[19]. It can also be obtained from a zinc ore mineral known as silisa. The method of electrolysis or fractional distillation is used to separate cadmium from zinc. Cadmium can be electrostatically deposited on some other metals such as iron or steel, forming a layer that is resistant to chemical changes[20]. It forms alloys with lead and bismuth for the manufacture of metal fuses used in fire alarm systems and electrical fuses[21].

## 1-5 Chromium (Cr)

It is important mineral chemical, among its general characteristics. It carries the symbol (Cr), the atomic number (24),density 7.19 g/cm$^3$ ,melting point1907C° it is gray or silver in color, and has a metallic luster[22]. It was discovered in the eighteenth century, and its use was famous in the nineteenth century and beyond, as chromium was used in many uses and industries. The most important features of Cr are prevention of rust, corrosion and heat for many metals[23]. Chromium is the first element of the sixth group, located to the left of the periodic table of elements. This group is one of the groups of transition metallic elements[24]. Chrome is a rapidly oxidizing element in the event of exposure to the open air, as an outer layer of chromium oxides is formed around it that insulates the rest of the internal metal from the air[25]. Chromium is extracted from chromite ore found in igneous rocks, and chromium is also present in small proportions in many foods, including: meat, liver, eggs, cheese, and whole grains: such as wheat[26]. Brown rice, corn, and others, and chromium is also found in potatoes, Nuts, and others[27]. Chromium is used in many fields, including: the manufacture of many metals and improving their resistance to corrosion and rust, such as: the manufacture of non-oxidation steel[28]. Chromium is used in leather tanning, and leather tanning: it is treated with some materials that purify it, remove moisture, stink and hair and prepare them for use. Chromium is used to color glass, and this is done by some salts extracted from it[29].

## 1-6 Literature Review

**Abbas *et al*. (2011)[30]** prepared PbS nano films which were deposited on glass substrates using chemical bath technique of different degrees,at different solution temperatures and sedimentation times. Film thickness was in the order of 600– 1000 nm. The crystal structure and size of these films were studied by X-ray diffraction. The optical properties, absorption, transmission and reflection were measured as a function of thickness. The influence of heat treatment under different annealing temperatures on the optical properties of some precipitates films has been studied and analyzed.

**Pawar *et al.* (2011)[31]** studied the chemosynthesis of nanocrystalline lead sulphide (PbS) thin films onto soda-lime glass substrates that used an easy and price chemically bath deposit (CBD) method. The formation of PbS with cubic crystal structure is visible in the X-ray diffraction (XRD) image. X-ray photon spectrometry was used to investigate the electrical structures and chemical states of PbS films (XPS). With the increase in deposition duration from 20 to 90 min, fields fluorescence transmission electron microscope (FESEM) images reveal the change from granularto- cubic-to-cubo-octahedra similar surface morphology. The UV–vis–NIR absorption spectra of PbS thin films were measured, and the energy band energy was calculated to use a classic photon energy approach. Quant strength value is seen in the rise in bandgap between 0.99 to 2.06 eV as crystallographic area is smaller. This work showed how to deposit PbS nanostructured thin films with dominant magnetic properties and use an easy and efficient solution approach. This technique may be helpful in micro sensitive oxide-based solar cells, which have recently also been subject of extensive interest.

**Bandyopadhyay *et al. (*2012)[32]** studied gas sensors of lead sulplide (PbS). The dopant PbS nanocrystals composite was obtained using the sol-gel process at two distinct reaction temperatures (60C and 90C) and they studied the structural properties using x-ray diffraction (XRD) and scanning electron microscopy (SEM). XRD results showed crystallite sizes of 17.81 nm and 14.5 nm, respectively. SEM analysis of produced PbS material showed a coagulated crystal structure. At different temperatures, the behavior of such substances was studied in the presence of moisture vapor, as well as various other gasses and fumes of solvents (25C to 90C). At ambient temperature, experimental gas sensors behaviour showed that the synthesized nanocrystals nanomaterials are influenced primarily by $NH_3$ and $NO_2$, among many other gases.

**Das *et al.* (2012)[33]** studied the chemical deposition technique. Nano - crystalline PbS and Sn enriched PbS films were successfully deposited on a suitably clean glass plate at steady room temp. The pure PbS thin films were deposited at room temperature for many dip cycles prior introducing Sn doped content to maximize the deposition time. The films were also annealed in oxygen for 10 minutes following deposit at 400 C°. X-ray diffract studies have been used to identify the crystalline structure of the film. The films were very well adherent to a surface and crystallized in a cubic form with a preferred orientation [200]. The crystallite size of pure PbS thin films was determined to be 40.4 nm at an optimized deposit time of 30 minutes, and increased with Sn content in pure PbS thin films. AFM studies were used to determine the surface roughness. SEM micrographs have been used to estimate the band - gap of the film. Studies indicated that the crystallite size and optical properties of the film are influenced on mycelial growth such as doping and heating.

**Sadovnikov *et al.* (2013)[34]** studied the crystalline structure of lead sulfide thin films produced by chemical activation from aqueous systems on a glass plate. Movies produced with PbS was shown to be analyzed. It has a cubic crystal structure (space group Fm3m) D03, which is not the same as type B1. Electron inspection of the microstructure of a film showed that almost half of all particles have a size of 60 nm or smaller. The photonic transportation of PbS happens in the spectrum range of 300 to 3200 nm. The thickness of submicron films with such a D03 significantly increased from 120 to 400 nm are determined. Whenever the mean size of the nanoparticles in PbS films is decreased, the energy band gap energy increases from 0.85 to 1.5 eV. These band gap energy values are greater than the 0.41 eV bandgap of wear resistant PbS. Witness The absorbance shift in the nano-structured lead sulfide film under investigation is blue.

**Obaid *et al.* (2013)[35]** deposited nanocrystalline PbS thin films on glass substrate from lead nitrate (Pb2+ ions) and thiourea (S2− ions) precursors using MACB technique. The effects of molar concentration (0.02, 0.05, 0.075 and 0.1 M) on the structure and microstructure evolution were studied using X-ray diffraction (XRD), scanning electron microscopy, and atomic force microscopy. The optical properties were investigated using UV–vis spectrophotometer. Crystal size values obtained from XRD were compared with these calculated using atomic force microscopy (AFM). The values of optical band gaps were found to decrease as the ion source molar concentration increase.

**Göde *et al*. (2014)[36]** prepared PbS films for 100, 115, 130, and 145 minutes in a chemical bath at room temperature, useing the precipitation method. X-ray diffraction is being used to distinguish crystal structures. In such a cubic rock structure, all of films are polycrystalline. Transmission electron microscope ( TEM) has been used to investigate the situation. Absorption, transmittance, and reflectance spectra are all used. Films' optical bandgap was decreased from 2.65eV to 2.50eV.with increasing sedimentation time. Refractive index, extinction, modulus and electrostatic constant were determined. The conductivity of the PbS film increased from 1.791 $10^{-6}$ to 1.655 $10^{-3}$ $(\Omega\ \mathrm{cm})^{-1}$ with the increase of sedimentation time. Thermal gloss is the intensity of films measured after fifteen minutes of irradiation with a source. minutes in temperature and kinetic parameters obtained using Computer glare curve evolution method.

**Kumar *et al. (*2014)[37]** use chemical baths deposit to produce nanocrystals Sb enriched PbS films. After deposition, the films were annealed at 673 K in air for 1 hour. X-ray diffraction (XRD) confirmed the formation of very well PbS with a face-centered crystalline and preferential orientation [200]. Its crystallite size was found to be between 40 and 43 nm. Surface analysis using AFM shows a texture that really is uniform and smooth, with an average grain size of 52.3 nm. The optical characteristics, absorbance, and transmission of the films were calculated as a function of doping. When Sb doping is increased in PbS thin films, the band gap ( $E_g$) decreases from 1.69 eV to 1.59 eV, resulting inside a blue shift of the absorption edge in nanostructured thin films. The films' electrical resistivity at room temperature is found to have a value between (-1.29 and -3.7 $10^6$) Ω cm.

**Niruban *et al*. (2015)[38]** deposited nanocrystalline (Pb1-Mg)Si thin films were successfully deposited on suitably cleaned glass substrate at constant temperature of 60° C, using the chemical bath deposition technique. After deposition the films were annealed at 300°C for 2 hours. The film's structural, morphological and optical properties have been investigated by X-ray diffraction (XRD), scanning electron microscope (SEM) and UV–vis spectrophotometer. X-Ray diffraction patterns reveal that all of the films are polycrystalline cubic in nature with preferential orientation (200). Microstructural parameters like crystallite size, micro strain and dislocation density have been calculated using x-ray line profile analysis. The average crystallite size was found to be between 20.03 and 15.12 nanometers. The films were polycrystalline in nature, with a homogeneous and smooth surface, according to SEM examination. Optical studies revealed the band gap energy for thin films, which increased from (1.54 - 1.66) eV with increased Mg doped samples.

**Rajashree *et al*. (2015) [39]** fabricated crystallinecadmium using the spray pyrolysis technique. Contaminated lead sulphide (PbS:Cd) thin films having different Cd loading levels (0, 2, 4, 6, and 8 at-percent) were fabricated on glass slides. Regardless of Cd carrier level, X-ray diffraction (XRD) studies revealed that all films have a facial cubic structure with a preferred orientation along the (200) plane. Optical studies revealed that the band gap is a major factor. At increased Cd concentration, the optimum permeability of treated films ranges from 1•96 and 2•12 H.cm, and the film covered using 6 at-percent Cd doped has a peak transmittance of nearly equal to 77 percent. As per electrical tests, the film covered with 6% Cd photocatalyst has a maximum conductivity of 12•6710$^{-1}$ $\Omega^{-1}$ cm$^{-1}$. According to the findings, the PbS:Cd film covered with 6% Cd photocatalyst exhibits better structural, morphology, optical, or electronic properties.

**NASIR *et al.* (2016) [40]** used chemical deposition method to successfully prepare nanocrystals thin films of PbS with different thickness (400, 600)nm on glasses and Si substrate. The framework and morphology of these films were studied by X-ray diffraction and atomic force microscope. It shows that the structure is polycrystalline and the average crystallite size has been measured. The electrical properties of these films have been studied, it was observed that D.C conductivity at room temperature increases with the increase of thickness, From Hall measurements the conductivity for all samples of PbS films is p-type carrier's concentration. Mobility and drift velocity increases with increasing of thickness.

**Touati *et al*. (2016) [41]** deposited copper-doped PbS polygonal thin films by chemical bath deposit. X-ray diffraction (XRD), Hutchinson elastic scattering spectroscopy (RBS), atomic force microscopy (AFM), transmission electron microscopy (TEM), X-ray light scattering spectroscopy (XPS), UV–visible–near infrared (UV–Vis–NIR) spectrophotometry, and Hall effect measurements have been used to start investigating the structure, framework, morphological characteristics, optical, and electrical properties of the materials. The dopant films have a PbS face cubic crystal structure to (111) preferential orientation, which alters to (200) plane with increasing Cu doping absorption, as per XRD studies. The film surfaces were found to be made up of nanotubes grains with a triangular form, according to AFM and SEM observations. With the increase in Cu carrier level, the optical band gap blue shifted from ( 0.72 - 1.69 )eV. At ambient temperature, the material with a [Cu2+]/[Pb2+] ratio of 1.5 at 5% Cu had a minimum resistivity of 0.16 Ω cm and a band gap close to 1.5 eV. Percentage of 1.5 the best electrical and optical characteristics are obtained in Cu-doped PbS thin films which are appropriate for the use of solar cells

**Yücel *et al*. (2017) [42]** used chemicals bathtub deposition (CBD) are used for 1 hour sedimentation time and lead sulfide isotope ratios (PbS) nanostructures on glass slides. The structural, morphological, and optical properties of PbS thin films were investigated in relation to Sr doped samples. SEM, X-Ray diffraction (XRD), and UV–visible scope and quality have been used to investigate variations in crystallite size, lattice strain, band gap, and energy band gap values of PbS thin films as a result of Sr content. The findings of an energy - dispersive X-ray analysis (EDSA) showed that nano - structured PbS films can be doped with Sr without causing significant structural strain. By increasing Sr-doping, the crystal size of the film decreases between 17.90 to 9.14 nm, as per XRD studies. Increasing the Sr doped from 0% to 5% raised the energy gap value of PbS thin films from 1.73 eV to 2.19 eV, according to UV–visible measurement.

**Carrasco-Jaim *et al*. (2017) [43]** investigated the photocatalytic hydrogen production from hydrogen production using a PbS/ZnO thin film. Chemical bath depositing of a p-type PbS thin film onto a single crystal was carried on by RF magnetron sputtering of an n-type ZnO thin film. Grazing angle x-ray diffraction (GA-XRD) and atomic force microscopy (AFM) were used to describe the morphological and structural properties, accordingly, while ultra - violet spectroscopy (UV–Vis) and spectroscopic device captures have been used to investigate the optical characteristics .The photocatalytic activity was assessed using chromatography to determine hydrogen production during uv irradiation. The results showed that PbS/ZnO thin films generated more photocatalysts hydrogen (7.38 µ $cm^{-2}h^{-1}$) than PbS (3.35 µ $cm^{-2}h^{-1}$) and ZnO (2.45 µ $cm^{-2}h^{-1}$) thin films. The synergistic impact of PbS and ZnO thin films for the generation and transport of electric charge was shown using linear sweep voltammetry (LSV).

**Kumar *et al*. (2018) [44]** determined the fabrication of PbS solar cells (QDs) using a sol-gel procedure that is efficient, affordable, and scalable over a broad area. Its diameter of a (QDs) can be adjusted by changing the bath levels between (50 and 200)mm. At 50mm bath level, transmission electron microscope (TEM) tests confirm the growth of spherically shaped 5.6 nm QDs. The optical bandgap of the QDs is found to be 0.9 eV, that fits the size reported by TEM. Sensitizing ZnO nanorods with PbS QDs is used to make

ZnO/PbS solar cells. The solar cells manufactured had the highest open circuit voltage of 200 mV and the maximum short circuit density of 0.81 A/cm$^2$.

**Ismail *et al*. (2018) [45]** used deposition chemical bath deposition (CBD) was used to create lead sulfide thin films on both glass and Si (100) substrates. The produced films feature a polycrystalline structure with (200) preferred orientation, as per XRD analysis of the PbS films at 25°C. By increasing the deposition period, bigger grains might be obtained. X-ray electron impact spectrometry (XPS) was used to chemically analyze the produced films, indicated the existence of lead and sulfur as PbS. The stoichiometry of the produced film was confirmed using the energy dispersive X-ray fluorescence (EDX) technique. The change in the films' morphology with deposition time was studied using atomic force microscopy (AFM). The influence of deposition duration on optical transmittance in the UV-Vis-NIR band as well as the film architecture was studied. The simulation results indicated that as the thickness increased, the optical band gap decreased.

**Şahin *et al*. (2019) [46]** used the chemicals baths deposition (CBD) technique to produce pure PbS and PbS:Mo(3%) thin films on glass slides at room temp. The main objectives of this article is to see how the added metals Mo influences the crystallite size, optical energy band gap, and photovoltaic capabilities of PbS semiconductor thin films. Although the structure of the PbS:Mo(3% ) thin film is identical to that of pure PbS, the crystallite size of the PbS:Mo(3% ) thin film (24.12 nm) was found lower (25.97 nm). The band gaps of PbS and PbS:Mo(3% ) thin films were found to be 1.89 and 1.91 eV, correspondingly. The photovoltaic characteristics of PbS and PbS:Mo(3% ) thin films might be one reason for the increase in the bandgap of PbS:Mo(3%) thin film. The IPCE and J–V tests were used to investigate Mo(3%) thin films synthesized on Zn2SnO4 coated on FTO conductive glass using the CBD technique. At 400 nm, the IPCE ( percent ) ratios for pure PbS and PbS:Mo(3% ) thin films were 35 percent and 41 percent, correspondingly. The efficiency (µ) values for pure PbS absorption of Mo6+ ions into the PbS structure were 2.02 percent and 2.11 percent, correspondingly.

**Huo** ***et al.*** **(2019)[47]** used biochemical and deposition methods to produce Cr-doped lead sulfide (PbS) stores and supermarkets. All nanofilm samples had high crystallinity, with a preferred orientation of the (200) crystal plane, according to X-ray diffraction (XRD) analysis. The nanofilm grain size reduced from 71.5 to 18.9 nm as the Cr dopant rose. The SEM results demonstrated that variations in Cr content resulted in varied grain morphologies, and grain size shrank as doping concentrations increased. Optical research revealed that the band gap rose from 1.21 to 1.60 eV after Cr doping; the 2 percent Cr-doped PbS nanofilm, with an Eg of 1.49 eV, met the optimal band-gap value. The Hall mobility and volume carriers density of the nanofilm attained maximum values of 59.6 $cm^3$ and $20.7 \times 10^{16}$ $cm^3$ for a two percent Cr doped dosage, according to voltage measurement. The Cr-doped PbS nanofilms with a concentration of 2% exhibited the greatest electrical and optical properties, making them ideal for solar cell applications.

**Mitri** ***et al*****.(2020)[48]** investigated lead sulfide-based sensors CQDs for room temperature $NO_2$ detection. Sensor response was measured for various polluting gases including $NO_2$, $CH_4$, Carbon monoxide and carbon dioxide 2 for different concentrations in the range of 2.8-100 ppm. For the first time, the effect of film thickness QDs sensor response has been checked and improved. at 30 ppm $NO_2$ release the best The gas response at room temperature is about having a reaction time of 12 minutes and a recovery time of 12 seconds 26 minutes straight. The detection limit is estimated to be 0.15 ppb of the sensor slope response and its electrical noise. Gas sensors show high sensitivity to $NO_2$, remarkable selectivity, recurrence and complete recovery after exposure. **Mohammed *et al*.(2020)[49]** studied nano lead sulfide PbS thin films' structure properties. Pulsed laser deposition thin specimens were prepared and coated on glass substrates at wavelengths of 1064nm with varied laser energy (200,300,400,500)nm. The effect of adjusting the laser energy on physical properties has indeed been studied using a transmission electron microscope (TEM) and X-ray diffraction. The barrier formed is crystalline in nature, as per the findings. The planes (111) is the dominant phase (200). At a laser energy of about 200 mJ, the minimum yield strength obtained was 16.5 nm. Thin films of average granular sizes (75 nm) might be prepared, as per the results. The effect of adjusting the laser energy on optical properties was studied, and it was found that they have direct allowed transitions in the range of (1.55 to 2.45) eV.

## 1-7 The Aim of the Work

1- Preparation and manufacture of a gas sensor and studying of (PbS,PbS:Cd and PbS:Cr) physical properties.

2- Study of the effect of doping cadmium and chromium on the structural and optical properties of PbS thin films prepared on the glass and silicon substrates.

# Chapter Two

## Theoretical Part

## 2-1 Introduction

This chapter contains a general explanation of the theoretical part of the topic of work, including theoretical concepts, physical ideas, mathematical formulas, and special laws in theoretical results.

## 2-2 The Film Deposition Techniques

The wide and good application of thin films in modern technology is an important factor that has helped researchers improve various methods of manufacturing thin films. Later, scientific development techniques made great progress in preparing thin films with a high degree of accuracy in determining the uniformity and thickness of the films. The ability to determine and describe deposition procedures using key criteria such as the source, the nature of the paint particles, the nature of the interaction between the surface and the development medium, and the strategy for introducing different types of paint into the medium [50]. Thin films have a wide influence on the modern era of technology. Thin film technology is the basic base for advanced applications in various fields such as optical devices, environmental applications, communication devices, energy storage devices and the like. The use of thin films in different applications depends on their shape and stability. Thin membrane morphology relies heavily on sedimentation techniques [51].The formation of a film composition prepared using vacuum processes depends on three basic steps: (1) Creation of species suitable for atomic, molecular or ionic precipitation; (2) Transfer of species from source to substrate; And (3) condensation of species deposited on the substrate directly or by chemical reaction with reactive components, and the formation of solid precipitates [52].The method used for thin film deposition is based on several techniques that are regrouped in two classes

Physical vapor deposition (PVD): Spray, evaporation, ionic coating and laser ablation techniques fall into this category.

Chemical vapor deposition (CVD): spray pyrolysis, dipping technique, hydrogen reduction, electrophoresis and liquid solution gel are classified into this category[53]. Deposition methods can be classified into two main categories, physical techniques and chemical techniques, as shown in Figure (2-1) [54] .

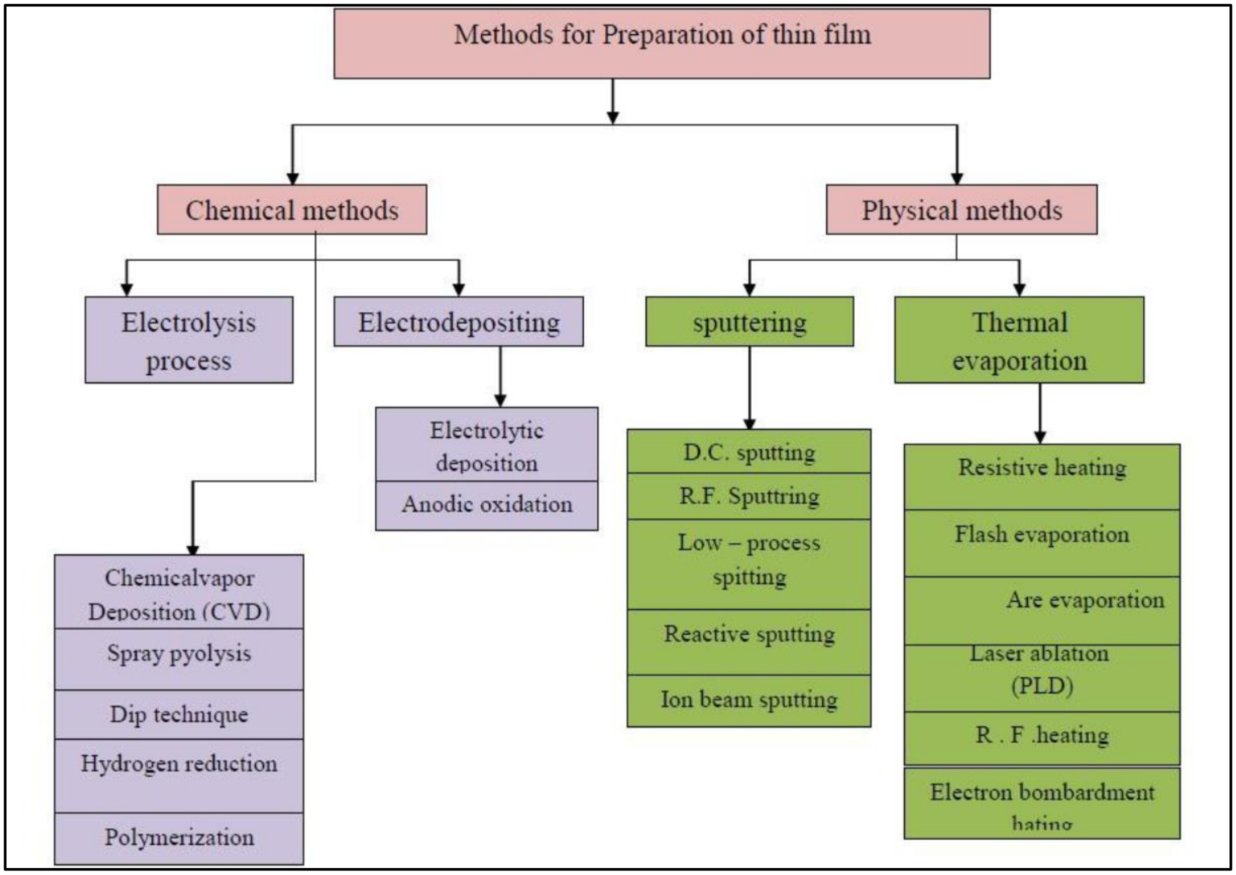

**Figure (2-1): show diagram of thin film preparation techniques [54].**

## 2-3 Pulsed Laser Deposition Techniques (PLD)

Pulsed laser deposition (PLD) is one of the most versatile techniques in solid state physics, which belongs to laser ablation in physical deposition technique. It is used in applied studies to prepare thin films of complex materials. The membrane preparation process with PLD technology adopts several stages, including the first stage, a high-energy pulsed laser beam is centered to hit a solid target inside a vacuum chamber, which leads to the evaporation of particles from the target surface forming a thick layer of vapor in front of the target called this plasma plume[55], which is formed as a result the energy absorption causes an increase in the pressure and temperature of this vapor. According to this increase, partial ionization of the atoms takes place, as just a wake wherein the world grows plasma a stratum of a top the target due to the high pressure and is formed in the second stage[56] .In the third stage, expansion takes place, the removed particles acquire several hundred eV as kinetic energy resulting from the conversion of the ionization energies and the internal heat. Due to the multiple collisions through expansion, attenuation of the kinetic energy occurs in the background gases of low pressure[57] .The pules laser deposition process can be categorized into three main physical categories.

- Particle extraction from the target surface with PLD.
- Transfer of excised from of the objective to a substrates, particulates.
- Particle deposition on the substrate

Figure (2-2) shows the PLD system.

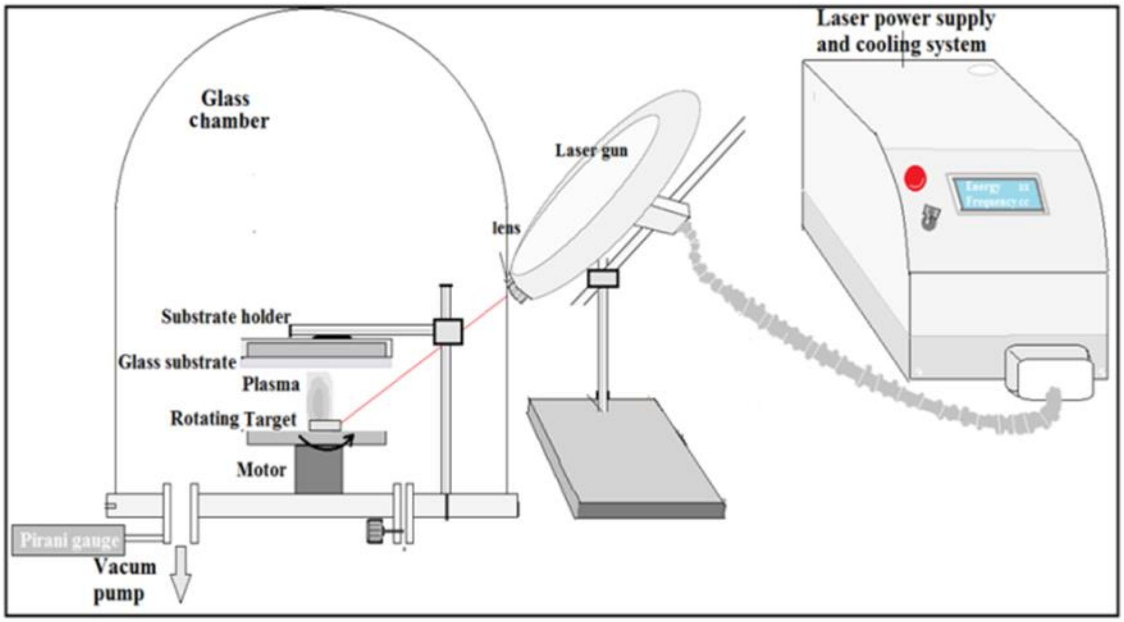

**Figure (2-2): Schematic diagram of PLD system** [58]

# 2-4 Solid Materials

Solids are classified in terms of their electrical conductivity into three sections as insulators, conductors, and semiconductors ln line with the theory of a band gap of it's material and the amount of the band gap that divides the valence band from the conduction band [59].

## 2-4-1 Insulator Materials

An insulator is a material that does not conduct an electric current. Because it has very few electrons that are free of motion or without a free electron. The energy gap separating the valence band from the conduction band is very large, which lies in the range (4-5.5) eV, such as wood, plastic, glass and others. Figure (2-3.a) shows the dielectric energy gap [60].

### 2-4-2 Conductor Materials

An electrical conductor, which is the material that allows electrons to pass through it easily, means that there is no resistance against this electron movement. Like metals they are very good conductors due to the fact that the energy level between conduction bar and equilibrium is very close and in most cases the conduction and valence band are covered. The conductor band gap is shown in Figure (2-3.b) [61], while the electrical conductivity of a metal such as aluminum is very high in the range $(10^{3}-10^{8})$ $(\Omega\ .cm)^{-1}$

### 2-4-3 Semiconductors Materials

A semiconductor is a core material with electrical materials in the middle of the insulator and the conductor. In semiconductors, electrons can be energized effortlessly from the valence band to the conduction band because there are few band gap energies of less than (3 eV) between the valence band and conduction band. The band gap structure of a semiconductor is shown in Figure (2-3.c) [62], while the electrical conductivity of semiconductors is shown in the range between $(10^{-8}-10^{3})$ $(\Omega\ .cm)^{-1}$ [63]. Semiconductors are affected by heat, magnetic field and light, and this has led to their adoption as a very basic material in electronic applications, at temperature coming to(0 K) behaves as an insulating materials while, its electrical conductivity increases by increasing the temperature above (0 K). In general, there are several opinions about semiconductors .

1- Conductivity is affected by magnetic fields.

2 - Has a negative thermal resistance coefficient.

3- Sensitive to light by PV phenomenon.

4- It has two types of charge carriers: electrons and holes. These make them the opposite of what appears in minerals.

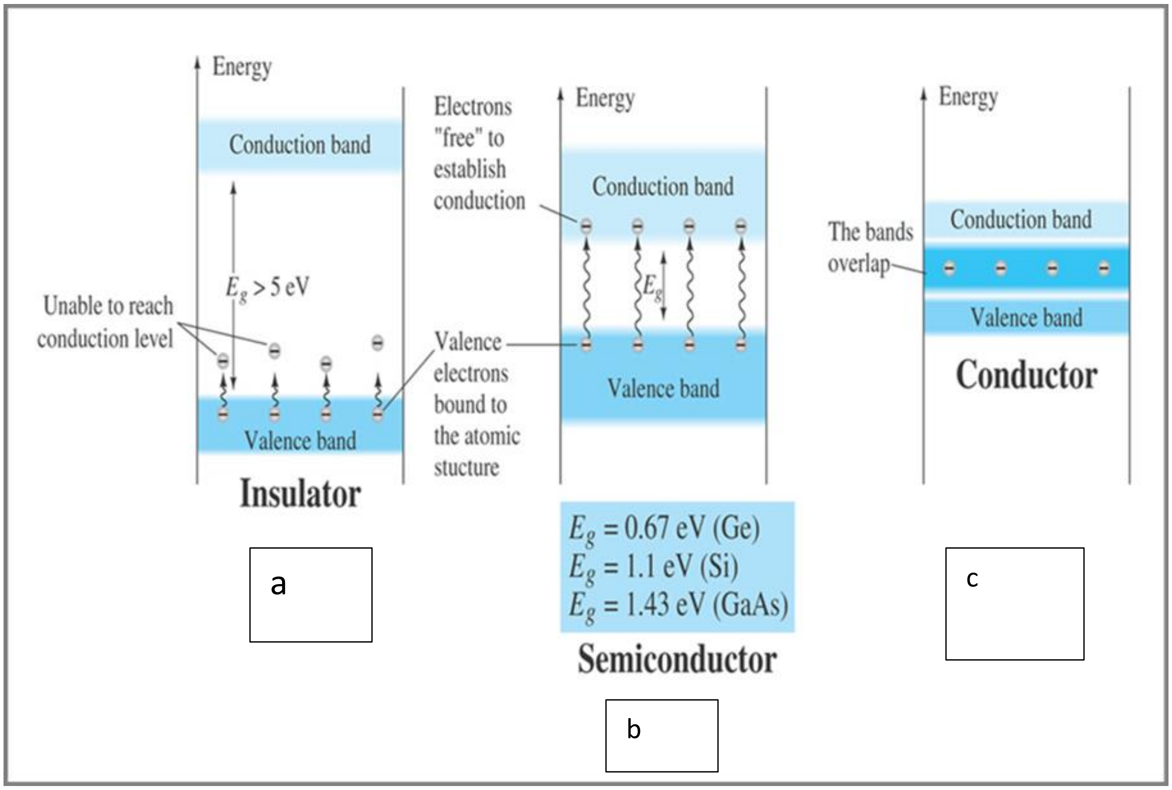

**Figure (2-3): the band gaps energy in solid materials[64]**

# 2-5 Types of Semiconductors

## 2-5-1 Intrinsic Semiconductors

It is a type of semiconductor and is known as uncovered or pure semiconductor as well, meaning it is free from any impurities. In this type of pure semiconductor at a temperature (0K). The conduction band ($E_c$) is nearly free of electrons while the valence band ($E_v$) is completely energyed by electrons [65] . Figure (2-4) shows the crystal structure of silicon and an energy gap ($E_g$) diagram at (0K). , and when the temperature of a pure semiconductor is raised to a certain high temperature, a certain number of valence electrons will be thermally affected and move directly into the conduction band. Each electron moving out of the valence band leaves something very important called holes which will be the positive charge carrier in the valence band while electrons carry the negative charge in the conduction band and are amenable to electric conduction once the field is applied.

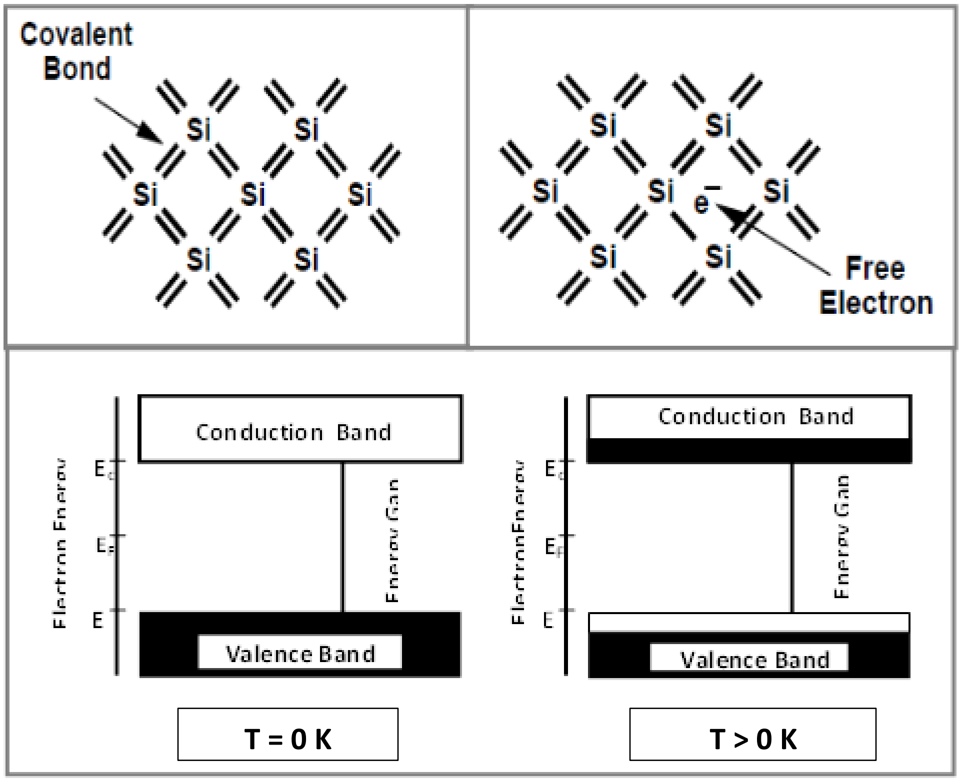

**Figure (2-4): crystalline structure of silicon and energy bands for intrinsic semiconductors[66].**

The process of producing an electron-hole pair continues as long as the effect of the heat continues, and the direction of movement of the holes is towards the applied electric field, which appears in the opposite direction to the free movement of electrons [67], as shown in the Figure (2-5)

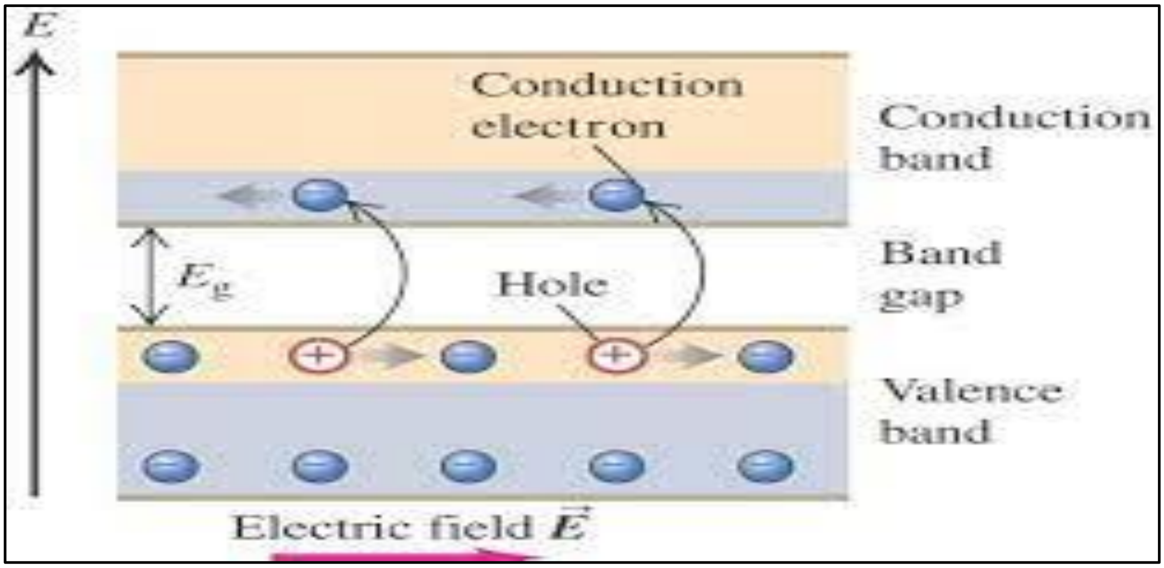

**Figure (2-5): Charge carriers movement direction in pure semiconductors (crystal of silicon) affected by applied electric field [68].**

### 2-5-2 Extrinsic Semiconductors

The heat treatment process is known to increase the electrical conductivity of pure semiconductors, but it is not desirable in practical application, particularly in the manufacture of devices. This is due to the difficulty in controlling the resulting electricity. Therefore, we use another method, which is grafting to change the pure semiconductor to an external semiconductor, by adding a limited number of impurity atoms to the pure semiconductor crystal. During the damping process, the impurity atoms will add new energy levels, generally the location of these levels, in the region between the conduction beam and the valence beam which is known as the blocked energy gap [69].

## 2-6 Crystal Structure for Semiconductors

Crystal structure in semiconductor materials can be classified into two types

### 2-6-1 Crystalline Semiconductors

The arrangement of atoms and molecules in this type of crystalline semiconductor is geometric and organized in a lattice of this means that there are atoms that function periodically in a three-dimensional form known as (far-reaching arrangement). Thus, It has kind of crystal symmetry. In this arrangement it can be considered a specific geometric model called unit cell. Crystalline semiconductors are divided into two parts:

1- Monocrystalline semiconductor

The periodic crystal model of its atoms extends across the entire 3D crystal, as shown in Figure (2-6.a).

2- Polycrystalline semiconductors

The cyclic shape of its atoms does not extend across the crystal, but rather stops at the boundary within the crystal known as the grain boundary, as shown in Figure (2-6.b).

### 2-6-2 Amorphous Semiconductors

The arrangement of atoms in this type of amorphous semiconductor is in randomly irregular shapes, so the periodic crystal form is not present in three dimensions. It has a short-term arrangement consisting of a complex formation that does not consist of any unit cell. Likewise, the arrangement of atoms is not repeated periodically, as in crystalline materials. It is possible to have uniformity in a very short range, but quickly lose it at a distance greater than one or three atomic radii as proven by Figure ( 2-6.c.)

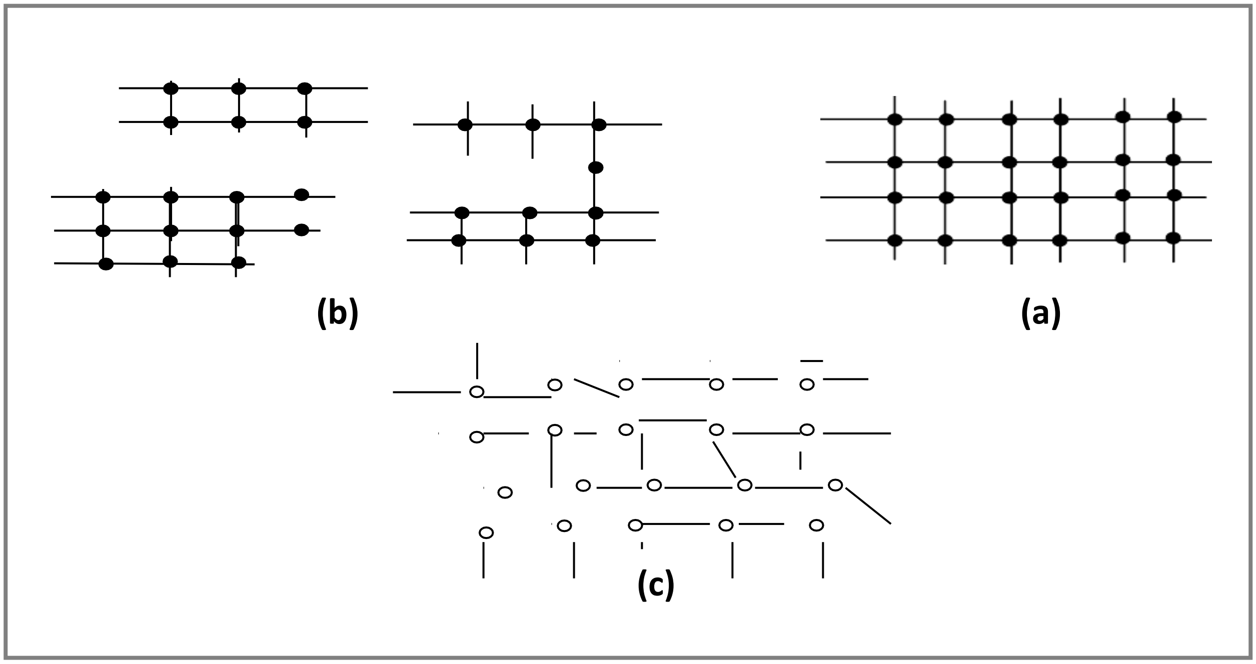

**Figure (2-6): Classification Solids are categorized according the order of its atoms. [70].**

**(a) A single incidence in crystallization**
**(b) Polycrystalline**
**(c) Amorphous**

The method of preparing and manufacturing materials is the reason for the existence of two types of solids (crystalline and amorphous). In the event that the atoms manage to arrange themselves within matter into a specific shape and are less heavy they can produce crystalline materials. Whereas, when the atoms are not able to arrange themselves, they will have a random distribution such that the overload is greater than the atoms in the crystalline state and produces amorphous solid materials [71].

# 2-7 Structural Characteristic

## 2-7-1 X-ray Diffraction

X-rays are electromagnetic waves located in a limited spectrum region between the UV region spectrum and the gamma ray spectrum. It has wavelengths ranging from (0.1 - 100) A°. X-rays are used in the diffraction crystal experiment becouse their wavelength is proportional to the intermediate distance of the atoms, so they are used to study the crystal structure of the material. As well as knowing the atomic structure of the lattice. Or even imaging the distribution of atoms by projecting a beam of X-rays at a certain angle (θ) on crystalline planes. X-rays interact primarily with electrons in the atom. When photons in the X-ray collide with electrons, some of the incident beam photons deviate from their original direction. If the incident X-ray wavelength does not change (that is, the X-ray photons have not lost any energy) the process is called an elastic collision, whereby the momentum of motion is only transformed in the collision process [72]. These are the x-rays that we measure in diffraction experiments that give us information about the distribution of electrons in materials. On the other hand, in the process of inelastic collision or Compton collision, X-rays transfer some of their energy to the electrons, so the neutral X-rays have a wavelength different from that of the X-rays [73], as shown in Figure (2-7).

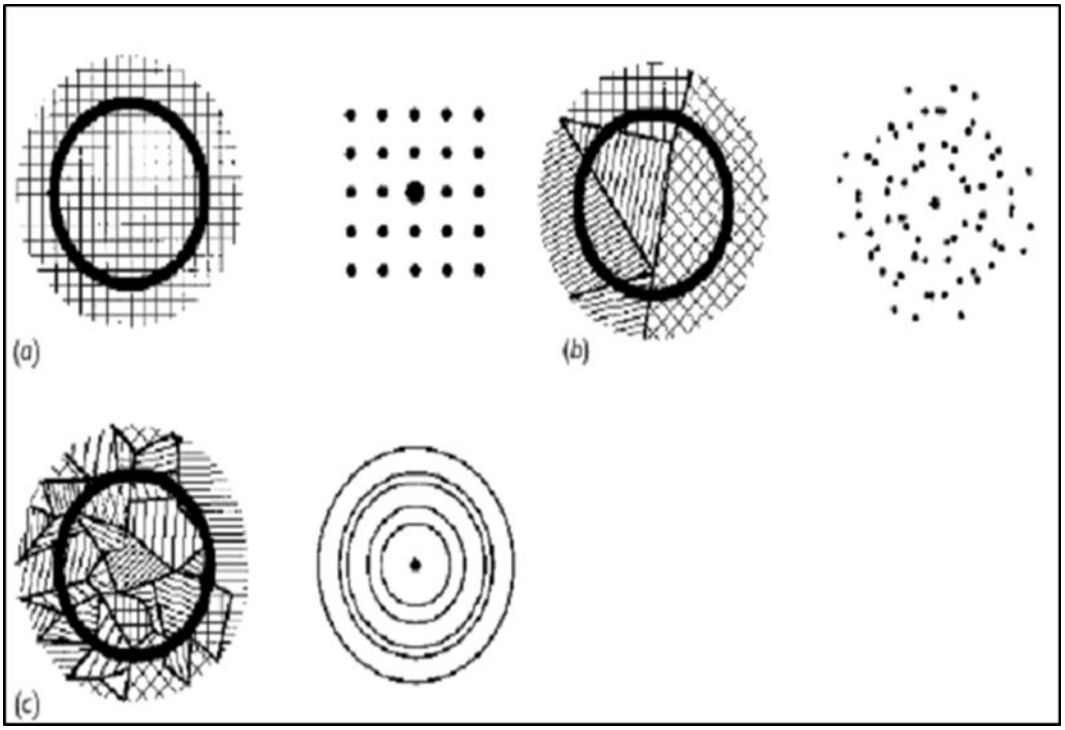

**Figure (2-7) :The X-ray diffraction of materials**
**(a)A single crystal. (b) Polycrystalline. (c) Amorphous[66].**

## 2-7.2 Bragg's Law

The physicist Bragg has proposed a very important supposition to study the crystal structure by using X- ray diffraction through knowing the direction of the X-ray diffraction of crystal after incident on it, as shown in figure (2-8). Also the Bragg's law, which would be represented inside the equation given, could be used to calculate inter - planar distances (d). [74].

$$n\lambda = 2d_{hkl} \sin\theta \quad \ldots\ldots\ldots\ldots\ldots\ldots\ldots\ldots (2\text{-}1)$$

Where $\theta$ : is the diffraction angle or Braggs angle, n: is the reflection ordering, $d_{hkl}$: is the spacing between both the atomic scale in a crystalline, as well as $\lambda$: is the wavelength of the falling X-ray.

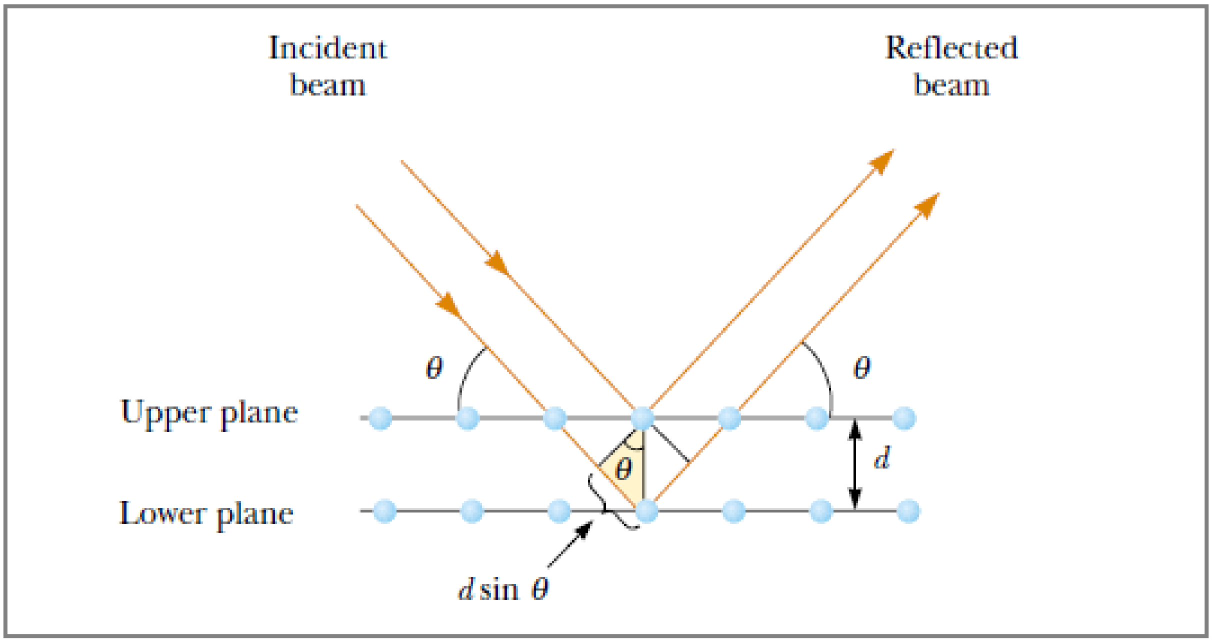

**Figure (2-8): Bragg′s law and Crystalline layers [75]**

There is a necessary condition for the occurrence of a Bragg′s reflection of the crystalline levels its Millier′s coordinate (hkl), known as Bragg′s condition. Which indicates that the wavelength of X-ray applied in equation (2-1) should be smaller or equal to double the atomic interface distance between two successive levels of crystals. Bragg′s condition can be represented in the following equation [67].

$$\lambda \leq 2d_{hkl} \quad \text{………………………….(2-2)}$$

Some empirical methods were designed for the purpose of applying this law from obtaining a pattern of X-ray diffraction [76].

1-Laue method.

2-Oscillating – Crystal method.

3-Powder method.

4-Rotating – Crystal method.

Analyzing procedure using any of these methods depends on the change angles value (θ) continuously or alteration the value of wavelength (λ) of the X-ray during the examination process. When the target is rotated at a certain angle (θ), the detector will be rotated at an angle of (2θ) so that, the angles which have recorded are double value of the angle has used in Bragg′s law. Therefor the value of ($d_{hkl}$) can be calculated from equation (2-1) if the value of λ and θ is known, provided that the rays are used a single wavelength.

# 2-8 Structure Parameters

## 2-8-1 Interpleader Distance

Found the Interpleader distance using Bragg's law and according to the relationship (2-1)

## 2-8-2 Crystal Size (C.S)

The Sherrer relationship could be used to calculate the expected crystallite size. [77].

$$C.S = \frac{0.9\,\lambda}{B\,\cos\theta} \quad \text{……………………….(2-3)}$$

Where B:  is full width at half maximum of peak (FWHM), θ: Bragg's angle.

## 2-9 Optical Properties for Polycrystalline Semiconductors

### 2-9-1 Absorption Coefficient (α)

The absorption coefficient is the rate of decrease in the flux of radiation energy into a unit distance in the direction of propagation of the wave within the medium. It is based on the properties of semiconductors and the energy of the incident photon [78]. When a beam of radiation falls on the surface of the thin film, a set of processes occur for this beam, as shown in Figure 2-9. Some of it is transmitted, some of it is reflected, and some of it is absorbed by the material of the film. It was noted that the amount of all transmitted, reflected and absorbed rays depend on the wavelength of the incident radiation and the nature of the thin films and their surface. The largest part of the absorption (63%) occurred at a distance (1 / α), which is known as the penetration depth [79]. The amount of absorption coefficient is binary important because it indicates the ability of the film to absorb the energy of the incident radiation. on him. However, the type of electron transmission can be determined in terms of the value of α where, at a high value of α which is ($\alpha > 10^4$ $cm^{-1}$), this means that the probability of direct electron transmission. While a low value of α ($\alpha < 10^4$ $cm^{-1}$) indicates the potential for indirect transmission [80]. The following formula could be used to determine the absorption coefficient:

$$\alpha t = 2.303 \log (I / It) \text{ .......................... } (2\text{-}4)$$

Where t is the film thickness, It is the incident radiation intensity and It is the transmitted radiation intensity.

Figure (2-9) shows the fall of radiation on a thin film [81].

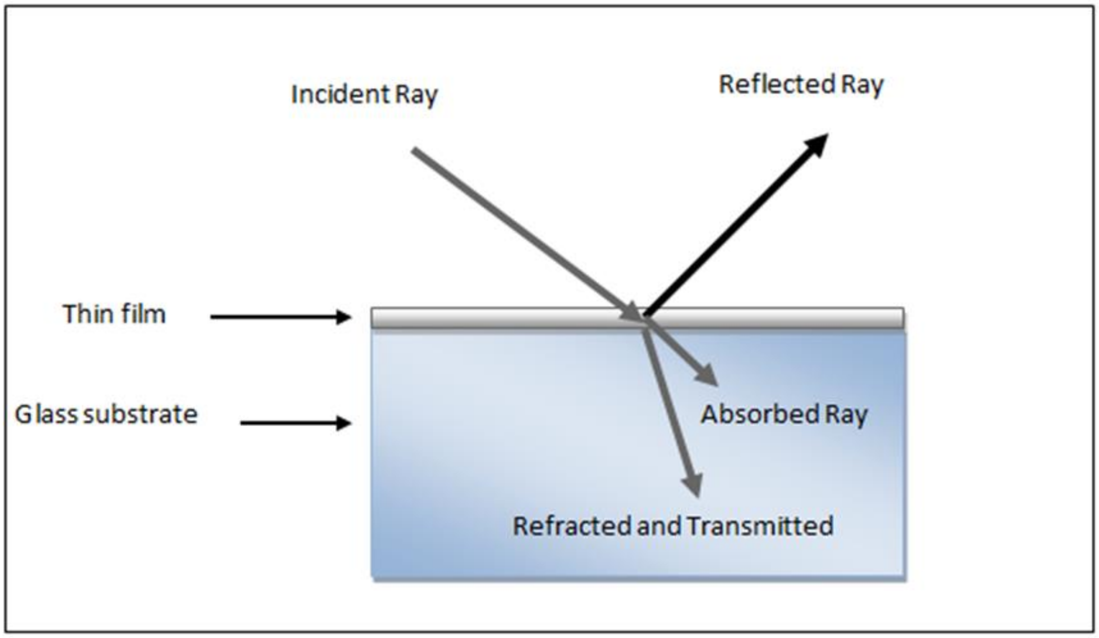

**Figure (2-9): falling of radiation on thin film[81].**

## 2-9-2 Regions of Absorption

The absorption process is one of the most important processes that occur inside the material, where an electron is transferred from collecting photon energy from radiation mostly on substance, the fermi level is transformed to the band gap [82]. The energy of the incident photon must be greater or equal to the optical energy gap between the valence band and the conduction band .The main absorption regions in semiconductors are divided into three separate regions, as shown in Figure (2-10).

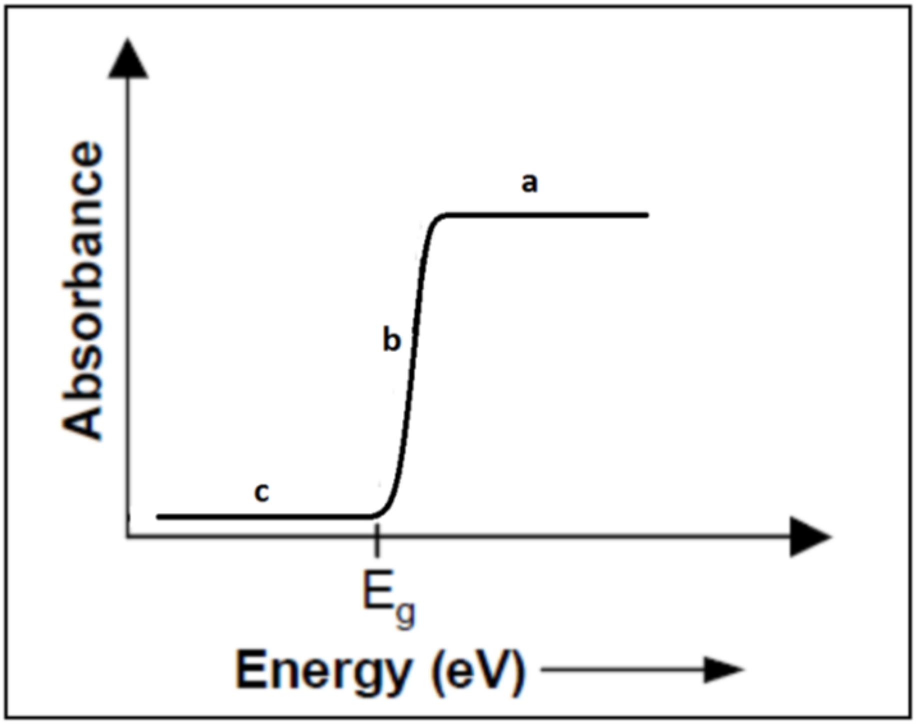

**Figure (2-10): Edge of Semiconductors' fundamental absorbing (a) area of higher absorption. (b) the area of exponential absorption. (c) Area having weak absorption [83].**

## 2-9-2-1 High Absorption Region (a)

In this region, transitions occur between levels extended in the valence band to levels extended in the conduction band. The value of the absorption coefficient for this area is ($\alpha \geq 10^4$ cm$^{-1}$) [84].

## 2-9-2-2 Exponential Absorption Region (b)

Two types of transfers occur in this region, in the first type a transfer occurs between levels extending in the parity band to bound levels in the conduction band. The second type occurs between levels confined at the highest point in the parity band to levels extending at the lowest band in the conduction band. The absorption coefficient value for this region is between ($1 < \alpha < 10^4$ cm$^{-1}$) [85].

### 2-9-2-3 Low Absorption Region (c)

In this area, $\alpha$ is very small. It lies at about ($\alpha < 1\ cm^{-1}$) It is explained by the transitions between levels in the range's tails. It should be pointed out that due to the low level of absorption in this part of the absorbance tails, verifying this is difficult [86].

## 2-9-3 Absorbance (A)

The amount ($\log I_i / I_t$) represents the absorption of the thin film, denoted by (A). The intensity of the incident radiation decreases greatly ($e^{-\alpha t}$) inside the material, where the absorption coefficient ($\alpha$) is an example of the rate of decay of the radiation energy inside the material [87]. Therefore, equation (2-4) can be written as follows:

$$\boldsymbol{\alpha = 2.303\ A / t} \quad \textbf{……………………… .. (2-5)}$$

# 2-10 Transitions in Thin Film

Semiconductor electronic transformation can be mainly divided into two types:

## 2-10-1 Direct Transitions

Electronic transformations occur in semiconductors possessing direct bandgap energy of two types. The first transition is known as the permissible direct transition which occurs when electrons move from the same wave vector from the valence band to the empty conduction band void point (k - space) provided that ($\Delta K = 0$) and $K = 0$ [88]. The second transition called the direct blocking transition that occurs when electrons move from regions of proximity to the region of direct transition while maintaining the state continuity that does not change the value of the wave vector (i.e.: $K1 = K2 \neq 0$ but $K = 0$). Figure (2-12) shows the direct transmission and the absorption equation for these types of semiconductors can be given as follows [89].

$$\alpha h\upsilon = P\ (h\upsilon - E_g)^r \ \ldots\ldots\ldots\ldots\ldots\ldots\ldots (2\text{-}6)$$

Where E is the energy of the incident photon and P is constant. The nature of the transition occurring in a semiconductor having a direct energy gap is determined using Equation (2-6). Where the permissible direct transmission occurs with a value of (r) equal to (1/2), and the prohibited direct transmission occurs with a value of (r) equal to (3/2) [90].

## 2-10-2 Indirect transition

The indirect transfer of electrons occurs when the energy of the upper part of the valence band and below the conduction band is inconsistent in the wave vector vacuum (space K). Since in this case the electron transition occurs between location and in valence band as well as any non-perpendicular location in the conduction band direction accordingly, the wave vector value ($\Delta K \neq 0$) [80]. The relationship between the absorption coefficient and the optical energy gap is given in the following equation [91].

$$\alpha h\upsilon = P^{\backslash}\ (h\upsilon - E^{\backslash}_g \pm E_P)^r \ \ldots\ldots\ldots\ldots\ldots\ldots\ldots..(2\text{-}7)$$

Where: $E^{\backslash}_g$ is the energy band gap of the indirect transmission, + $E_P$ is the phonon absorption process, - $E_P$ is the phonon emission process and $P^{\backslash}$ is constant. There are two types of indirect transmission, the first type is known as the permissible indirect transfer which occurs when an in a non-straight path, an electrons passes from the maximum height inside the valence band to the lowest level in the conduction band. direction as shown in Figure (2-11). The value of (r) will be in equation (2-7) for this transition (2). The second type is called the indirect blocking transition which occurs when an electron moves from regions of proximity to that extreme in a non-straight path from of the highest point throughout the valence band to the lowest level throughout the conduction band direction and the value of (r) in equation (2-7) will be (3). In contrast to direct transmission, in this type of transmission, the absorption and emission action is temperature dependent [69].

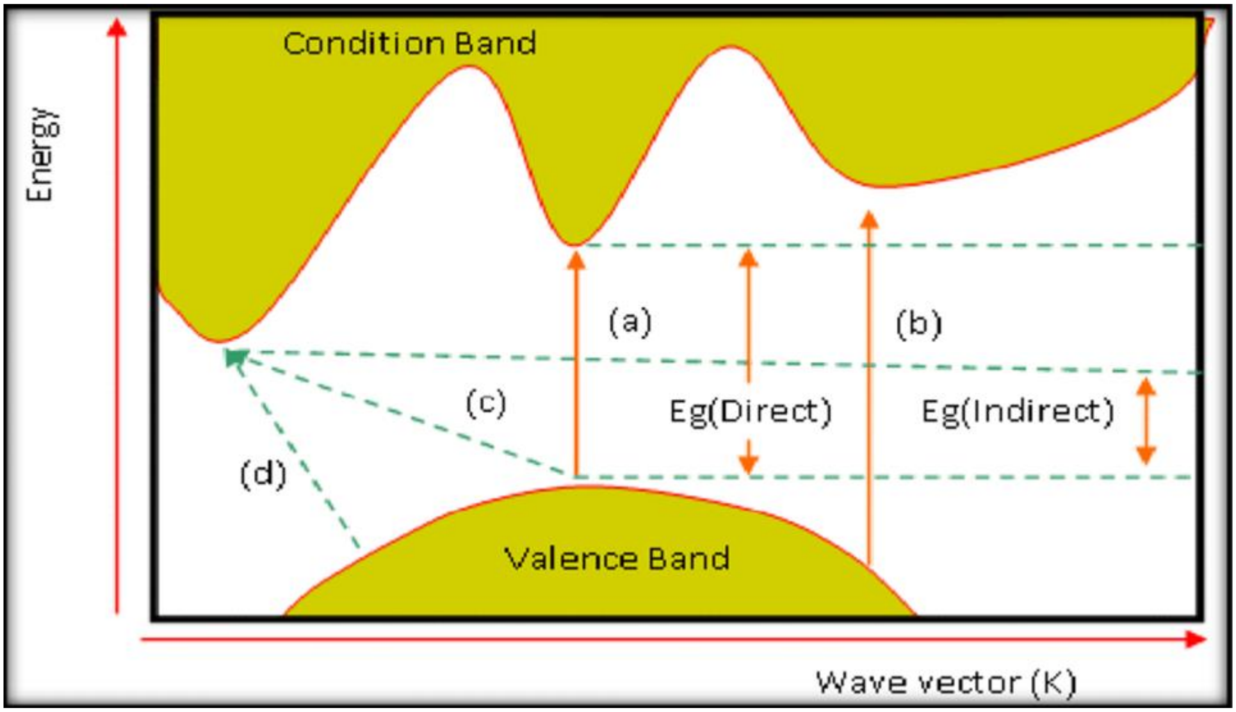

**Figure (2-11): Electronic transition kinds [92].**

(a) Direct allowed. (b) Direct forbidden. (c) Indirect allowed. (d) Indirect forbidden.

## 2-11 Optical constant

### 2-11-1 Transmittance (T)

It is the ratio between the intensity of the transmitted rays to the intensity of falling rays on the surface of the material. It is related to reflectivity and absorptance as shown in the following equation, according the law of energy conservation [93].

**R + T + A= 1 …………………… ..… (2-8)**

## 2-11-2 Reflectance (R)

It is the ratio between the intensity of the rays reflected during the fall of a radiation beam of a certain wavelength on the surface of the material to the intensity of the incident rays [85]. The reflectivity is the accompanying connection exists between both the refractive index and the extinction coefficient [82].

$$R = \frac{(n_\circ - 1)^2 + K_\circ^2}{(n_\circ + 1)^2 + K_\circ^2} \quad \ldots\ldots\ldots\ldots\ldots\ldots\ldots\ldots (2\text{-}9)$$

Whereas $K_\circ$ is the extinction coefficient and $n_\circ$ is the real refractive index.

When $K_\circ = 0$ the above equation becomes:

$$R = \frac{(n_\circ - 1)^2}{(n_\circ + 1)^2} \quad \ldots\ldots\ldots\ldots\ldots\ldots\ldots\ldots (2\text{-}10)$$

## 2-11-3 Refractive Index ($n_\circ$)

It is the ratio of a light speed in a vacuum (c) to the light speed in a certain medium. (υ). The real portion of the refractive index complicated is $n_c$ .It can be calculated by following equation [85].

$$n_o = \left[\left(\frac{1+R}{1-R}\right)^2 - \left(k_o^2 + 1\right)\right]^{1/2} + \frac{1+R}{1-R} \quad \ldots \ldots (2\text{-}11)$$

The complex refractive index is given by the following equation.

$$n_c = \sqrt{\varepsilon} \quad \ldots\ldots\ldots\ldots\ldots\ldots\ldots\ldots (2\text{-}12)$$

Where $\varepsilon$ is the complex dielectric constant.

## 2-11-4 Extinction Coefficient ($K_\circ$)

It is the amount of energy absorbed by the electrons of the material, which causes the decrease of the radiant energy falling to the material. Also, it represents the imaginary part of the complex refractive index $n_c$ and the following equation shows the relationship between $K_\circ$ and $n_c$ [94].

$$n_c = n_\circ + iK_\circ \quad \dots\dots\dots\dots\dots\dots\dots\dots\dots (2\text{-}13)$$

The extinction coefficient is related to the absorption coefficient with the following equation that was used to calculate $K_\circ$ for all the thin films prepared [95].

$$K_\circ = \alpha\lambda / 4\pi \quad \dots\dots\dots\dots\dots\dots\dots\dots\dots (2\text{-}14)$$

## 2-11-5 Dielectric Constant ($\varepsilon$)

It represents the material's compliance with various frequencies and complex behavior, and the material's ability to polarize by means of the dielectric constant. The level of polarization of a surface is measured by its physicochemical structures of material which depends on the electric field. The polarization of the medium charge due to the interaction of light with the charges of this medium is determined by the complex dielectric constant ($\varepsilon$) which is given mathematically as follows [85, 96].

$$\varepsilon = \varepsilon_r + i\varepsilon_i \quad \dots\dots\dots\dots\dots (2\text{-}15)$$

Where $\varepsilon_r$ and $\varepsilon_i$ are the real and imaginary parts of the dielectric constant, respectively. The complex dielectric constant is related to the complex refractive index by the following equation:

$$\varepsilon = n_c^2 \quad \text{……………………} \textbf{(2-16)}$$

Substituting in the value of the equation ($\varepsilon$, $n_c^2$) (2-16) becomes:

$$\varepsilon_r + i\varepsilon_i = (n_\circ + iK_\circ)^2 \quad \text{……………} \textbf{(2-17)}$$

Two separate equations can be obtained from equation (2-17) representing the real and imaginary part of the dielectric constant as in the following equations:

$$\varepsilon_r = n_o^2 - k_o^2 \quad \text{………………} \textbf{(2-18)}$$

$$\varepsilon_i = 2 n_o k_o \quad \text{………………} \textbf{(2-19)}$$

The last two equations were used to compute the real and imaginary part of the dielectric constant for all prepared thin films.

## 2-12 Hall Effect

This phenomenon was discovered by the American scientist Edwin Hall in 1879 and is called the Hall Effect. It is defined as the different distribution of current in a metal strip under the influence of a magnetic field. Through it, the type and density of the charge carriers and the movement of these charges are determined. We notice that when there is a magnetic field present to a semiconductor on the vertical direction for a current that passes through it as a result, an electric field is created in a vertical direction on both the magnetic field and the current as shown in Figure (2-12) [97]. The hall coefficient ($R_H$) represents the ratio of the output voltage to the current product and magnetic field ($\vec{i} \times \vec{B}$) taking into account the thickness of the films. The Hall parameter is given mathematically by the following formula [98].

$$R_H = \frac{V_H}{i_x} \cdot \frac{t}{B_Z} \text{..............................} (2-20)$$

Where $V_H$ is the hall voltage, t is the films thickness, $i_x$ is the external current and $B_z$ is the magnetic field strength. The value of the Hall coefficient depends on the number, type and properties of charge carriers, and the type of semiconductor can be determined by the sign of the $R_H$ value. When its sign is negative it is a semiconductor (n type), and when it is positive it is a semiconductor (p type) and may determine the concentration of the carrier of semiconductor type and carrier type using the Hall coefficient equation, $R_H$ is negative for n-type and positive for p-type, correspondingly. [90].

$R_H = \frac{-1}{ne}$ in the n-type …………(2-21)

$R_H = \frac{1}{n\mathrm{p}}$ in the p-type…………(2-22)

The electron charge is denoted by the letter e. If the conduction is owing to a single type of carrier, such as electrons

$\sigma_n = qn\mu_n$ for n-type………………..(2-23)

And

$\sigma_p = qn\mu_p$ for p-type………………..(2-24)

We can measure the Hall mobility as :

$\mu_H = \frac{\sigma}{n.e}$ ………………………………..(2-25)

$$\mu_H = \sigma . |R_H| \quad \ldots\ldots\ldots\ldots\ldots\ldots\ldots\ldots\text{(2-26)}$$

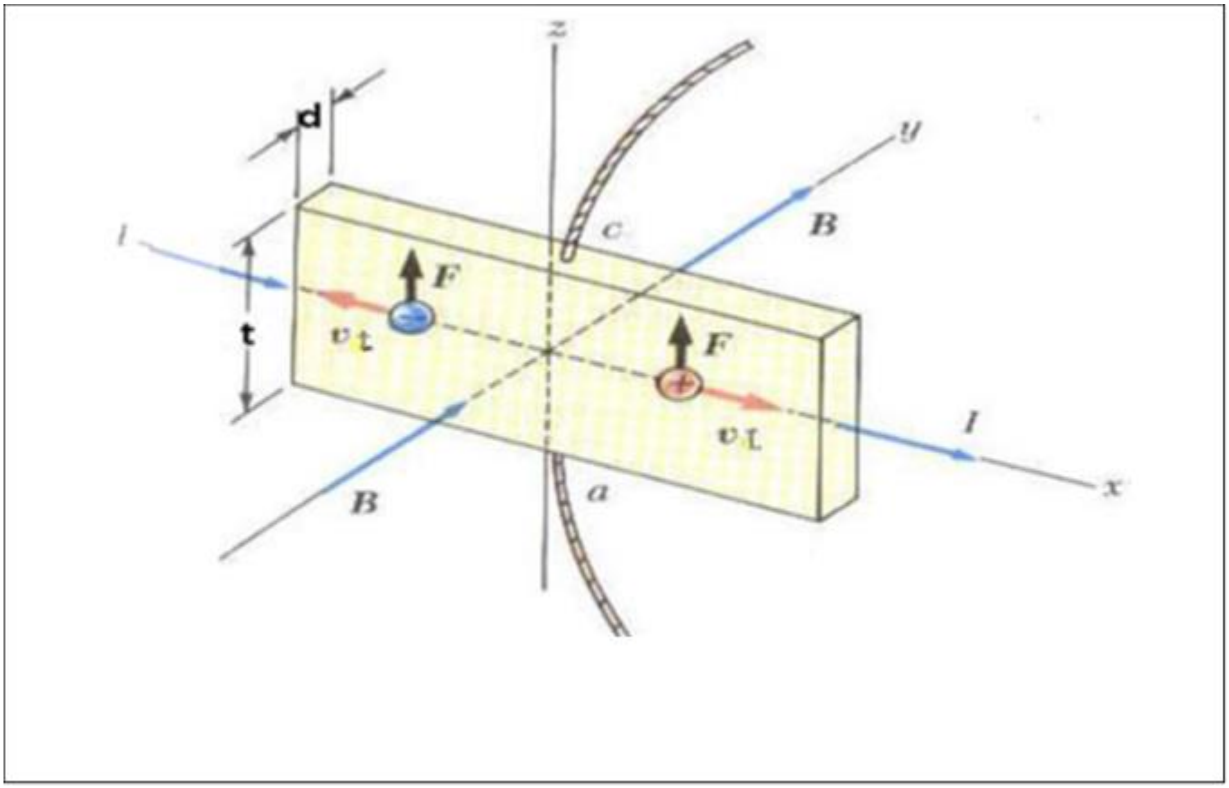

Figure (2-12): Hall Effect diagram [91].

## 2-13 Gas Sensor

Semiconductors are one of the basic materials used in the manufacture of gas sensors and to date they are manufactured and increase their efficiency .The purpose of this use is to reduce manufacturing cost, high energy and temperature rise. In order to improve their sensitivity and increase their effectiveness in gas sensitivity, impurities are added in specific proportions [99].

Gas sensors have such a variety of applications, a most significant of these is the identification of catastrophes including such toxic gases or reactivity inside the environment, and the detection of pollution in the environment [100].

### 2-13-1 Sensitivity (S)

It is the rate of change in the resistance of the thin film to the presence and absence of gas. Among the most important factors affecting it are: relative humidity, temperature of sensors, response time to sensitization, time of exposure of gas films, background of gas composition, and thickness of the membrane. It is calculated from the following relationship [99].

1- In case of reduction

$$S = \left| R_g - R_a \right| / R_a \times 100\ \% \ldots\ldots\ldots\ldots\ldots\ldots\ldots (2\text{-}27)$$

2- In case of oxidation

$$S = \left| R_a - R_g \right| / R_g \times 100\ \% \ldots\ldots\ldots\ldots\ldots\ldots\ldots (2\text{-}28)$$

Where: $R_g$ and $R_a$ are film resistances measured in the existence of a gas and an atmosphere environment, accordingly.

### 2-13-2 Response and recovery times

When the sensor is exposed to the target gas, the response time is defined as the time it takes for conductance to achieve 90% of the payback period. Whenever a sensor is in the out-gas state and then placed in clean air, the recovery time is defined as the time it takes for the sensing output to fall to 10% of the maximum rate as shown in Figure (2.13). An excellent sensor is described as having a brief response and recovery time, enabling it to be used frequently [101].

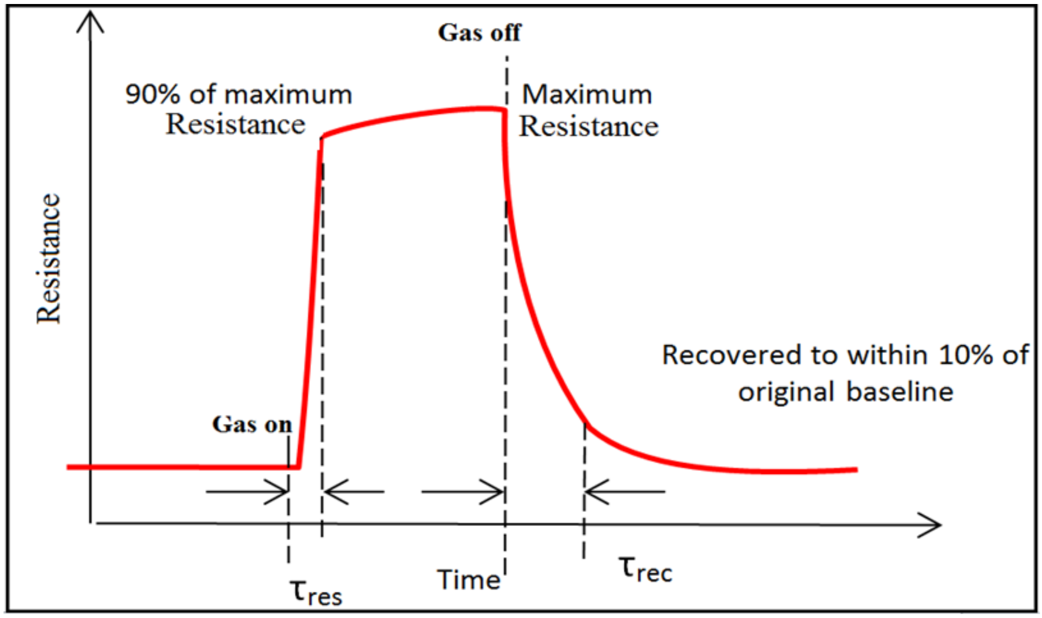

**Figure (2-13): Typical structure of a conductivity sensor [102].**

### 2-13-3 Applications of Gas Sensors

Sensors detecting gas are employed in a variety of purposes, as the [103]:

1-Use in industries to monitor the concentration of the toxic gases.

2-Use  in households to detect an emergency incidents.

3-Use at oil rig locations to monitor the concentration of the gases those are released.

4-Use  at hotels to avoid customers from smoking.

5-Use  in air quality check at offices.

6-Use  in air conditioners to monitor the $CO_2$ levels.

7-Use  in detecting fire.

8-Use  to check concentration of gases in mines.

# Chapter Three

## Experimental Work

## 3-1 Introduction

This chapter includes a brief description of the pulsed laser deposition technique used in the preparation of the thin films and the thin film deposition stages. As well as explaining the techniques and devices used in the process of examining and diagnosing the prepared films and the gas sensor.

## 3-2 Equipment of Deposition

Figure (3-1) shows the basic components of the PLD system as shown by the arrangement of the target placed on the substrate holder inside the room in proportion to the laser beams.

**Figure (3-1): Pulse laser deposition system in plasma lab- University of Baghdad.**

### 3-2-1 Nd:YAG Laser Source

Use of Nd:YAG laser (Huafei Tongda Technology - DIAMOND- 288pattern EPLS) to precipitate pbs films. This part of the system consists of computer control system, cooling system, light path system, and energy supply system. The light path system is installed in the hand piece, while the control of the cooling system and the energy supply are installed in the machine box of the energy supply.

**Basic technical parameters:**

- Laser model: Q-switch Nd: YAG second harmonic generation (SHG) laser.
- Energy supply (220V).
- Laser wavelength (1064nm).
- Repetition frequency (6 Hz).
- Pulse count (100).
- Pulse duration (10 ns).
- Cooling method (internal circulation of water for cooling).

### 3-2-2 Vacuum System

The sedimentation chamber was installed on a steel flange comprising an O-ring groove to seal the vacuum and charge - through the foundation for the electrical connection (stepper motor control and the substrate heater). The chamber is evacuated using a circulating pump directly connected to the chamber by stretchable tubes to obtain a vacuum less than $10^{-2}$ mbar and monitor the pressure inside the chamber using a pyraniometry.

## 3-3 Target Preparation

The target used in the precipitation was prepared from pure nanoparticle lead sulfide (PbS). The target is in the form of a circular disc under a pressure of 10 tons, the dimensions of the resulting target are 2.5 cm diameter and 0.4 cm thick. The compression process produced a thick, homogeneous target in order to ensure the high quality of the film deposition. Figure (3-2) shows the sample before and after the compression.

**Before** **After**

**Figure (3-2): Target before and after pressing.**

## 3-4 Substrate Preparation

### 3-4-1 Glass substrates

The substrates of glass (7.5 x 2.5) $cm^2$ have been utilized to deposit the thin films for the purpose of execution the necessary tests. Several steps have been taken to clean the glass substrates, the first step is to remove dust particles and any impurities suspended on the substrate surface using distilled water. The second step is using the ultrasonically device .It is cleaned in alcohol for 15 minutes before use.The last step is drying the cleaned substrates by a dryer.

### 3-4-2 Si substrates

The substrates of Si two types are (n-type and p-type) for the purpose of manufacturing a gaseous sensor from thin films are (PbS,PbS:Cd and PbS:Cr) and in specifications diameter 100 mm and orientation(100) thickness (500-525) µm the first step is to remove dust particles and any impurities suspended on the substrate surface using distilled water. The second step is using the ultrasonically device .It is cleaned in alcohol for 20 minutes before use. The last step is drying the cleaned substrates by a dryer.

## 3-5 Thin Films Deposition Procedure by PLD

Pulsed laser deposition technique was used to prepare single-step thin PbS films directly onto glass substrates placed above the target within the vacuum chamber of the PLD system. Sedimentation was completed at room temperature with a back pressure ($2x10^{-3}$ mbar). The target of PbS,PbS:Cd and PbS:Cr it was also doped with cadmium and chromium in doping rates(X= 2,4,6) wt%. Was irradiated with (1064 nm) using an Nd: YAG laser with different laser energies from (200 - 350) mJ with an increase of (50 mJ) for each sample with a fixed number of pulses (100 pulses), and a pulse duration of 10 ns, and 6 Hz frequency. The laser light is fully concentrated and accurately on the target to use a lens with such a focal length of 120 mm.

To ensure successful and accurate deposition, the sample was arranged on a substrate holder inside the chamber in proportion to the laser beams. Focusing Nd: YAG it exchanges the emitted laser beam through a window or lens directed exactly at the sample surface at a 45° angle. The substrate is placed at an appropriate distance directly above the sample surface and in this arrangement nothing prevents the laser beam from falling onto the target. The deposition process was repeated several times and some factors such as the distance between the target and the substrate or the angle of the incident laser beam were changed in order to obtain a high quality of prepared thin films.

## 3-6 The Techniques of Measurement

The optical and structural properties of thin films and measuring thickness by several techniques, have been investigated.The most important of which are the following.

### 3-6-1 Measurement of Thickness

An optical interferometer technique was used to calculate the film thickness. This technique depends on the interference that occurs to the light rays reflected from the surface of the film and the base of the substrate as shown in Figure (3-3). A He-Ne laser was used in the measurement process with a wavelength of (632.8 nm) and the thickness was calculated according to the following equation [104].

$$t = \frac{\Delta S}{S} \text{x} \frac{\lambda}{2} \qquad \text{………… (3-1)}$$

where, S is the width of fringes and ΔS is the shifting that happen to fringes

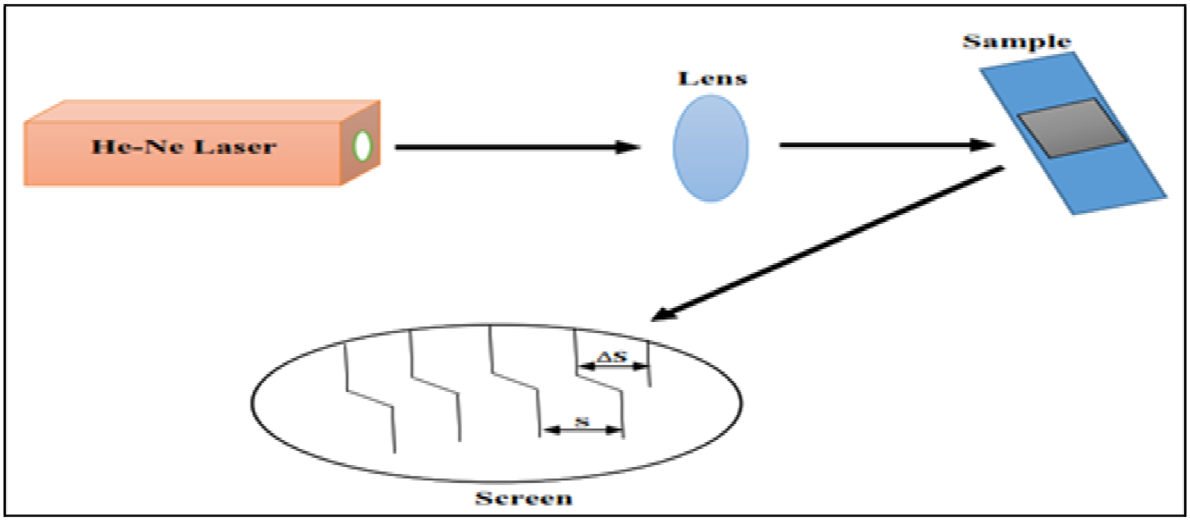

**Figure (3-3): Schematic diagram of measurement of the films thickness [105].**

## 3-6-2 Atomic Force Microscope (AFM)

Angstrom Ad – Davison Corp's atomic force microscope (AA300 Vibrating Sample Microscopy SPM, tip NSC 35/AIBS) was used to study the morphological of thin film surface. Roughness, particle size, and root mean squares (RMS) of film could all be directly measured by this technique.

## 3-6-3 X-Ray Diffraction Analysis

Given the nature data and the crystal growth process of the films made under varied deposition conditions, the XRD technique is very important for examining the characteristics of the thin film' structure. The (American Standard of Testing Material) (ASTM) cards were used to measure the XRD. With (Cu-K) radiation of (λ=1.54A°), a Philips PW 1050 X-ray diffraction measurement system was used. The structural parameter of all the prepared PbS thin films was calculated using XRD pattern.

## 3-6-4 Optical Measurement

double-beam UV-Vis Spectrophotometer was applied to study the absorption and transmittance of PbS thin films prepared under different conditions. The estimated spectral range is between (190-1100) nm, as shown in Figure (3-4). Background calibration was considered for each scan. The transmittance and absorbance measurement was used to examine the absorption coefficient of thin films at different wavelengths and with this measurement, the band gap energy of the prepared films was calculated.

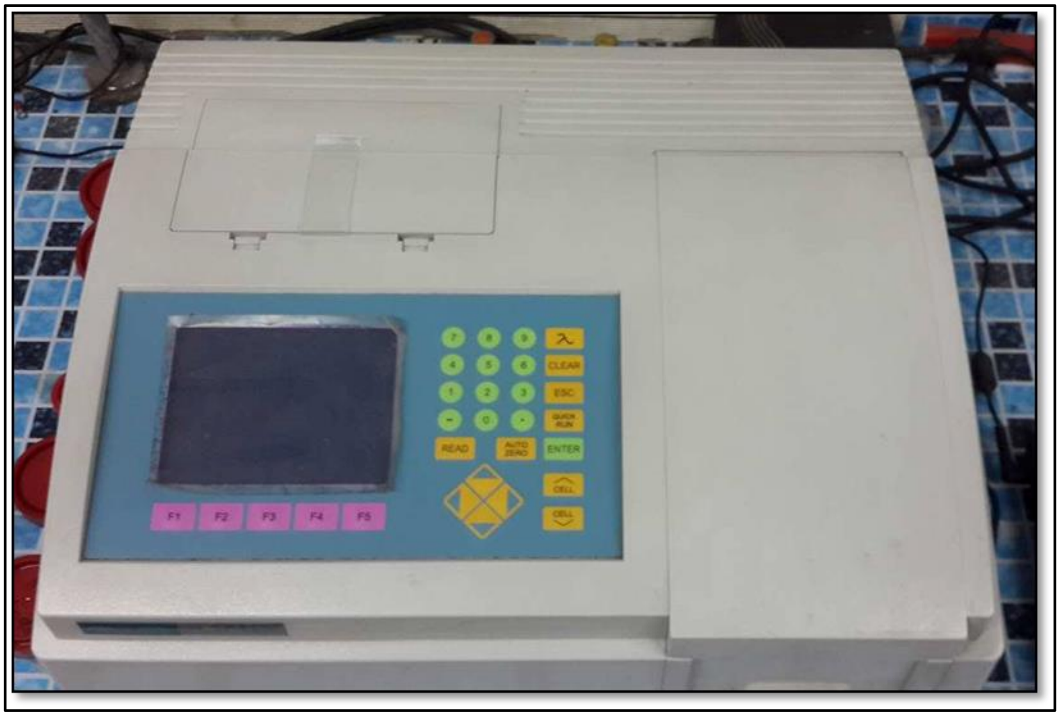

**Figure (3-4): UV- Vis –Spectrophotometer.**

## 3-6-5 Gas Sensing Measurement

An adequate setup is produced in order to determine the sensitivity parameter, which is primarily the response time and recovery time of the (PbS,PbS:Cd and PbS:Cr) gas sensors. A gas sensitive test system is seen in Figure (3-5) ,it comprises of a stainless steel cylindrical test chamber with a diameter of 30 cm and a height of 35 cm. The chamber's effective volume is 6594 cc, and it contains an inlet for the tested gas and an air inlet valve for ambient air after it has been evacuated. Electrical connections to the heater, -type-K thermocouple, and sensor electrodes are made via a multi-pin feed at the chamber's base. Inside the chamber, the heater comprises of a hot plate and a type-K thermocouple for controlling the sensor's operational temperature. The sensor current variation is recorded when exposed to a mixing ratio of $NH_3$-$NO_2$ gases using a UNI-T UT81B computer-connected digital multimeter and a laptop computer. The test gas is fed through the flow and the mixing gas is fed by zero air.

Metering and needle valve setup to achieve actual sensitivity, the mixing gas is delivered into the test chamber through a tube above the sensor.

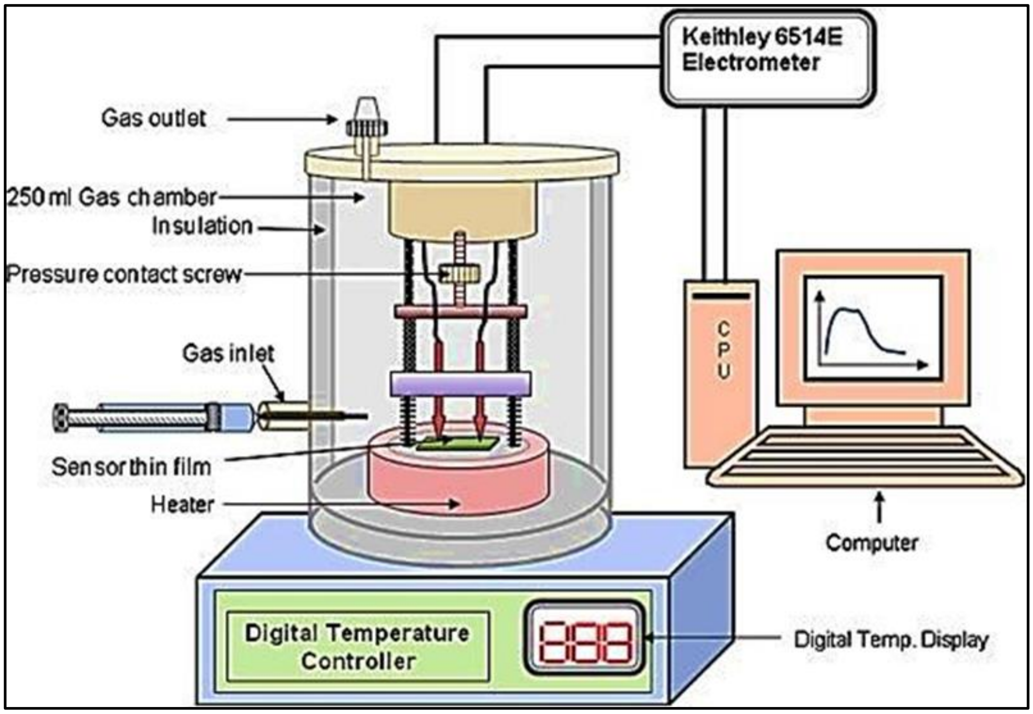

**Figure (3-5): Gas sensor testing system [106].**

## 3-6-6 Procedure for Testing Sensors

Gas sensing measurements of (PbS, PbS:Cd and PbS:Cr) thin films produced on (Si) surfaces with varying formation ratios at a constant current of 40 mA and different temperatures at ( 473,523, and 573) K to make nitrogen dioxide and ammonia gas sensors according to the following setup:

1- The sensor is put on the heater after the test chamber is opened. The test chamber was closed after the appropriate electrical connections between the feed-through pin and the sensor were formed using conductive aluminum sheets.

2-Creating a 6 volt bias voltage between the two electrodes.

3-Turn on the circulating pump to empty the test chamber to about 1 mbar, then use the temperature controller to adjust the sensor to the correct operating temperature. A schematic diagram of the electrical circuit for gas sensor measurements is shown in Figure (3-6).

4-With the needle valves, adjust the flow rate of the test gas and air, and set the volumetric concentration of the test gas in the air to 5%.

5-A digital interfacial multimeter of the type UNI-UT81B is used to measure the current contrast.

6-The digital multimeter first records the bias current of the air flow, then turns on the test gas ($NO_2$) until the current is low contrast after a few seconds, then turns off the test gas to record the recovery time.

7-Working temperatures and other gases are measured in the same way as above.

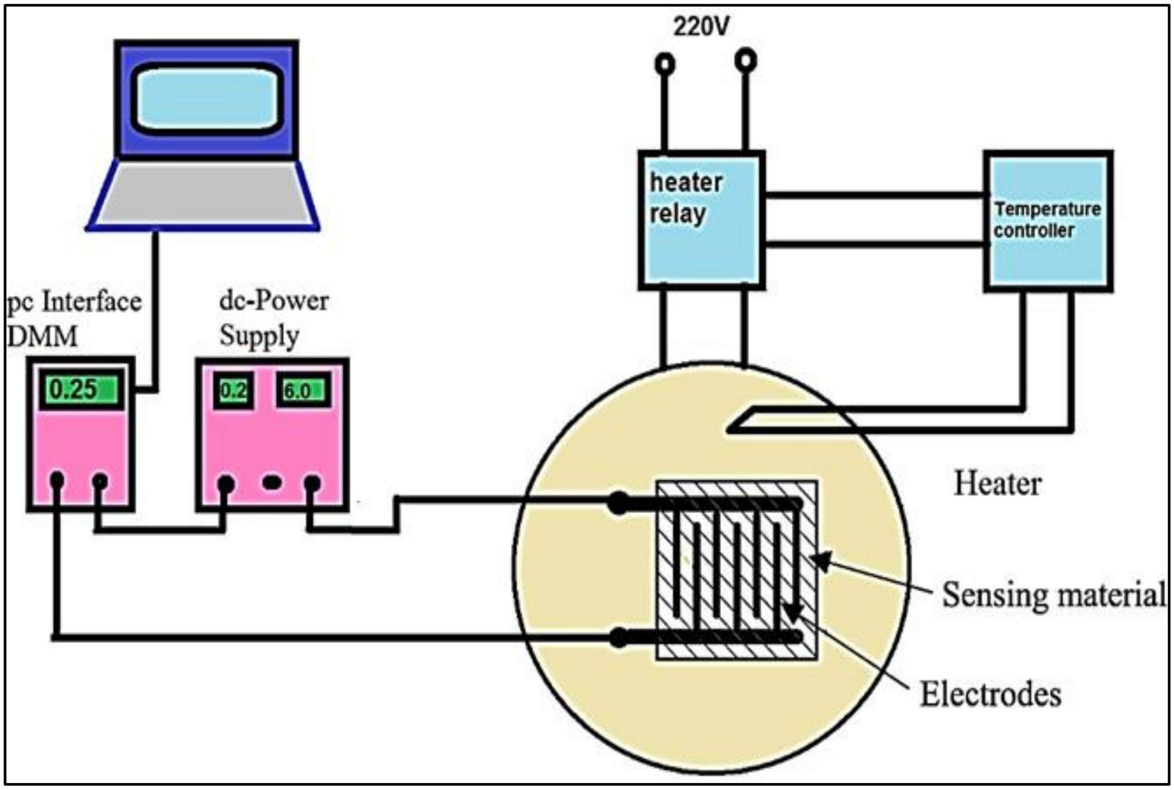

**Figure (3-6): Schematic diagram of gas sensing and the electrical circuit setup [106].**

# Chapter Four

## Results and Discussion

## 4-1 Introduction

The findings of structure, morphology, optic, and gas sensor testing of cadmium-chromium-doped PbS thin films generated on glass and silicon substrates using the pulsed laser deposition process are summarized and discussed in this chapter. The influence of laser energy at various energies (200-350) mJ was also investigated. doped rates (2, 4, 6)wt% are also discussed for all films that have been prepared.

## 4-2 Thin Film Thickness

Table (4.1) shows thickness measurement of samples deposited at RT with varied laser energy ranging from (200 – 350) mJ with a fixed number of pulses (100 pulses) on the glass substrate (notice that thickness measurements had an error rate of roughly 5.2 nm). It can be seen that as the laser energy is increased, the thickness of the films increases, implying that the laser energy is increased, more particles are removed from the target surface. As a result, the thickness of the thin films increases.

**Table 4.1: Thickness of (PbS,PbS:Cd and PbS:Cr) thin film (±5.2 nm).**

| **Sample** | **Laser Energy** mJ | **Thickness** (nm) |
|---|---|---|
| PbS | 200 | 203 |
| PbS | 250 | 227 |
| PbS:Cd | 300 | 246 |
| PbS:Cr | 350 | 261 |

# 4-3 Structural properties

## 4-3-1 X-ray diffraction

Figure (4-1) shows the X-ray diffraction pattern of PbS:Cd powder. The observed PbS:Cd diffraction peaks were indexed within the cube crystal structure PbS:Cd, which was checked with a regular card (JCPDS No. 05-0592) [107] .The vertices were portrayed as what corresponds to as pattern, they're Miller indices. Peaks which have a score above (2θ= 26.1710 °, 30.2833 °,and 43.2629 °), comply with to the planes hkl= (111), (200),and (220), planes of crystallization, accordingly. Thin tops suggest that the substance has crystalline nature and that it likes to be directed in the direction of [200]. Furthermore, the lack of any other peaks indicates that this powder is free of flaws. It was also observed that the crystallite size increased with the increase in the rate of doping with the addition of different inoculation ratios(X=2,4,6)wt% as indicated in the table(4-2).

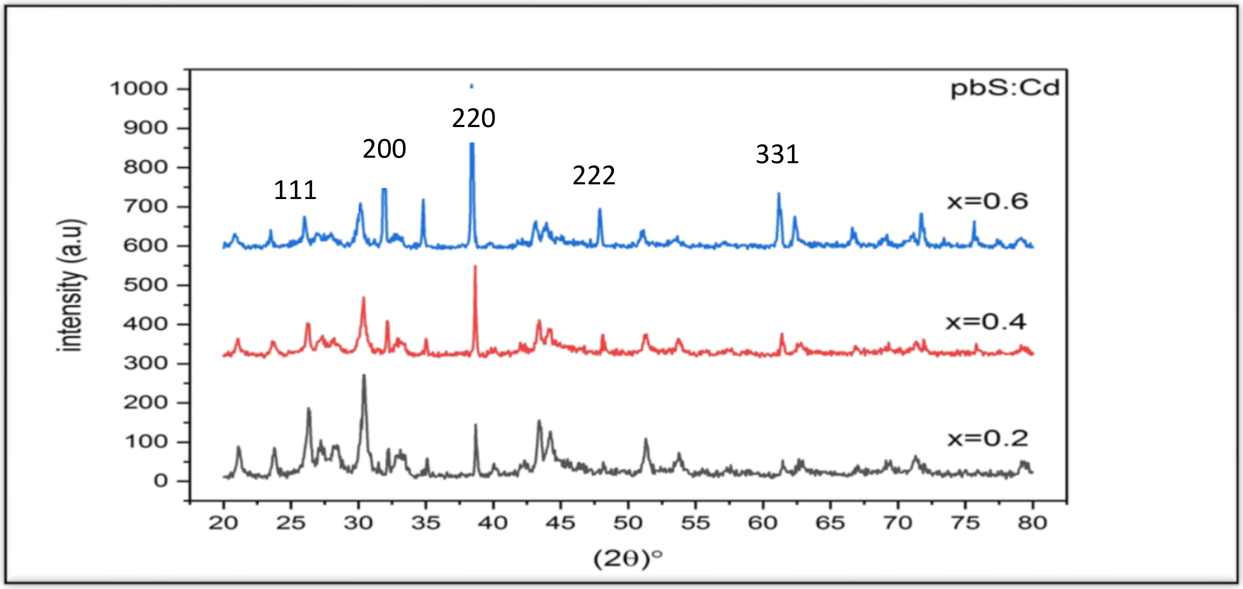

**Figure (4-1): X-ray diffraction Pattern of PbS:Cd powder.**

Figure (4-2) shows the X-ray diffraction pattern of PbS:Cr powder. The observed PbS:Cr diffraction peaks were indexed within the cube crystal structure PbS:Cr, which was checked with a regular card (04-002-0034 and 00-005-0592) [108] .

The vertices are represented by what corresponds to as spectrum, they're Miller indices. Peaks that have a rating above (2θ= 26.1710 °, 30.2833 °,and 43.2629 °). Comply with to the planes hkl= (111), (200),and (220), levels for crystallization, accordingly. Thin tops suggest that the substance has crystalline nature and that it likes to be directed in the direction of [200] Furthermore, the lack of any other peaks indicates that this powder is free of defects. It was also observed that the crystallite size increased with the increase in the rate of doping with the addition of different inoculation ratios(X=2,4,6)wt% as indicated in the table(4-2) [108].

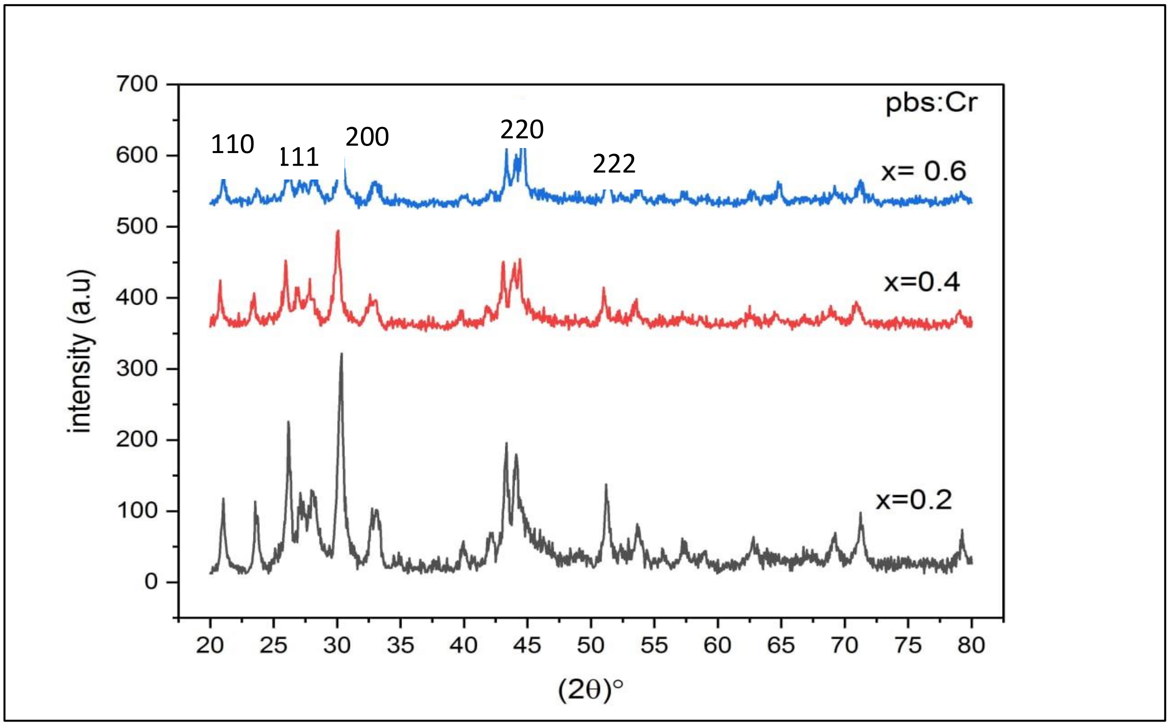

Figure (4-2): X-ray diffraction Pattern of PbS:Cr powder.

**Table (4-2): Structural parameters for PbS:Cd and PbS:Cr powder.**

| Material | $2\theta$ (Deg.) | FWHM (Deg.) | $d_{hkl}$ Exp.(Å) | C.S (nm) | $d_{hkl}$ Std.(Å) | Hkl |
|---|---|---|---|---|---|---|
| PbS:Cd<br>X= 2% | 26.3384 | 0.3606 | 3.3810 | 22.6 | 3.9581 | 111 |
| | 30.4365 | 0.3875 | 2.9345 | 21.2 | 3.8758 | 200 |
| | 39.7283 | 0.2522 | 2.3231 | 24.5 | 3.2132 | 220 |
| | 43.4213 | 0.3427 | 2.0823 | 25.0 | 3.4371 | 222 |
| | 61.342 | 0.3523 | 2.1330 | 25.5 | 3.5543 | 331 |
| X= 4% | 26.1989 | 0.1642 | 3.3987 | 49.7 | 3.3828 | 111 |
| | 30.4428 | 0.1300 | 2.9339 | 25.2 | 3.0816 | 200 |
| | 39.1095 | 0.10000 | 2.3014 | 26.2 | 3.1232 | 220 |
| | 43.4816 | 0.1048 | 2.0796 | 21.6 | 2.8370 | 222 |
| X= 6% | 26.0550 | 0.1749 | 3.4172 | 46.6 | 2.6652 | 111 |
| | 30.1431 | 0.3882 | 2.9624 | 63.3 | 2.6074 | 200 |
| | 39.4355 | 0.1044 | 2.3223 | 23.2 | 3.6733 | 220 |
| | 43.1005 | 0.2875 | 2.0971 | 29.7 | 2.5834 | 222 |
| PbS:Cr<br>X= 2% | 20.0653 | 0.4111 | 4.2139 | 18.3 | 2.4321 | 110 |
| | 26.2105 | 0.4167 | 3.3972 | 19.6 | 2.4576 | 111 |
| | 30.3050 | 0.4892 | 2.9469 | 16.8 | 2.4415 | 200 |
| | 43.3164 | 0.4233 | 2.0871 | 20.2 | 2.4211 | 220 |
| | 52.3293 | 0.2708 | 1.7469 | 18.6 | 2.41123 | 222 |
| X= 4% | 20.3368 | 0.2500 | 4.3632 | 17.8 | 2.3234 | 110 |
| | 26.9774 | 0.4438 | 3.4272 | 18.4 | 2.3816 | 111 |
| | 30.0485 | 0.5230 | 2.9715 | 15.7 | 2.2141 | 200 |
| | 43.0782 | 0.4473 | 2.0981 | 19.1 | 2.0848 | 220 |
| | 52.1564 | 0.3083 | 1.7522 | 20.3 | 2.0543 | 222 |
| X= 6% | 20.2038 | 0.0833 | 4.3916 | 23.6 | 2.0465 | 110 |
| | 26.2250 | 0.3125 | 3.3916 | 26.1 | 2.0715 | 111 |
| | 30.3928 | 0.2500 | 2.9386 | 32.9 | 1.9965 | 200 |
| | 43.3567 | 0.2358 | 2.0853 | 36.3 | 1.9646 | 220 |
| | 52.555 | 0.10000 | 1.9896 | 28.7 | 1.9543 | 222 |

In Figure (4-3), PbS thin films' X-ray diffraction pattern can be seen. The diffraction peaks throughout the observed PbS thin film are indexed inside the cube crystal structure (PbS),which was checked with a regular card (04-002-0034 and 00-005-0592) [108].The vertices are represented by what corresponds to as spectrum, they're Miller indices. Peaks which have a score of (2θ=26.1710 °, 30.2833 °,and 43.2629 °), comply with the planes hkl= (111), (200),and (220), Levels of crystal, accordingly. Thin tops indicate that the material has crystalline nature and that it likes to be oriented in the plane of [200]. Furthermore, the lack of the any other peaks reveals that the film is now without flaws, defects it was also observed that the crystallite size increased with the increase of laser energies (E=200,250,300 and 350)mj as shown in table (4-3) [108].

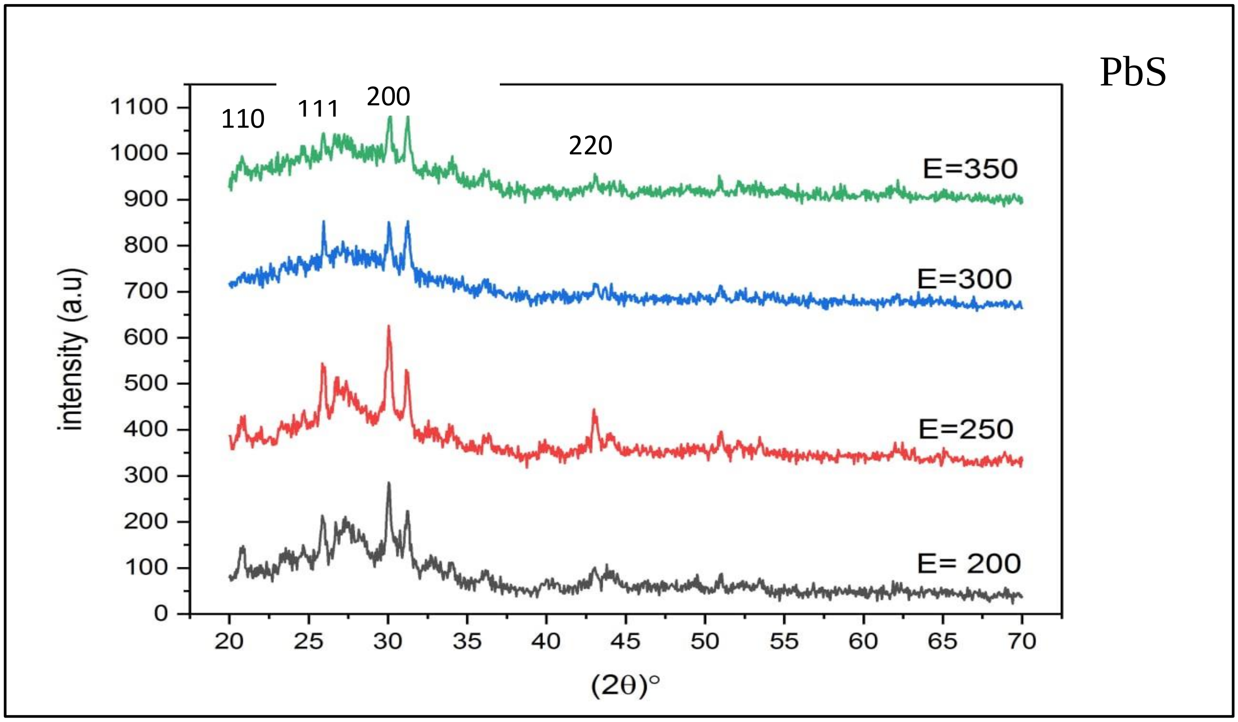

**Figure (4-3): X-ray diffraction Pattern of PbS thin films.**

Figure (4-4) shows the PbS:Cd X-ray diffraction pattern of PbS:Cd thin films thin. The diffraction peaks in the PbS:Cd film were indexed inside the cube crystal structure. PbS:Cd, which was confirmed to use a normal card (JCPDS No. 05-0592) [107]. For spectrum, the vertices are represented by what has been known as Miller indices. Peaks which have a rating of (2θ=26.1710 °, 30.2833 °,and 43.2629 °), comply with to the planes hkl= (111), (200),and (220), Levels of crystal, accordingly. Narrow tops suggest that the materials have crystalline nature and that it likes to be directed in the direction of (200). Furthermore, the lack of any additional peaks reveals that the film is now without defects .It was observed that the crystallite size increased with the increase in the rate of doping with the addition of different inoculation ratios(X=2,4,6)wt% as indicated in the table(4-3) [107].

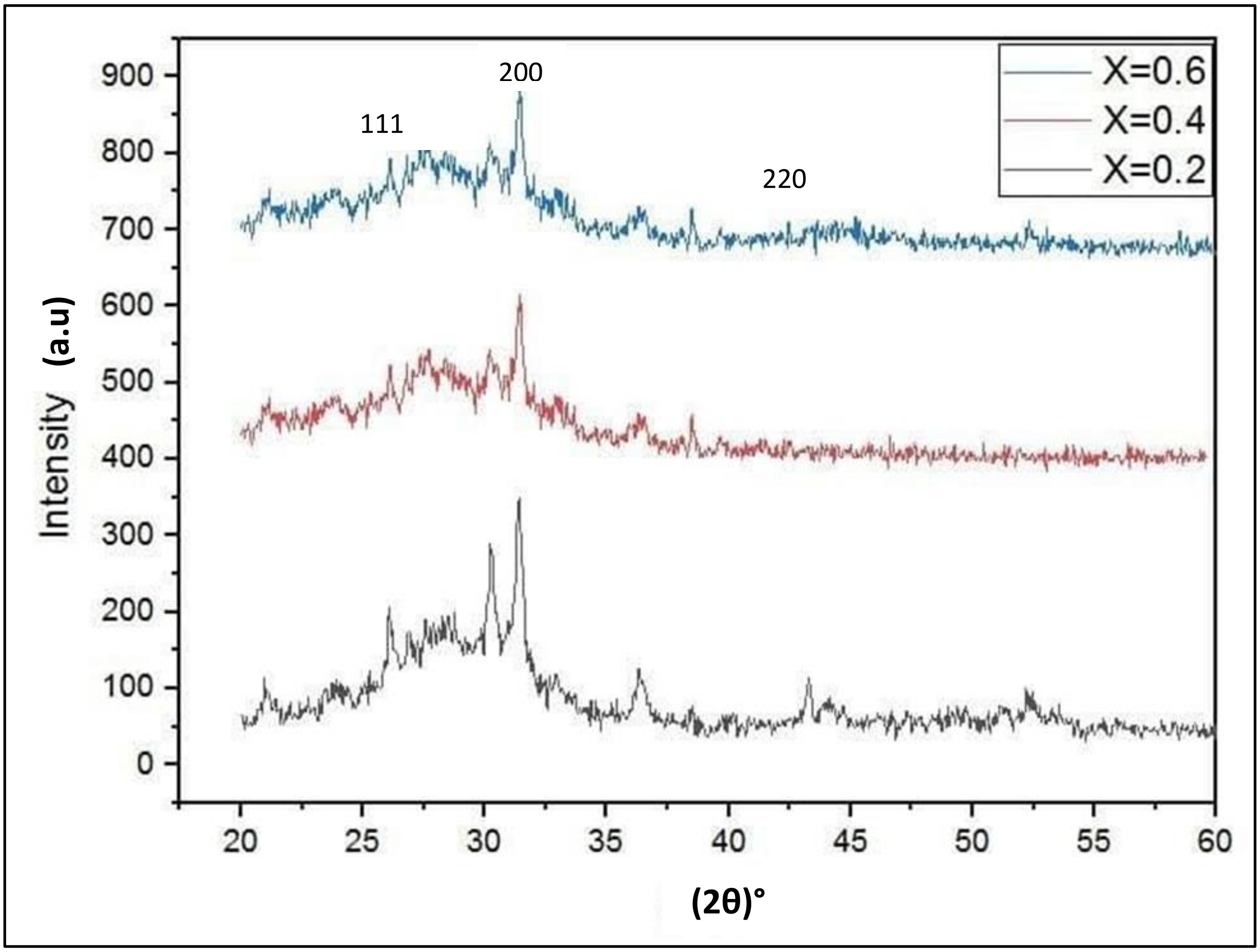

**Figure (4-4): X-ray diffraction Pattern of PbS:Cd thin films at laser energy(350)mj.**

The X-ray diffraction pattern of PbS:Cr thin films is shown inFigure (4-5). The peak intensity in the PbS:Cr films is indexed inside the cube crystal. structure (PbS:Cr), which was checked with a regular card (04-002-0034 and 00-005-0592) [108]. From the pattern, the vertices are denoted by what has been known as Miller indices. Peaks which have a rating of (2θ=26.1710 °, 30.2833 °,and 43.2629 °), complies with to the planes hkl= (111), (200),and (220). Narrow tops suggest that the materials has crystalline nature and that it likes to be directed in the direction of (200). Also, the lack of any other peaks reveals that the film is now without defect. It was also observed that the crystallite size increased with the increase in the rate of doping with the addition of different inoculation ratios (X=2,4,6) wt% as indicated in the table(4-3) [108].

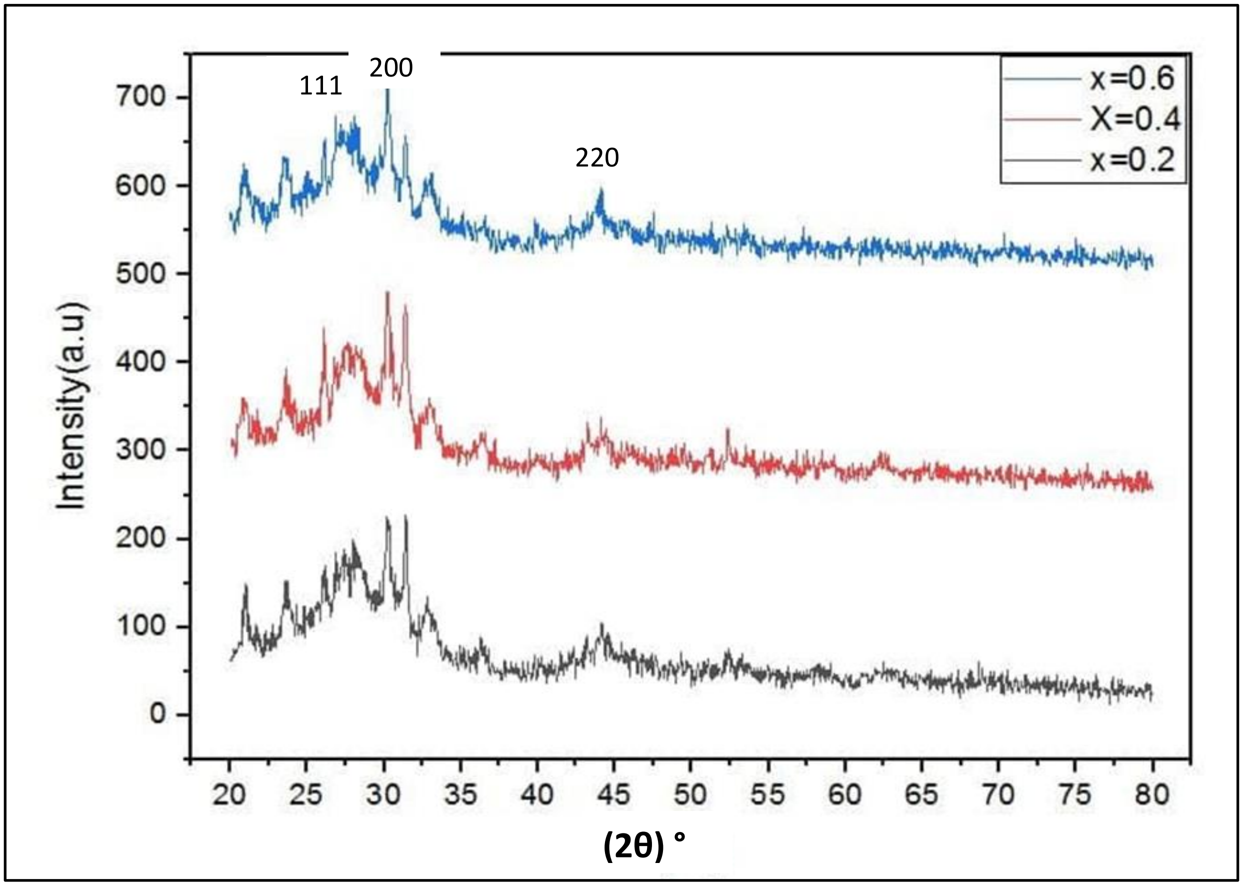

**Figure (4-5): XRD Pattern of the PbS:Cr thin films at laser energy(350)mj.**

**Table (4-3): Structural parameters for PbS, PbS:Cd and PbS:Cr thin films**

| Materal | 2θ (Deg.) | FWHM (Deg.) | $d_{hkl}$ Exp.(Å) | C.S (nm) | $d_{hkl}$ Std.(Å) | hkl |
|---|---|---|---|---|---|---|
| PbS E=200 mJ | 20.8271 | 0.3690 | 4.2552 | 21.9 | 3.8758 | 110 |
| | 26.7979 | 0.5334 | 3.4350 | 15.3 | 3.0816 | 111 |
| | 30.0893 | 0.4461 | 2.9676 | 18.4 | 2.8370 | 200 |
| E= 250 mJ | 20.8231 | 0.3690 | 4.2552 | 21.9 | 2.6074 | 110 |
| | 26.7979 | 0.7500 | 3.5038 | 10.9 | 2.3816 | 111 |
| | 30.0827 | 0.4399 | 2.9682 | 25 | 3.8758 | 200 |
| E=300 mJ | 20.8769 | 0.2333 | 4.2552 | 21.9 | 3.0816 | 110 |
| | 26.0057 | 0.3800 | 3.5242 | 21.4 | 2.8370 | 111 |
| | 30.0859 | 0.4084 | 2.9679 | 30 | 2.6074 | 200 |
| E= 350 mJ | 20.2620 | 0.5083 | 4.2608 | 15.9 | 2.4415 | 110 |
| | 26.8578 | 0.3867 | 3.4274 | 20.1 | 2.3816 | 111 |
| | 30.1319 | 0.4083 | 2.9634 | 34 | 3.8758 | 200 |
| PbS:Cd X= 2% | 26.1710 | 0.4894 | 3.4023 | 16.7 | 3.4371 | 111 |
| | 30.2833 | 0.4557 | 2.9490 | 18.1 | 3.0816 | 200 |
| | 43.2629 | 0.3001 | 2.0896 | 28.5 | 2.8370 | 220 |
| X= 4% | 26.1456 | 0.3733 | 3.4055 | 21.8 | 2.6074 | 111 |
| | 30.2596 | 0.1333 | 2.9140 | 57 | 2.4415 | 200 |
| | 43.2000 | 0.4000 | 2.1004 | 21.4 | 2.3816 | 220 |
| X= 6% | 26.1291 | 0.3852 | 3.4076 | 21.2 | 2.2141 | 111 |
| | 30.3451 | 0.6955 | 2.9432 | 61 | 2.0848 | 200 |
| | 43.2318 | 0.1500 | 2.0683 | 11.8 | 3.8758 | 220 |
| PbS:Cr X= 2% | 26.1476 | 0.4472 | 3.4053 | 18.2 | 3.4371 | 111 |
| | 30.2798 | 0.5180 | 2.9493 | 15.9 | 3.3828 | 200 |
| | 43.2068 | 0.4750 | 2.0921 | 18.0 | 3.0816 | 220 |
| X= 4% | 26.1137 | 0.4151 | 3.4096 | 19.6 | 2.8370 | 111 |
| | 30.2632 | 0.5505 | 2.9509 | 23 | 2.6652 | 200 |
| | 43.2817 | 0.6000 | 2.0887 | 14.2 | 2.6074 | 220 |
| X=6% | 26.1490 | 0.6500 | 3.4051 | 12.5 | 2.5834 | 111 |
| | 30.2409 | 0.7292 | 2.9530 | 44 | 2.4415 | 200 |
| | 43.4316 | 0.6500 | 2.0819 | 13.2 | 2.3816 | 220 |

## 4-3-2 Atomic Force Microscope (AFM)

Figures (4-6),(4-7) and (4-8) show atomic force microscope (AFM) images of pure cadmium-chromium-doped PbS films deposited on glass slides using PLD process kept at room temperature.The AFM picture reveals that the films are well adherent and homogeneous, with an average particle diameter of less than (100 nm) for all deposited films, as given in table (4-4), and that the average particle diameter decreases with increasing laser energy for all films. for pure thin films, the average diameter of the particles grows as the percentage of manufactured thin films increases. This is the end outcome. The doping ratio causes the produced films to have a high crystalline structure and homogeneity. In other words, when laser energy and doping ratio increase, the interplanetary distance between atoms decreases while the average crystal size increases. as a result, the produced films' uniformity and crystal structure are improved. It was also found that as the laser energy increases, the diameter of the particles decreases.

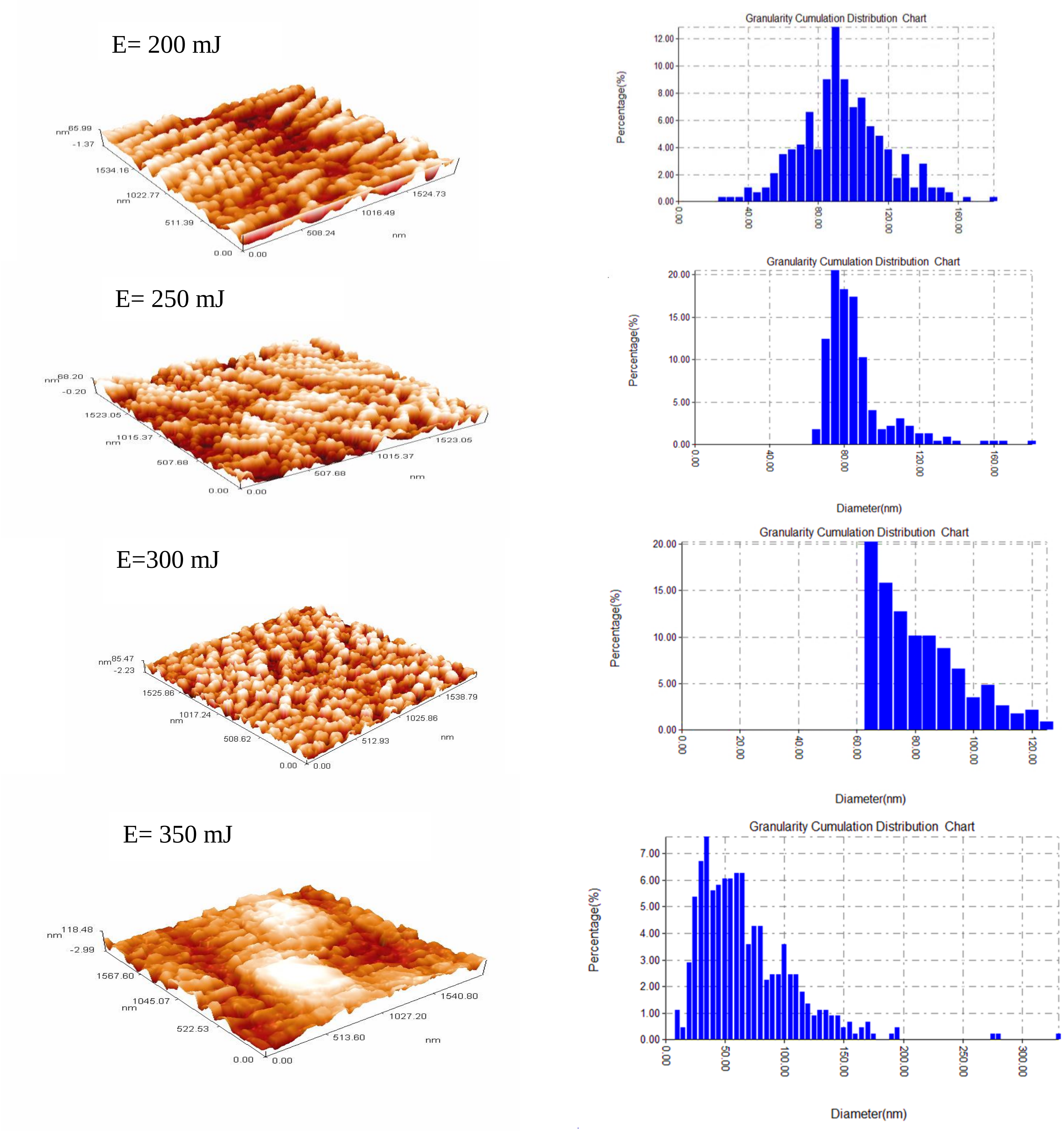

**Figure (4-6): AFM image of PbS thin films at laser energies range (200 - 350)mJ**

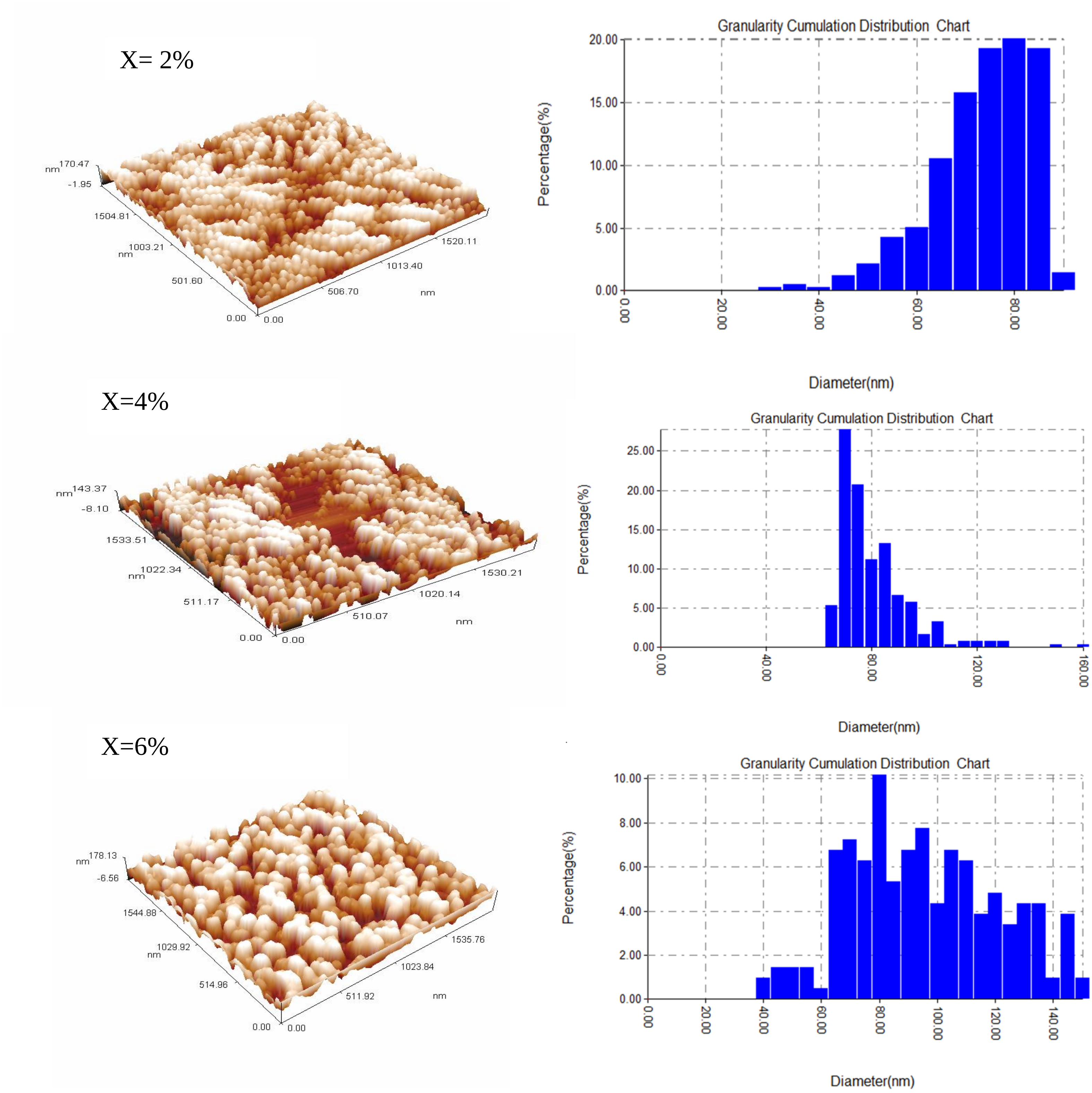

Figure (4-7): AFM image of different concentration ratios of PbS:Cd thin films.

X=2%

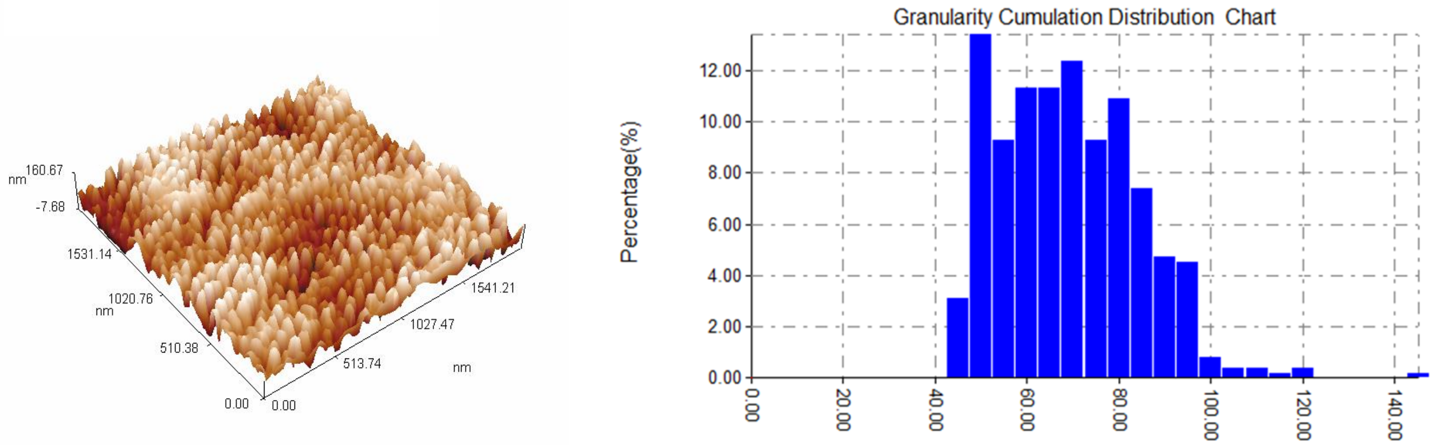

X=4%

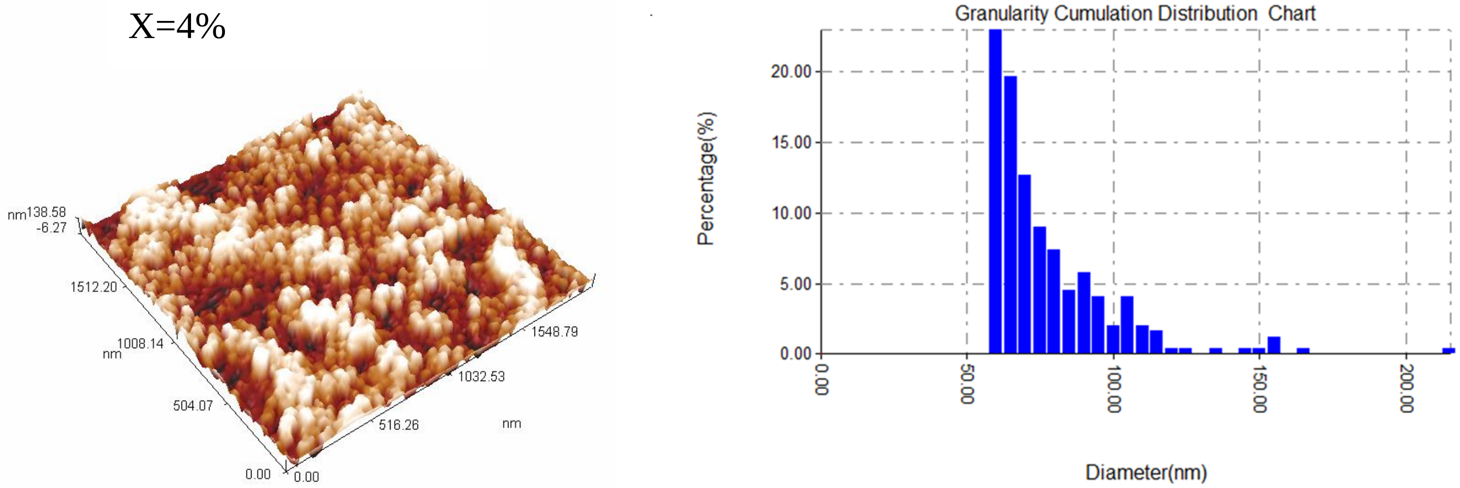

X=6%

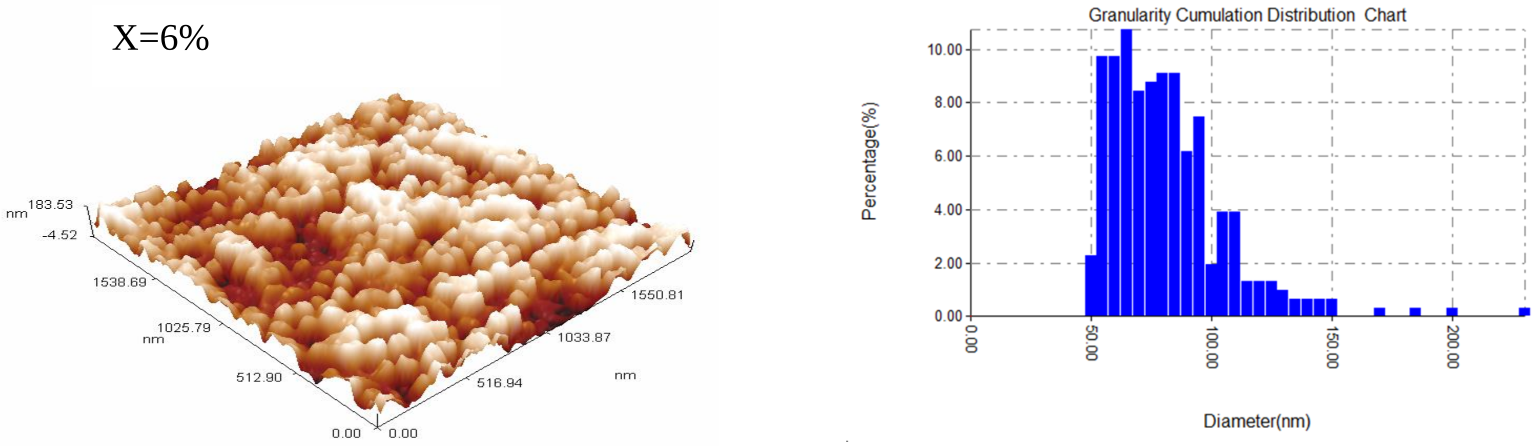

**Figure (4-8): AFM image of PbS:Cr thin films at different doping ratio**

**Table (4-4): AFM parameters for PbS, PbS:Cd and PbS:Cr thin films at various laser energy and different doping ratio.**

| Material | Average diameter (nm) | Root mean Square (nm) | Average Roughness (nm) |
|---|---|---|---|
| **PbS**<br>**E=200mJ** | **92.02** | **16.6** | **14.1** |
| **E=250 mJ** | **83.65** | **18.7** | **16.1** |
| **E= 300mJ** | **79.00** | **23.1** | **19.7** |
| **E=350mJ** | **65.75** | **24.9** | **20.5** |
| **PbS:Cd**<br>**X=2%** | **71.07** | **40.1** | **33.4** |
| **X=4%** | **78.42** | **43.7** | **37.9** |
| **X=6%** | **93.16** | **49.8** | **42.7** |
| **PbS:Cr**<br>**X=2%** | **66.83** | **35.2** | **28.9** |
| **X=4%** | **75.15** | **39.9** | **34.3** |
| **X=6%** | **79.30** | **46.9** | **39.9** |

## 4-4 Optical Properties

The absorption spectrum, optical energy gap, and absorption coefficient, as well as other optical constants, of PbS, PbS:Cd and PbS:Cr thin films produced by PLD technique on a glass substrate at RT with different laser energy and doping ratios were analyzed were described for all the generated films.

### 4-4-1 The Absorption Spectrum

A UV-VIS spectrophotometer was used to examine the absorption spectrum of pure PbS thin films deposited at room temperature on glass substrates with varied laser energy in the wavelength range (190-1100) nm [109] .

Figure (4-9) depicts the absorbance spectra as a function of wavelength for various laser energy ranging from (200 -350) mJ and a set number of pulses (100). The highest absorption occurs at 306 nm, as shown in this diagram. With increasing laser energy from (200-350)mJ, the absorption of films similarly increases. It's possible that this behavior is attributable to the removal of additional atoms from the target surface. As a result, the thickness of the thin films increases. This is validated by measuring the film thickness, which results in a high absorption rate. Increasing the laser energys can also reposition and rearrange the atoms, improving the films' crystalline structure. As a result, the average particle size decreases, resulting in increased thin films absorption. The average visible absorption of the films rises as a result of a variety of causes, the most significant of which is the thickening of the films, which results in less scattering and greater photon absorption. The optical absorption of the produced films is affected by a number of parameters, including the crystal structure and surface form of the films. The laser energy of all films created with the PLD approach was found to have a significant impact on the optical absorption measurement in the current study.

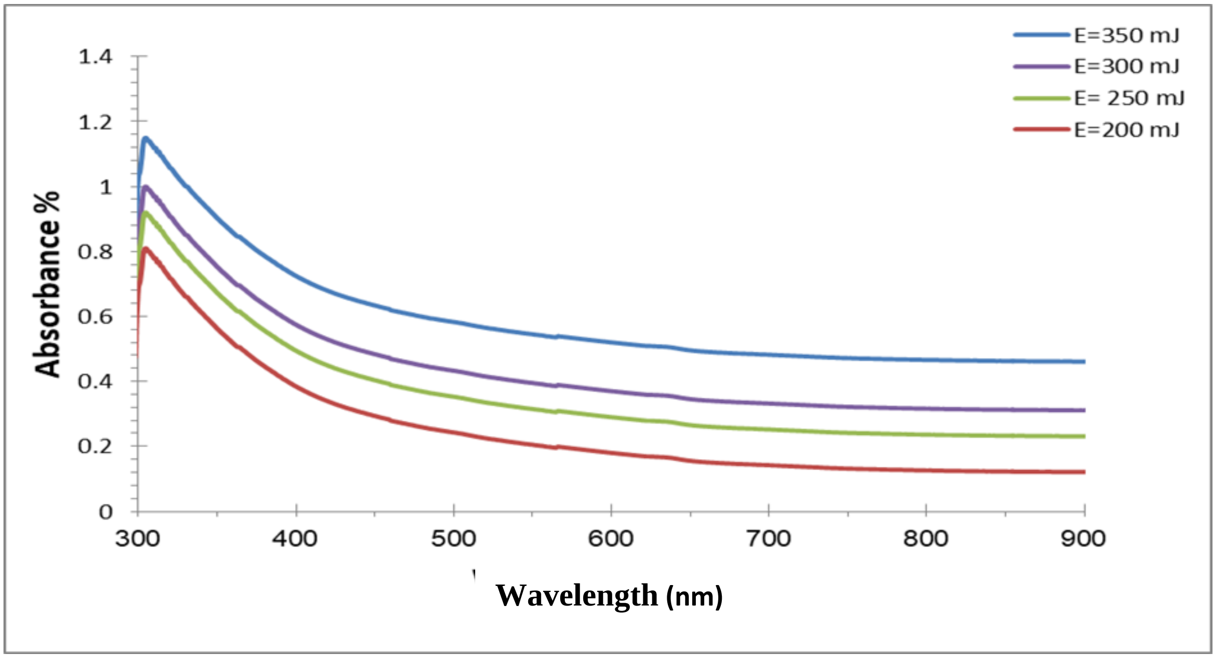

**Figure (4-9): Absorption spectra of PbS thin films at different laser energy**.

Figure (4-10) shows the absorbance spectrum as a function of wavelength in the wavelength UV-VIS spectrophotometer range of PbS:Cd thin films deposited at room temperature on the glass substrates with different ratio of doping [107]. It can be seen from this figure that the maximum absorption occurs at 200 nm. Also, the films absorbance increases with the increase of doping ratio (2,4,6)wt%. This conduct can be due to that more atoms are removed from the target surface. Which, leads to the thin films thickness to increase which causes high absorption [107].

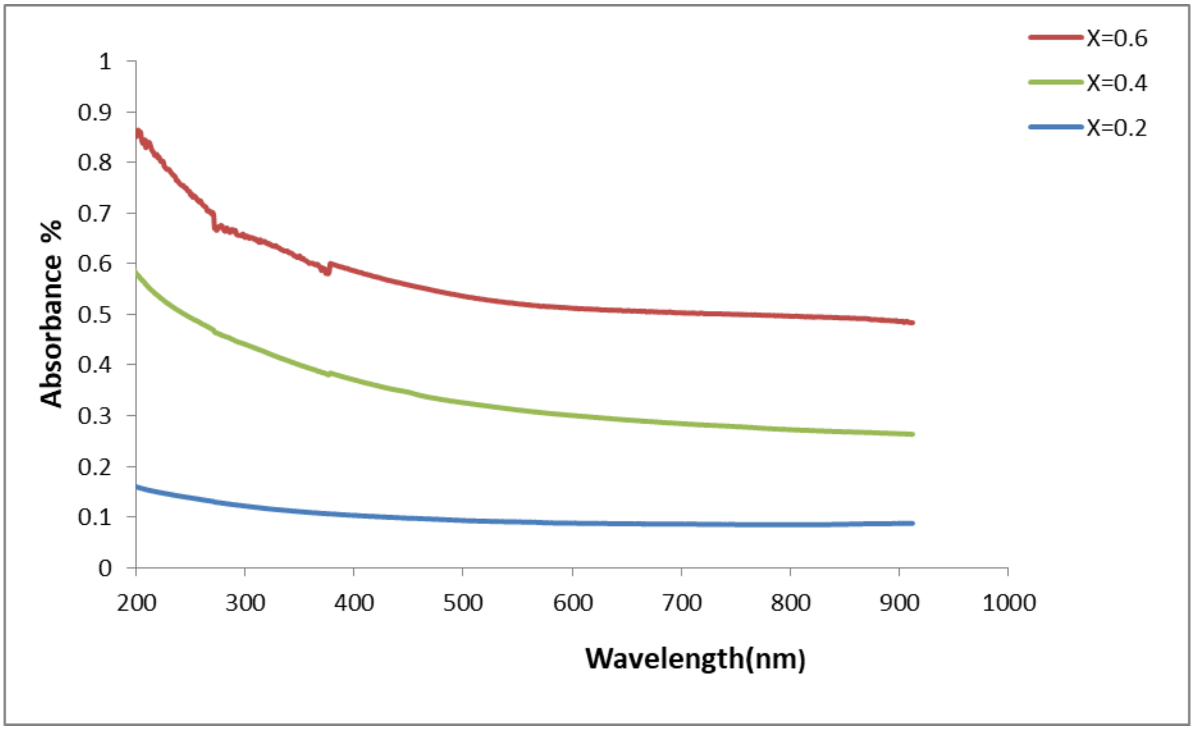

**Figure (4-10) Absorption PbS:Cd thin film spectrum at various doping ratios**.

Figure (4-11) shows the absorption spectrum of PbS:Cr thin films deposited at room temperature on glass substrates with higher concentration ratios as a function of the wavelength in the UV-VIS spectrophotometer wavelength range [108]. The absorption edge is located at 450 nm, as shown in this diagram. In fact, as the doping ratio rises (2,4,6)wt%, the film's absorbance. goes up. This activity could be due to the loss of more atoms from the target surface. As a consequence, the thickness of thin films increases, resulting in high absorption [108].

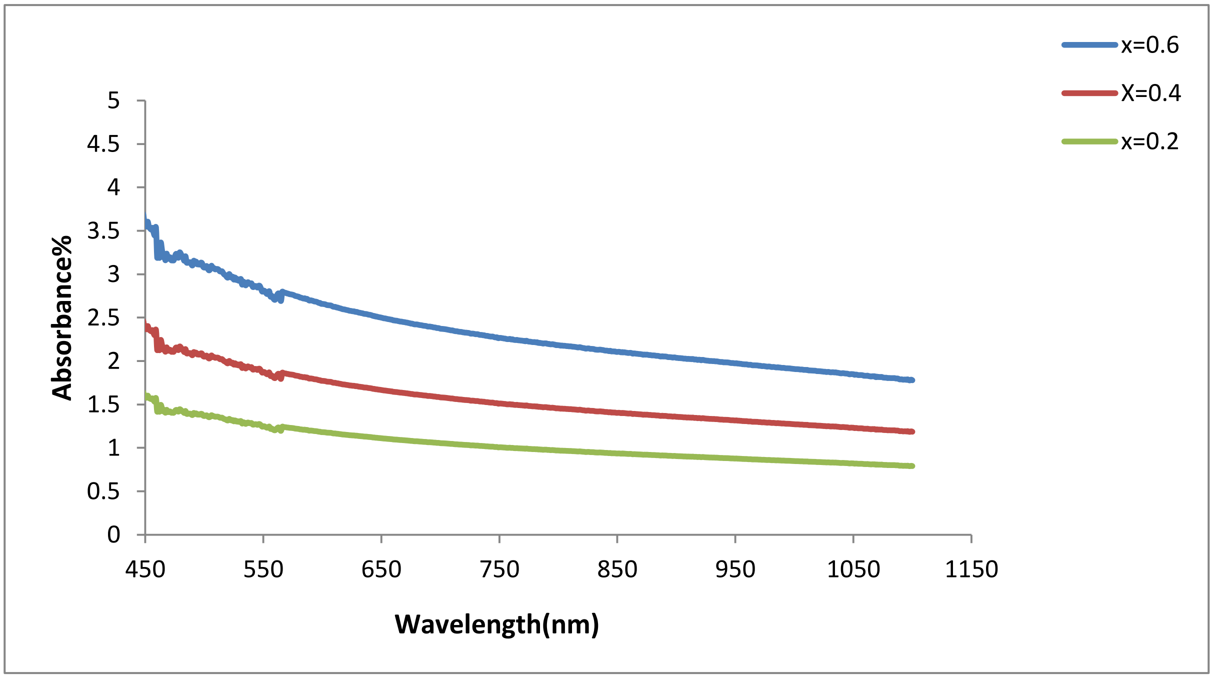

**Figure (4-11): PbS:Cr thin film absorption spectra at various doping ratios.**

## 4-4-2 The Absorption Coefficient

Figure (4-12) shows the variation in the absorption coefficient (α) of PbS thin films as a function of wavelength for different laser energy ranging from (200 – 350) mJ and a set number of pulses (100 pulses). The absorption coefficient (α) was calculated at edge's region of high absorption. As can be seen in this diagram, raising the laser energy increases the absorption coefficient for all produced films, owing to the increased thickness of the film as the laser energy increases. These findings were found to be in agreement with [108]. It should be noticed that the absorption coefficient was higher than ($10^4$ $cm^{-1}$) as indicated in Table (4-5). This establishes that electronic entries are of direct allowed transmissions type.

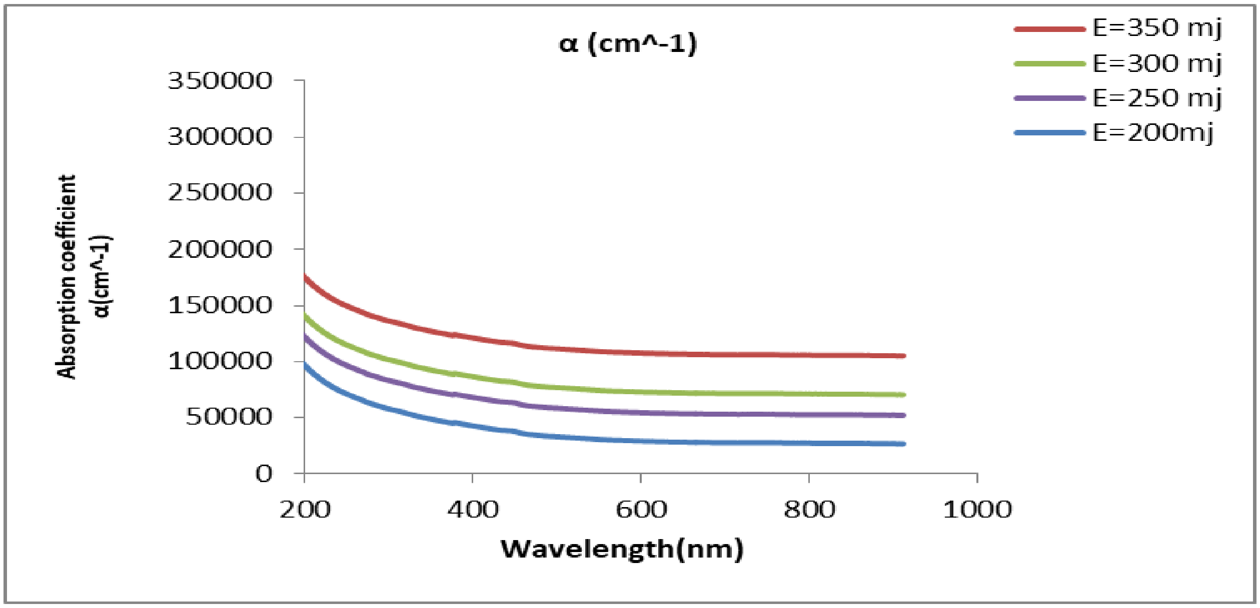

**Figure (4-12): Changing of the absorption coefficient (α) for PbS film at varied laser energy as a function of wavelength.**

Figure (4-13) shows the changing of the absorption coefficient (α) for PbS:Cd thin films as a function of the wavelength various ratio of doping (2,4,6)wt%. From the area of high absorption, the absorption coefficient (α) was computed. It can be seen from this figure that the absorption coefficient increases with the increase of doping ratio (2,4,6)wt% . Absorption coefficient increases due to the increased film thickness with increasing doping ratio. It should be noticed that the absorption coefficient was higher than ($10^4$ $cm^{-1}$) as indicated in Table (4-5). This establishes that electronic entries are of the direct transmission [107].

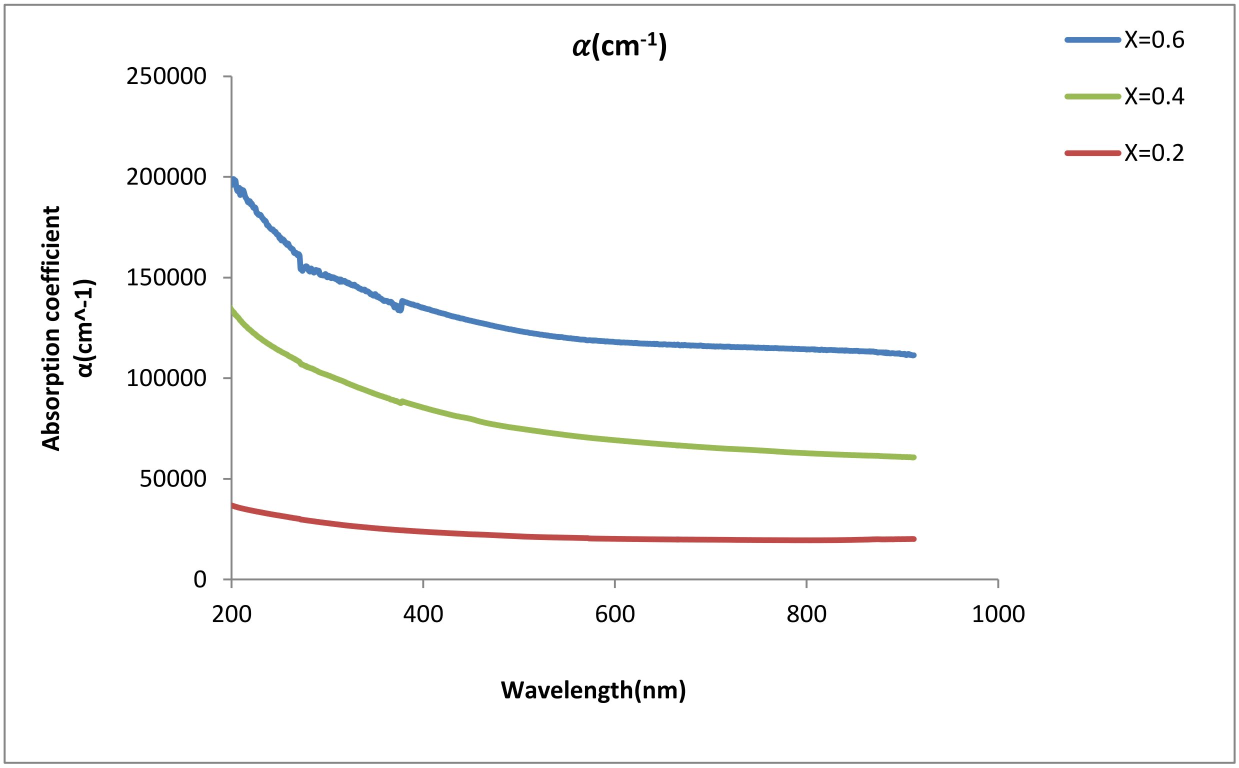

**Figure (4-13): changing of the absorbance coefficient (α) for PbS:Cd films with varying doping ratios as a function of wavelength.**

Figure (4-14) shows the switching calculating the absorption coefficient (α) for PbS:Cr thin films as a function of wavelength with various doping ratios (2,4,6)wt% . The rate of absorption increases as you move away from an area of high absorption. As can be seen in this graph, raising the dope ratio increased the absorption coefficient so because film thickness increased with the doping ratio. It should be noticed that the absorption coefficient was higher than ($10^4$ $cm^{-1}$) as indicated in Table (4-5). This establishes that electronic entries are of the direct transmissions [108].

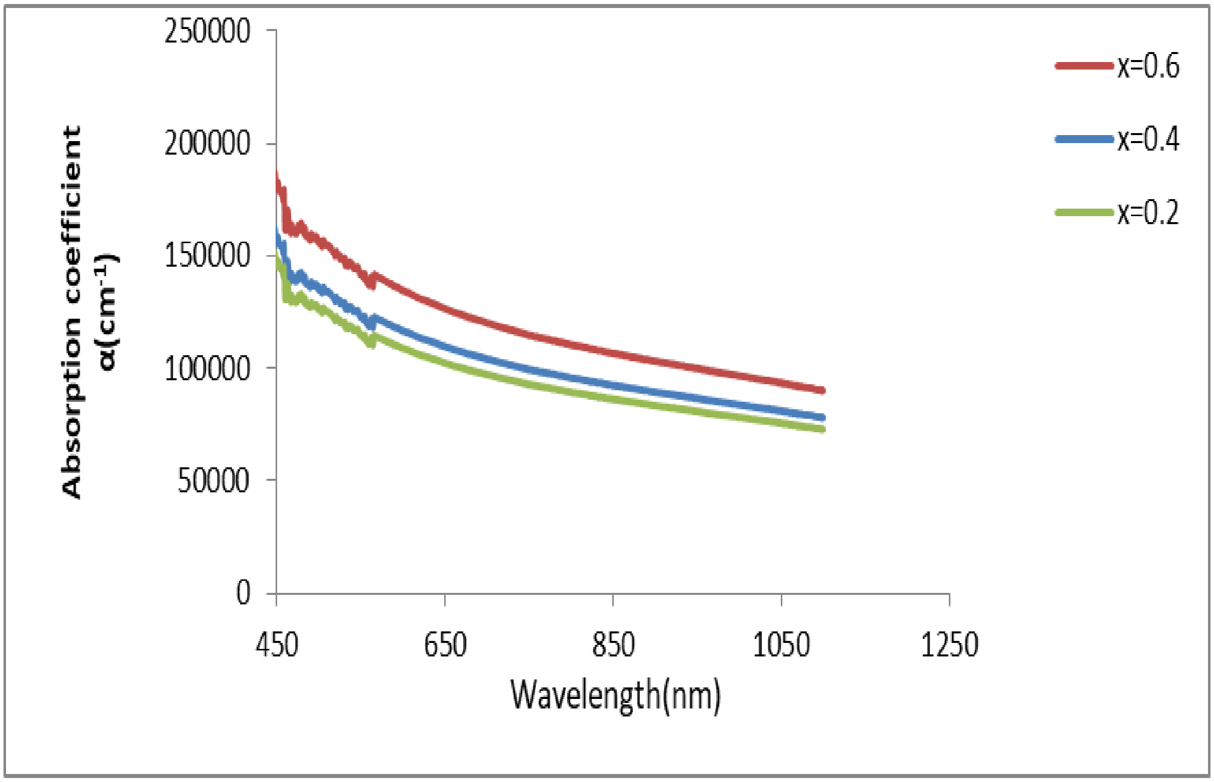

**Figure (4-14): The absorption coefficient (α) of PbS:Cr films with varying doping ratios varies with wavelength.**

## 4-4-3 Optical Energy Gap

In order to calculate the optical energy gap of PbS thin films prepared by PLD method on a glass plate at RT with different laser energy from (200 – 350) mJ, the quantity $(\alpha h\upsilon)^r$ is plottedwith the photon energy $(h\upsilon)$ as shown in Figure (4-15).The intersection with the photon energy axis at the anticipated linear portion of the curve $(\alpha h\upsilon)^r=0$, represents the energy gap values of the prepared films recorded in Table(4-5). The direct band hole of the films changes towards lower energy as shown in this diagram, which means that the energy of the optical band gap is affected by laser energy and increases as laser energies increase, as seen in Figure (4-15). This finding was found to be consistent with [109], which was produced using a different method. The increase in the optical energy gap can be explained by the fact that raising the laser intensity causes the atoms to rearrange, resulting in a better crystalline structure of the films. This is consistent with the experimental findings of the XRD and AFM analyses, which revealed a drop in average particle size, which leads to enhanced membrane adsorption and, as a result, an increase in the energy gap.

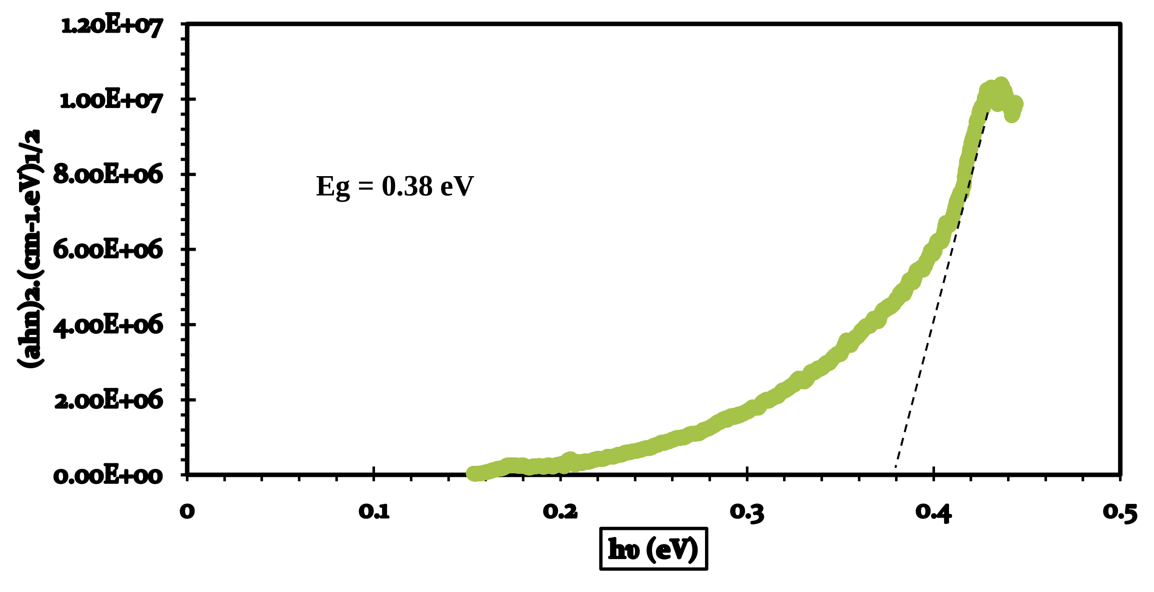

**Figure (4-15):** $(\alpha h\upsilon)^{1/2}$ **versus photon energy for PbS films with different laser energies.**

The optical energy gap of PbS:Cd thin films deposited on glass substrate with PLD technique at RT with different doping ratios (2,4,6)wt% was determined. The quantity $(\alpha h\upsilon)^2$ is plotted with the photon energy (hυ) as shown in figure (4-16) .The intersection of the estimated linear section of the curve with the photon energy axis at $(\alpha h\upsilon)^r$= 0 which represents the energy gap values of the prepared films and recorded in Table (4-5). The band gap hole of the films is seen in this diagram. Shifts towards lower ratios, which means that the optical bandgap energy is affected by the doping ratios and increases with the increase in the doping ratios, as shown in Figure (4-16) .This result was found to be consistent with [107], which was produced using a different method. The increase in the optical energy band gap can be explained by the fact that an increase in the rate of doping leads to a rearrangement of the atoms, which leads to a better crystalline structure of the films. This is consistent with the experimental results of XRD and AFM analyses, which revealed an increase in the average particle size, which leads to enhanced membrane adsorption and, as a consequence, an increase in the energy gap [107].

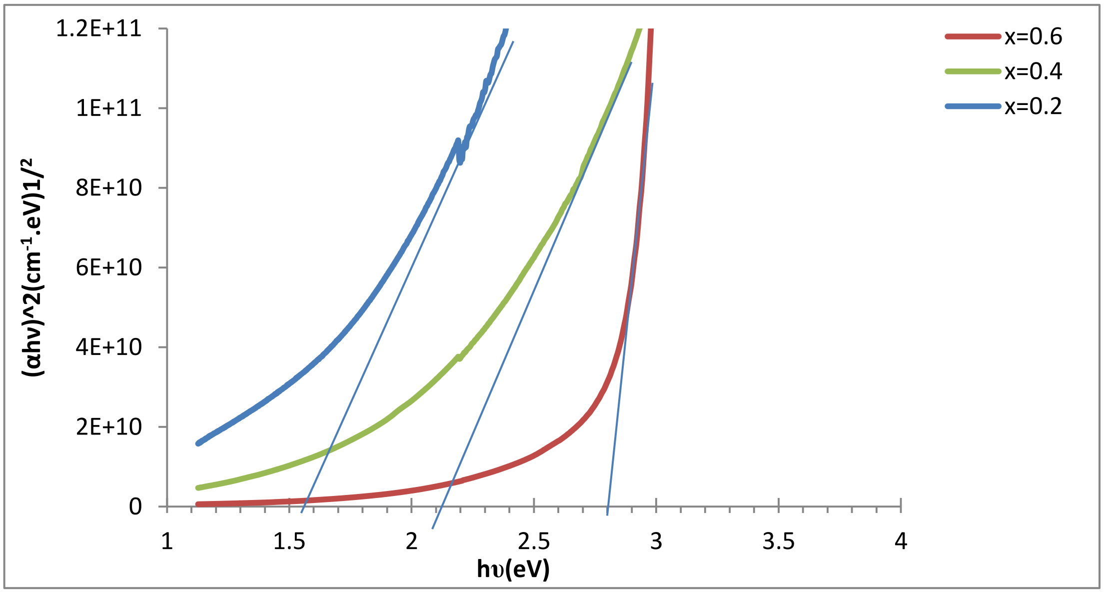

**Figure (4-16):** $(\alpha h\upsilon)^{1/2}$ **versus photon energy for PbS:Cd films with different doping ratios.**

The optical bandgap of PbS:Cr thin films deposited on glass substrate with PLD technique at RT with different doping ratios (2,4,6)wt% was determined.The quantity $(\alpha h\upsilon)^2$ and how it changes with the photon energy (hυ) as shown in Figure

(4-17) was obtained The intersection of the estimated linear section of the curve with the photon energy axis at $(\alpha h\upsilon)^{r}= 0$ which represents the energy gap values of the prepared films and recorded in Table (4-5) [108]. In this diagram, the direct band hole of the films can be seen. Shifts towards lower ratios, implying that the optical bandgap energy is influenced by doping ratios and increases as doping ratios increase, as illustrated in Figure (4-17) This finding was discovered to be consistent with, which was obtained by a different method. The rise in the optical energy band gap can be explained by the fact that increasing the doping rate causes atoms to rearrange, resulting in a better crystalline structure of the films. This is in line with the findings of XRD and AFM experiments, which demonstrated a rise in average particle size, which leads to enhanced membrane adsorption and, as a consequence, an increase in the energy gap[108].

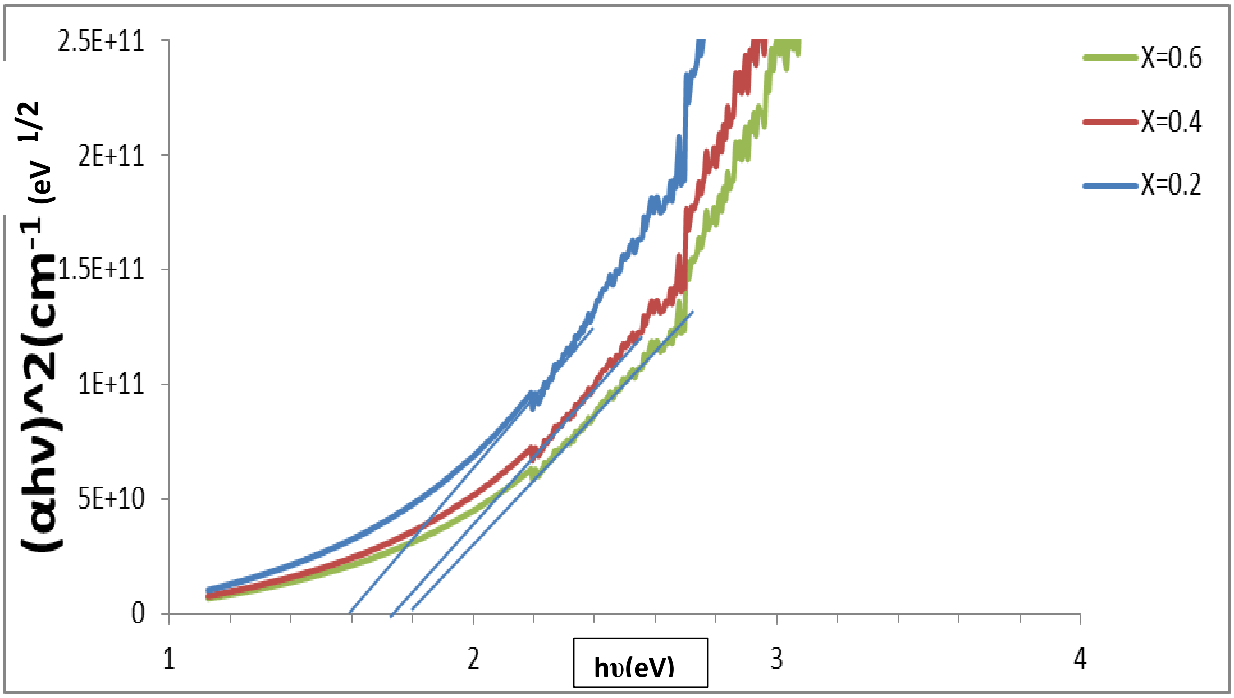

**Figure (4-17):** $(\alpha h\upsilon)^{1/2}$ **versus photon energy for PbS:Cr films with different doping ratios.**

## 4-4-4 Extinction Coefficient

Figure (4-18) illustrates the extinction coefficient (K) as a function of wavelength for pure PbS thin films formed at RT with varied laser energys ranging from (200-350) mJ at a fixed number of pulses (100 pulses). The extinction coefficient increases as the laser energy increases from (200 -350) mJ, as shown in this graph. When compared to the behavior of the absorption coefficient, this behavior is similar and conforms with the equation (2-12). For PbS thin films made using a different process, the extinction coefficient found in Table (4-5) [110].

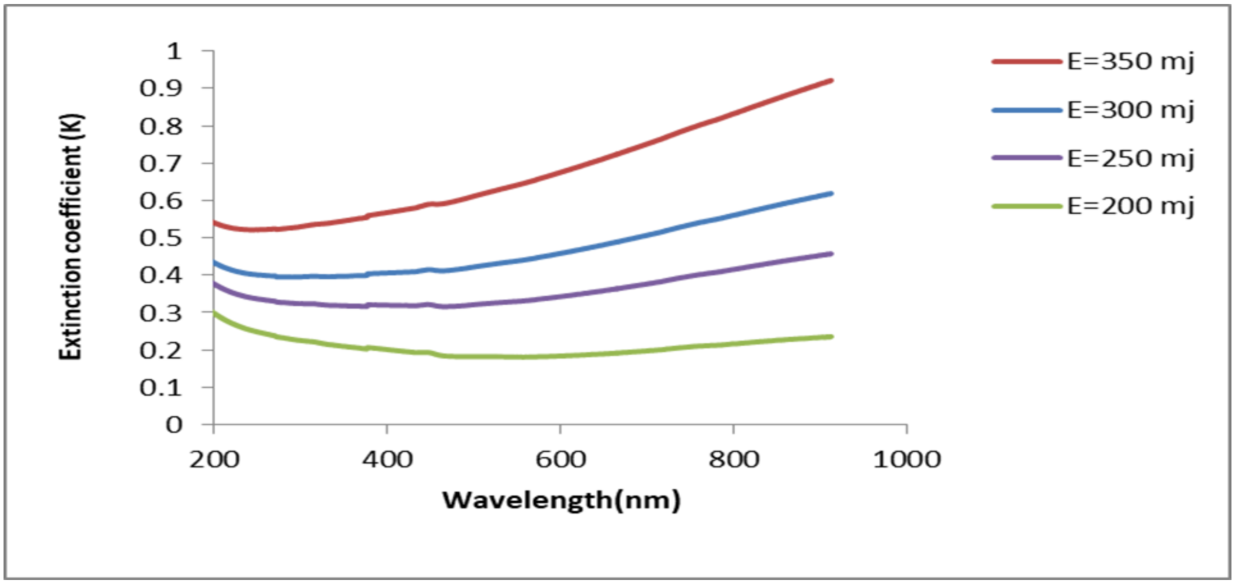

**Figure (4-18): shows the extinction coefficient (k◦) of PbS thin films changes with wavelengths at different laser energies,.**

The extinction coefficient (K◦) of pure PbS:Cd thin films produced at RT with varied doping ratios ranging (2,4,6 )wt% at a fixed number of pulses (100 pulses) [107], is shown in Figure (4-19). As seen in this graph, the extinction coefficient rises as the doping ratio rises ( 2,4,6)wt%. When compared to the absorption coefficient's behavior, this behavior is similar and correlates to equation (2-12). The extinction coefficient in Table (4-5) is identical to for thin films manufactured of PbS:Cd using a different technique.

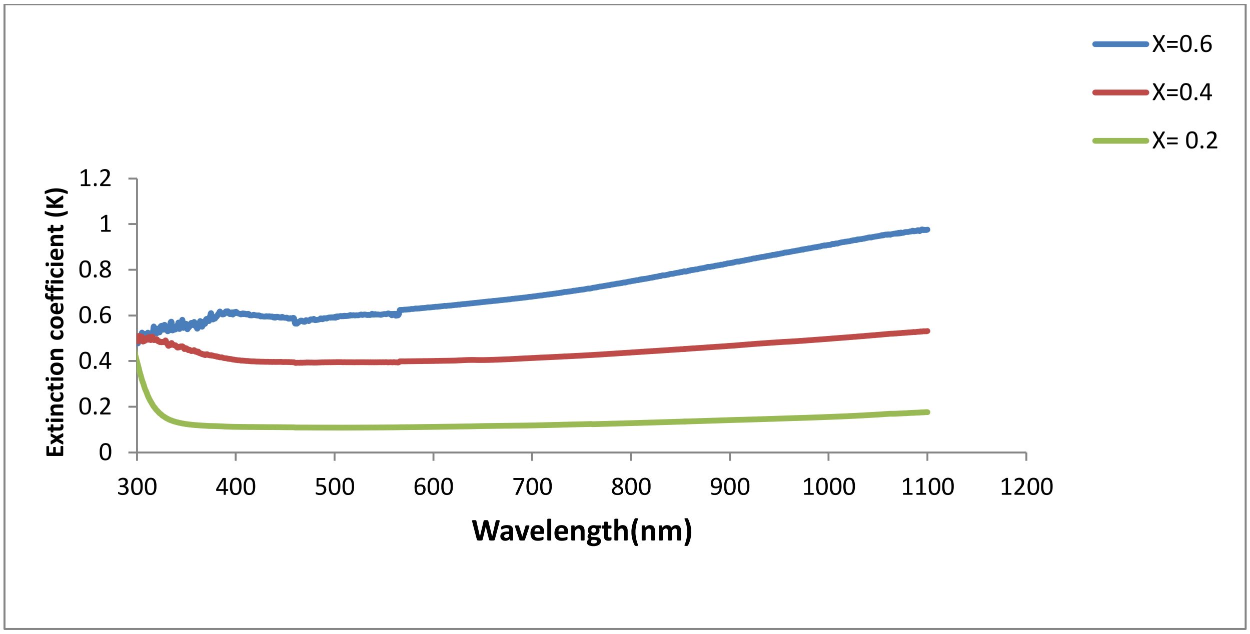

**Figure (4-19): For PbS:Cd thin films with varying doping ratios, the extinction coefficient (k◦) changes with wavelengths.**

The extinction coefficient (K◦) of pure PbS:Cr thin films produced at RT with varied doping ratios ranging (2,4,6 )wt% at a fixed number of pulses (100 pulses) [108], is shown in Figure (4-20). As seen in this graph, the extinction coefficient rises as the doping ratio rises ( 2,4,6)wt%. When compared to the absorption coefficient's behavior, this behavior is similar and correlates to equation (2-12). The extinction coefficient in Table (4-5) is identical to for thin films manufactured of PbS:Cr using a different technique.

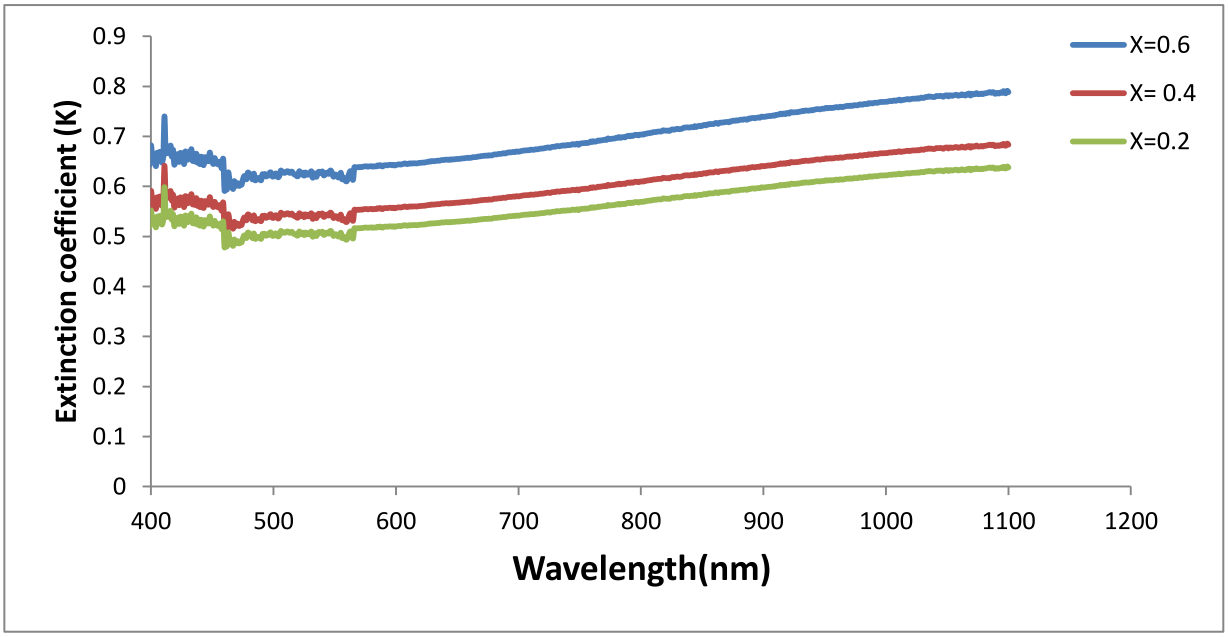

**Figure (4-20): variation of the extinction coefficient (k∘) with wavelength for PbS:Cr thin films at various doping ratios.**

## 4-4-5 Refractive Index

Figure (4-21) shows the variation in refractive index vs wavelength for PbS thin films with different laser energy (200–350) mJ at RT and a set number of pulses (100) As the laser energy is increased from (200 – 350) mJ, the refractive index of all prepared samples increases slightly. This behavior can be explained by improvements in the crystallization of PbS membranes. This finding was found to be in agreement with those of PbS thin films manufactured using a different technique[110].

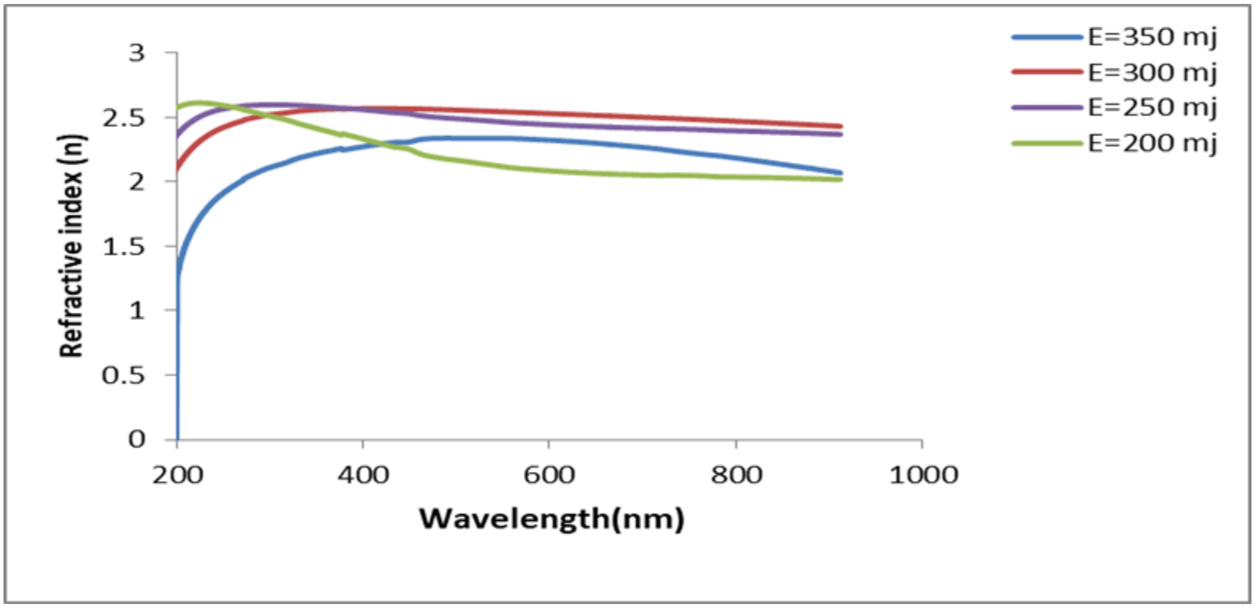

**Figure (4-21): the refractive index versns wavelength for PbS films at different laser energies.**

Figure (4-22) shows the variation in refractive index versus wavelength for PbS:Cd thin films preparedwith various compositions(X=2,4,6)wt% in the region (300-1100) nm. Grafting ratios at RT and a constant number of pulses (1 00 pulses). For all produced samples, this figure indicates that the refractive index increases somewhat as the inoculation ratios increase. The improvement in the crystallization of PbS:Cd thin films can be used to explain this behavior. For PbS:Cd thin films made using a different process, this finding was found to be in agreement with [107].

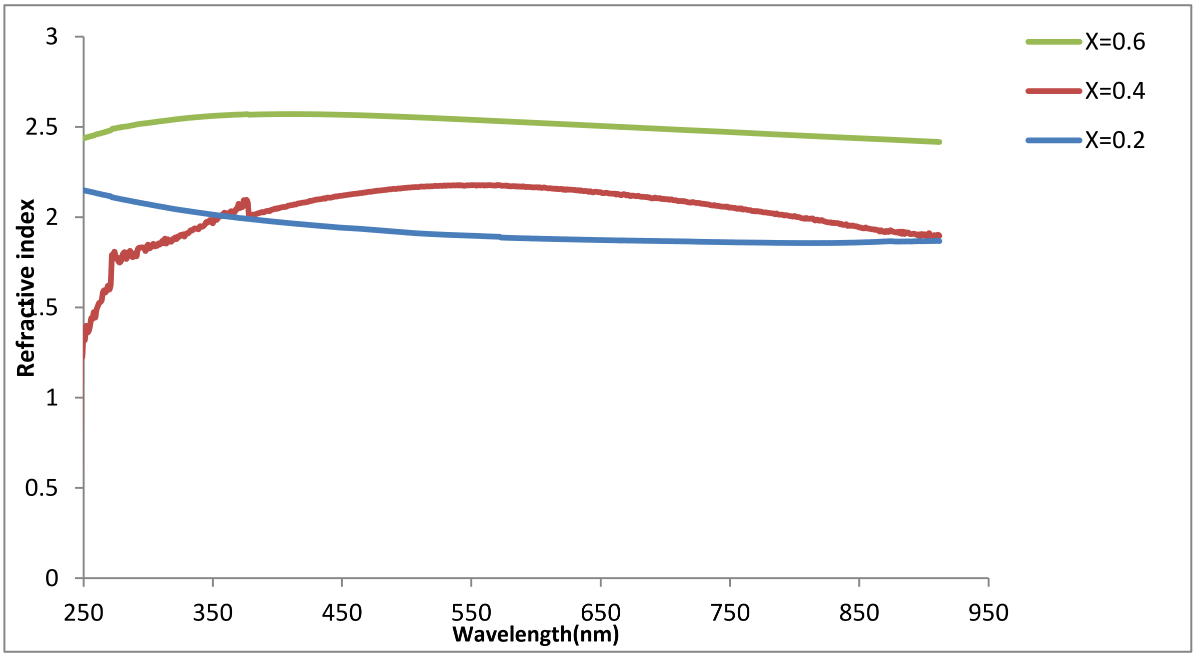

**Figure (4-22): the refractive index versus wavelength for PbS:Cd films at different doping ratio.**

Figure (4-23) shows prepared the variation in refractive index versus wavelength for PbS:Cr thin films with various compositions (X=2,4,6)wt% in the region (300-1100) nm RT grafting ratios and a fixed number of pulses (100 pulses). This figure shows that when the inoculation ratios increase, the refractive index increases slightly for all generated samples. This phenomenon can be explained by improvements in the crystallization of PbS:Cr thin films. This conclusion was found to be in agreement with for PbS:Cr thin films created using a different technique [108].

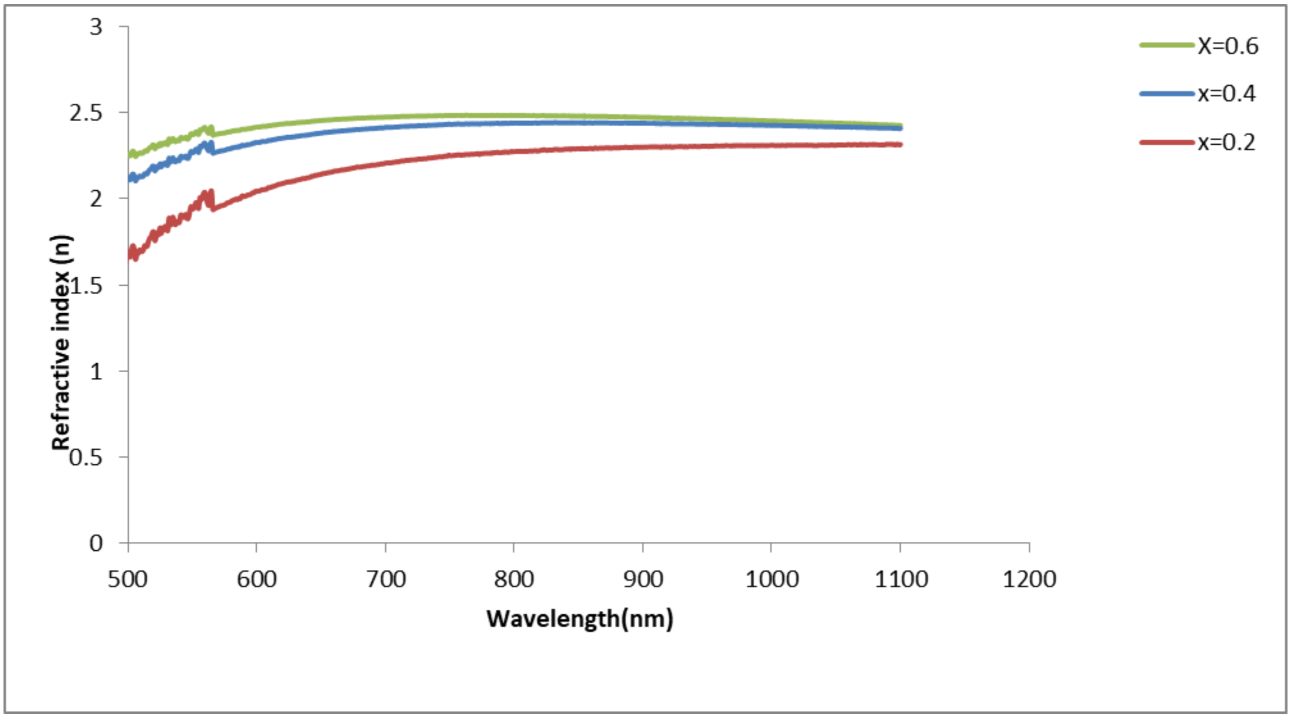

**Figure (4-23): PbS:Cr films were studied doping ratios, the index of refraction varies with wavelength.**

## 4-4-6 The Optical Dielectric Constant ($\varepsilon_r$ and $\varepsilon_i$)

Figures (4-24.a) and (4-24.b) demonstrate the fluctuation of the dielectric constant's real ($\varepsilon_r$) and imaginary ($\varepsilon_i$ ) components vs wavelengths values in the range (300-1100) nm for PbS thin films with different laser energy from (200 – 350) mJ at RT and a fixed number of pulses (100 pulses) .It can be seen that the real part's estimates are higher than the imaginary part's. According to the relationship in equation, the behavior of the real part of the dielectric constant is comparable to that of the refractive index due to the smaller value of ($k_{\circ}^2$) compared to ($n_{\circ}^2$) (2-18). While, as shown in equation, the value of the imaginary part ($\varepsilon_i$) of the dielectric constant is mostly determined by the value of the extinction coefficient ($k_{\circ}$) (2-19).

As can be observed at higher (500 nm) wavelength radiation, $\varepsilon_r$ and $\varepsilon_i$ increase with increasing of laser energy. [110].

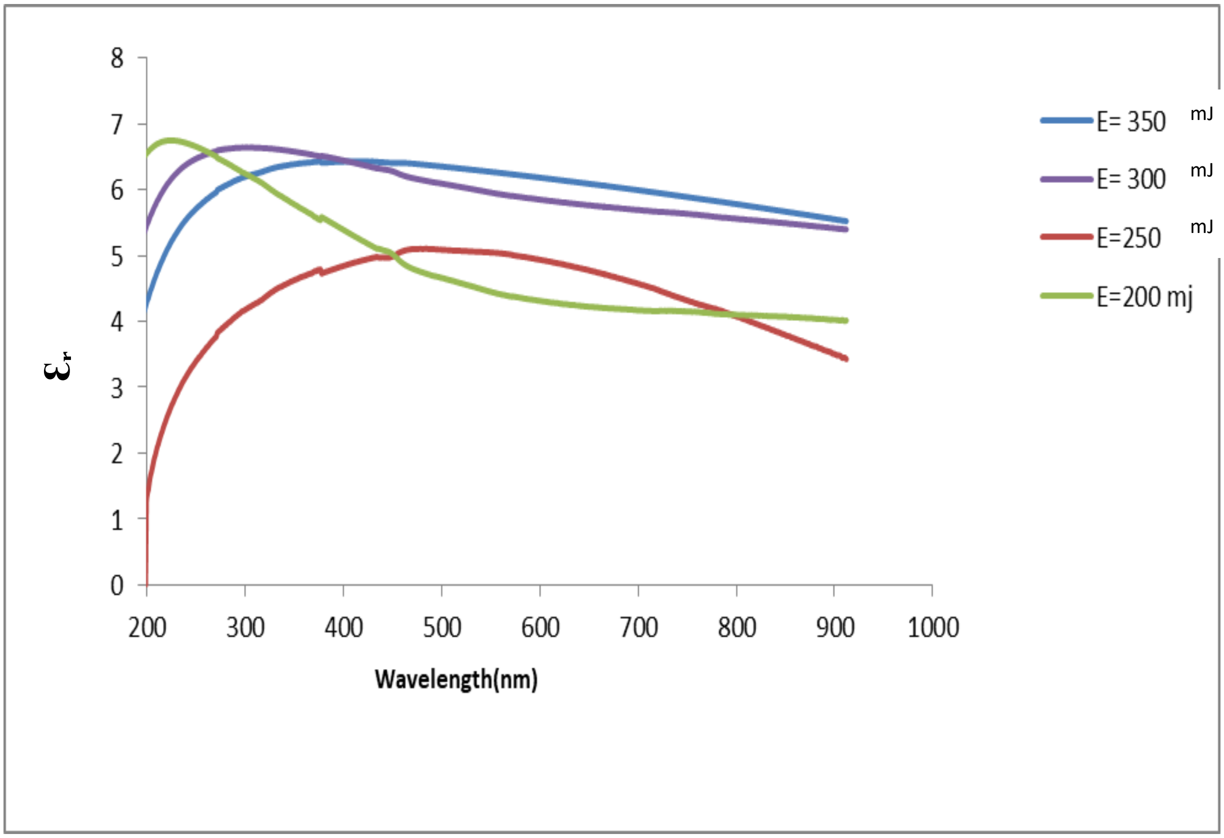

**Figure (4-24.a) : PbS films prepared at various laser energy, the real dielectric constant changes with wavelength.**

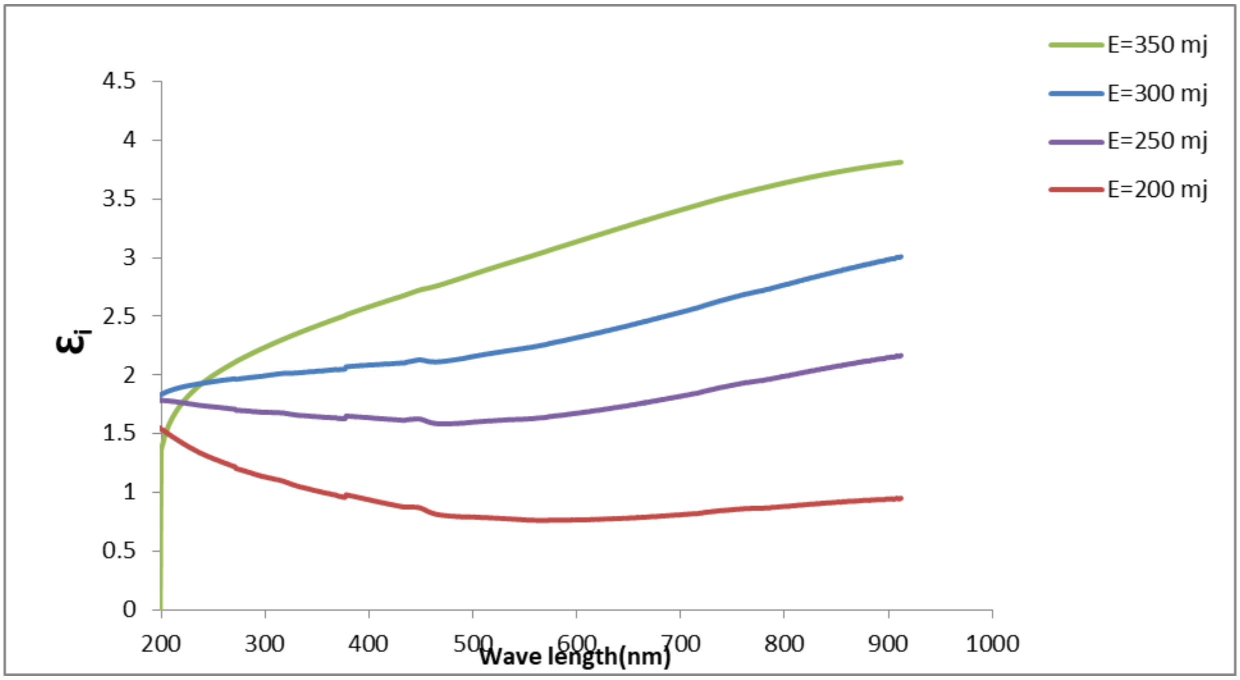

**Figure (4-24.b): variation of imaginary dielectric constant with wavelength for PbS films at different laser energies.**

Figures (4-25.a) and (4-25.b) show the fluctuation of the dielectric constant's real ($\varepsilon_r$) and imaginary ($\varepsilon_i$) portions vs wavelength values in the range (300-1100) nm for PbS:Cd atdifferent doping ratios of thin films (2,4,6)wt% at RT and a fixed number of pulses (100 pulses) . The real part's estimates are higher than the imaginary part's, as can be shown. Because of the smaller value of, the behavior of the real part of the dielectric constant is comparable to that of the refractive index, according to the relationship in equation. ($k_\circ^2$) compared to ($n_\circ^2$) (2-18). While, as shown in equation, the value of the imaginary part ($\varepsilon_i$) of the dielectric constant is mostly determined by the value of the extinction coefficient ($k_\circ$) (2-19). ). As can be observed at higher (500 nm) wavelength radiation, $\varepsilon_r$ and $\varepsilon_i$ increase with increasing doping ratios [107].

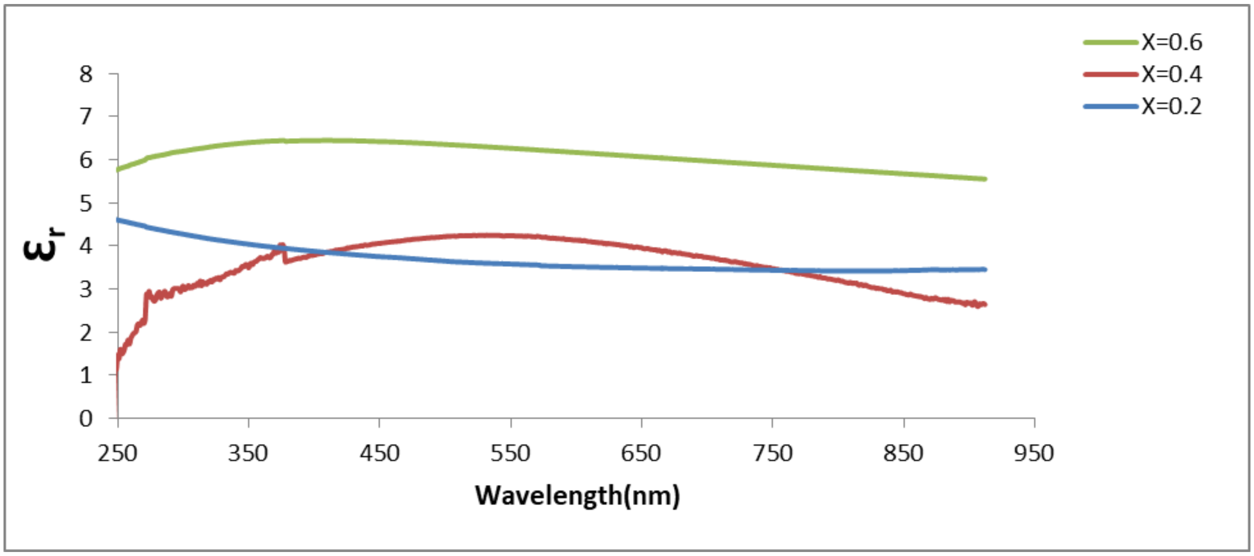

**Figure (4-25.a): variation of real dielectric constant with wavelength for PbS:Cd films at different doping ratios.**

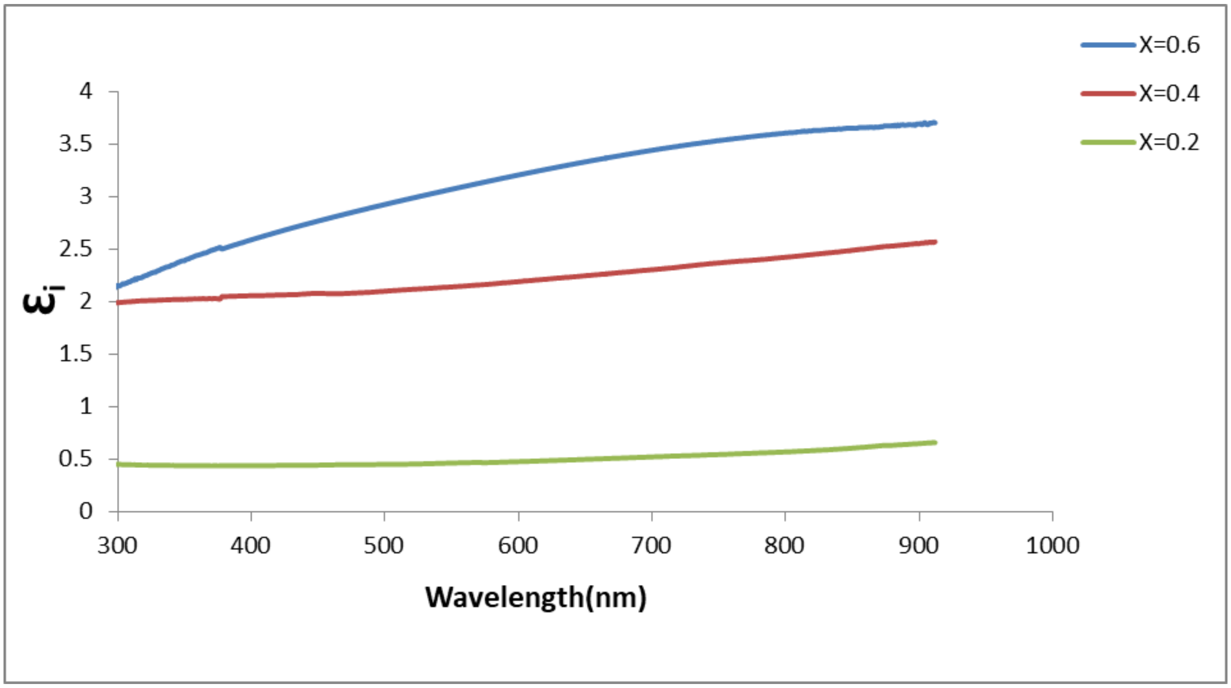

**Figure (4-25.b): shows different of imaginary dielectric constant with wavelength for PbS:Cd films at different doping ratios.**

Figures (4-26.a) and (4-26.b) show the change of a dielectric constant's real ($\varepsilon_r$) and imaginary ($\varepsilon_i$) parts versus wavelength values ranging (300-1100) nm for PbS:Cr thin films with different doping ratios (2,4,6)wt% at RT and a fixed number of pulses (100 pulses) . The estimates of the real part are higher than those of the imaginary part, as can be observed. Because the real part of the dielectric constant has a smaller value than the refractive index, its behavior is comparable to that of the refractive index, according to the relationship in equation. ($k_\circ^2$) compared to ($n_\circ^2$) (2-18). While, as shown in equation, the value of the imaginary part ($\varepsilon_i$) of the dielectric constant is mostly determined by the value of the extinction coefficient ($k_\circ$) (2-19). As can be observed at higher (500 nm) wavelength radiation, $\varepsilon_r$ and $\varepsilon_i$ increuse with increasing of doping ratios [108].

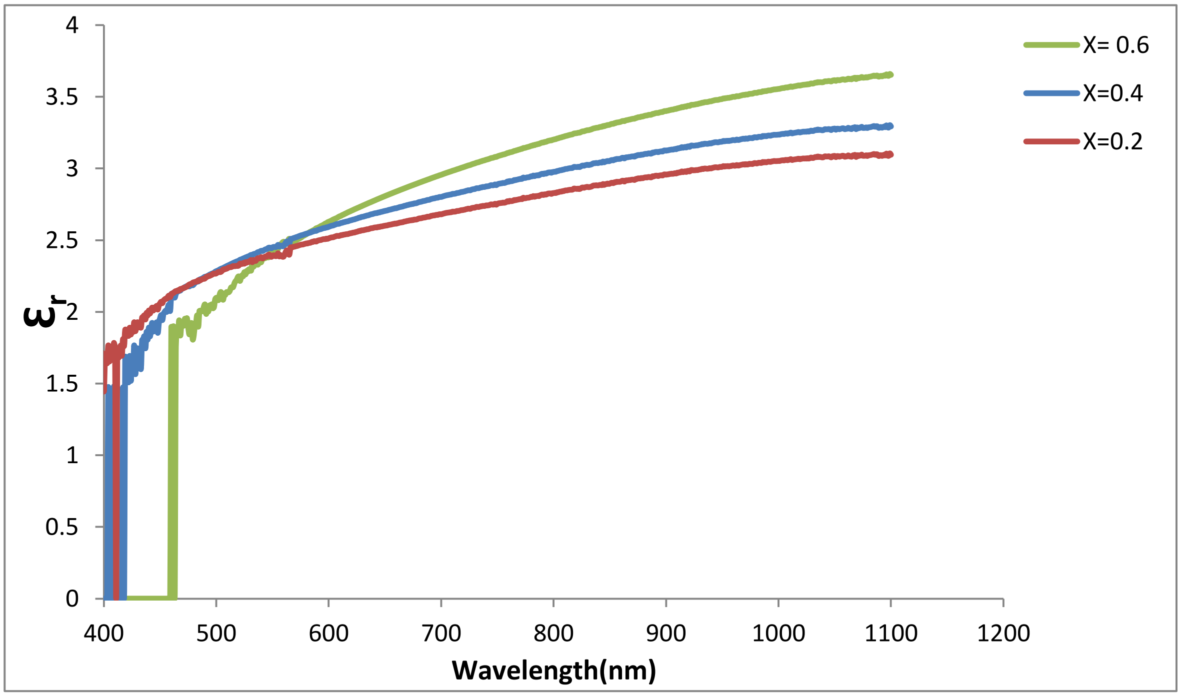

**Figure (4-26.a): variation of real dielectric constant with wavelength for PbS:Cr films at different doping ratios.**

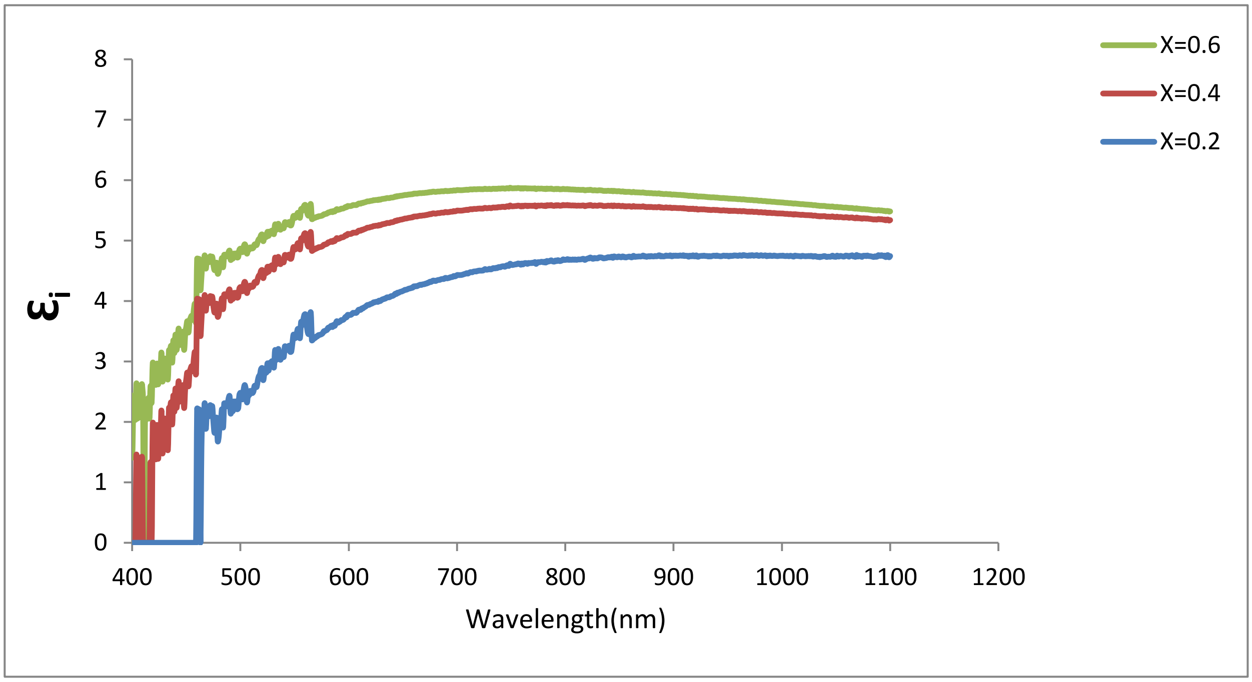

**Figure (4-26.b): variation of imaginary dielectric constant with wavelength for pbs:Cr films at different doping ratios**.

**Table (4-5) The obtained results of optical properties at wavelength 550 nm of PbS, PbS:Cd and PbS:Cr thin films at different laser energies and different doping ratios .**

| Material | A% | α ($cm^{-1}$) | $K_{\circ}$ | N | $\varepsilon_r$ | $\varepsilon_i$ | $E_g$ (eV) |
|---|---|---|---|---|---|---|---|
| **PbS E=200 mJ** | 20.53 | 47280 | 0.2070 | 2.2359 | 4.6971 | 0.9903 | 0.26 |
| **E=250 mJ** | 31.51 | 72613 | 0.3179 | 2.3916 | 5.6771 | 1.6399 | 0.30 |
| **E=300mJ** | 34.50 | 91037 | 0.3986 | 2.5622 | 6.4033 | 2.0429 | 0.32 |
| **E=350mJ** | 54.52 | 125582 | 0.5499 | 2.5788 | 6.5491 | 2.4592 | 0.34 |
| **PbS:Cd X=2%** | 10.86 | 25023 | 0.1095 | 2.002 | 3.7146 | 0.4389 | 1.5 |
| **X=4%** | 60.10 | 138422 | 0.3949 | 2.020 | 3.9996 | 2.0264 | 2.1 |
| **X=6%** | 84.15 | 190183 | 0.6061 | 2.565 | 6.4266 | 2.4493 | 2.7 |
| **PbS:Cr X=2%** | 49.97 | 115084 | 0.5039 | 1.9430 | 3.3874 | 2.3917 | 1.6 |
| **X=4%** | 53.54 | 123304 | 0.5399 | 2.2685 | 4.8546 | 2.4211 | 1.7 |
| **X=6%** | 61.77 | 142274 | 0.6230 | 2.3730 | 5.3772 | 2.4497 | 1.8 |

## 4-5 Hall Effect

The type of charge and concentration of carriers ($n_H$) as well as their Hall mobility ($\mu_H$) as determined by hall measurements. The influence of the main hall shown in Table (4-6). The $R_H$ Hall coefficient was calculated using equation (2-20). The PbS and PbS:Cd samples are n-type, whereas the PbS:Cr sample is p-type, according to a positive $R_H$ sign. Values for carrier concentration ($n_H$) and Hall mobility ($\mu_H$) Equations are determined using Equations (2-21) , (2-22) and (2-25).When the Cd and Cr content is raised, the concentration of carriers increases and the hall mobility falls. In addition to the charge carriers produced by doping, a rise in the density of charge carriers occurred. The negative connection between $\mu_H$ and $n_H$ causes mobility to diminish.

**Table (4-6) Hall effect measurements for PbS, PbS:Cd and PbS:Cr thin films with different energy and doping ratios.**

| Sample | Laser energy and doping ratios | $R_H$ ($cm^{-3}C^{-1}$) | n ($cm^{-3}$) | ợ $(o.cm)^{-1}$ | μ ($cm^2V^{-1}s^{-1}$) | Conductivity Type |
|---|---|---|---|---|---|---|
| **PbS** | 350 Mj | 9.61E+04 | 6.49E+13 | 1.73E+00 | 1.66E+05 | n |
| **PbS:Cd** | X=6% | 4.76E+02 | 1.31E+16 | 1.10E+02 | 5.23E+04 | n |
| **PbS:Cr** | X=6% | 1.47E+05 | 4.24E+13 | 3.91E+00 | 5.74E+05 | p |

# 4-6 Gas Sensor Measurements

## 4-6-1 Gas Sensing measurements of (PbS, PbS:Cd and PbS:Cr)/Si toward reducing gas ($NH_3$)

Figures (4-27 to 4-36) show the variation of resistance as a function of time. As low gas sensors at different working temperatures of the PbS,PbS:Cd/p-Si and PbS:Cr/n-Si. Resistance fluctuation as a function of time when $NH_3$ gas was introduced at 5% concentration and heated at various working temperatures, (473, 523, and 573) K. Table (4-7) shows the estimated sensitivity. The shape of the response plot versus time of the sensing cell, which is evident from the shape of the response plot versus time of the PbS, PbS:Cd/p-Si and PbS:Cr/n-Si sensing cell when exposed to $NH_3$ gas, is well known to depend on the surface shape and degree of crystallization as well as the chemical composition. For all working temperatures under exposure to $NH_3$ gas, the resistance increases. While the resistance return to decreases when the exposure to $NH_3$ is stopped and let to air admittance [112].

Because $NH_3$ is a reducing gas, this the behavior demonstrates the p-type sensor's nature as a result of PbS, PbS:Cd/p-Si and PbS:Cr/n-Si semiconductor nature. While all other sensor cells' resistance falls when exposed to $NH_3$ gas at all operating temperatures, when $NH_3$ is discontinued and air is added, the resistance returns to its original value. This behavior demonstrates the n-type sensor's nature, which is caused by PbS:Cr n-type semiconductor nature, which is the only component of the of PbS, PbS:Cd/p-Si –loaded[113] . PbS:Cr gas sensor of PbS, PbS:Cd/p-Si sensor has excellent reversibility; when air is reintroduced, the exit signal reverts to the air value. The sensitivity of the x-content sensor cell was shown to decrease with increasing working temperature, while the sensitivity of the high x-content sensor cell increased with increasing operating temperature. The maximum sensitivity (19%) of the PbS /P-Si composite sensors is observed when the relative high working temperature is 523 K. The maximum sensitivity (15%) of the composite sensors PbS:Cr/n-Si is at 573 K. Activation of $NH_3$ uptake is not sufficient. At higher temperatures (i.e. 573 K), the gas adsorption rate is much higher than the adsorption rate, which means that the gas escapes before effective adsorption on the sensor surface [111]. The sensing method can be improved in the following way: The resistance of a metal-based gas sensor changes as it is exposed to a target gas. The composition and this shift can be used to identify the target gas's level. Adsorption of oxygen gas in the air on to the sensor surface when the PbS, PbS:Cd/p-Si and PbS:Cr/n-Si sensors are in an aerobic environment [114-115].

$O_2(g) \rightarrow O_2(ads)$

$O_2(ads) + e^{-} \rightarrow O^{2\,-}$ (ads) $O_2^{\,-} + e^{-} \rightarrow 2O^{-}$ (ads)

$O^{-} + e^{-} \rightarrow O^{2-}$

When the sensor is exposed to an $NH_3$ atmosphere, hydrogen molecules interact with oxygen ions adsorbed on the sensor's surface according to the equation below.

$2NH_3 + 3O^{-}(ads) \rightarrow N2 + 3H_2O + 3e-$

The released electrons return to the sensor's surface as a result of the previous events, resulting in a dramatic reduction in the breadth of the electron depletion layer on the sensor. As a result, may be seen. Furthermore, due to the abundance of PbS:Cr substantial n- PbS:Cr-n- PbS:Cr symmetries exist, which can act as potential barriers to electron passage. The resistance varies when the potential height of homodimers is changed in the presence of $NH_3$, which adds to the emergence of the sensor signal. It should be noted, that because the manufactured sensors contain extremely small amounts of PbS, PbS:Cd/p-Si homogenous are unlikely to have a major impact on the sensors' final sensing capability. Furthermore, because hydrogen has a strong reducing impact, PbS:Cr surface mining is based on the adsorption of $NH_3$ atoms. The resistance of PbS:Cr surfaces changes as a result of the surface metal, which adds to the sensor response. When removing the $NH_3$ gas as well as the air supply. It should be noted that all the manufactured sensors were roasted at the same temperature, which means that all sensors are assumed to have approximately the same shape, surface area, and grain sizes. Therefore, excluded these factors in our analysis. It was found that the sensing is greatly affected by the number of p- PbS / n- PbS:Cr variance with different doping ratios, the response can be improved by increasing cadmium and chromium doping ratios as well as increasing the laser energy during model making.[113]. As a result, the gas sensor's resistance changes more. However, the response reduced for the remaining formulations. This could be owing to p-type PbS , PbS:Cd weak gas sensing properties compared to n-type PbS:Cr, and (ii) a potential decrease in heterogeneous PbS, PbS:Cd and PbS:Cr due to higher congeners, rather than direct contact with the gas. PbS, PbS:Cd/p-Si and PbS:Cr/n-Si granules made direct contact with each other, causing the sensor response to degrade. At E=250 mJ, the highest reaction (19%) was recorded. These findings are linked to the large grain size, which causes the active surface area to expand, resulting in the formation of high adsorption sites that could potentially interact with the gas. The drop in grain size, which leads to a reduction in accessible adsorption sites, explains the decrease in sensitivity. Table (4-7) shows the calculated sensitivity. Sensing performance is frequently linked to material crystallization. The intrinsic resistance of the material reduces as crystallization progresses, resulting in improved electron transport and high sensing performance, as evidenced by the high sensitivity of the PbS sample at temperature 523K. Due to the large size of the grains, which led to the enlarging of the active area. Resulting in the improvement of the inner grains for the reaction with $NH_3$ gas. The second sample PbS:Cr at temperature 573 K containing chromium content X = 6% sensitivity(15%) due to the large size of the grains, which led to the enlarging of the active area, resulting in the improvement of the inner grains for the reaction with $NH_3$ gas.

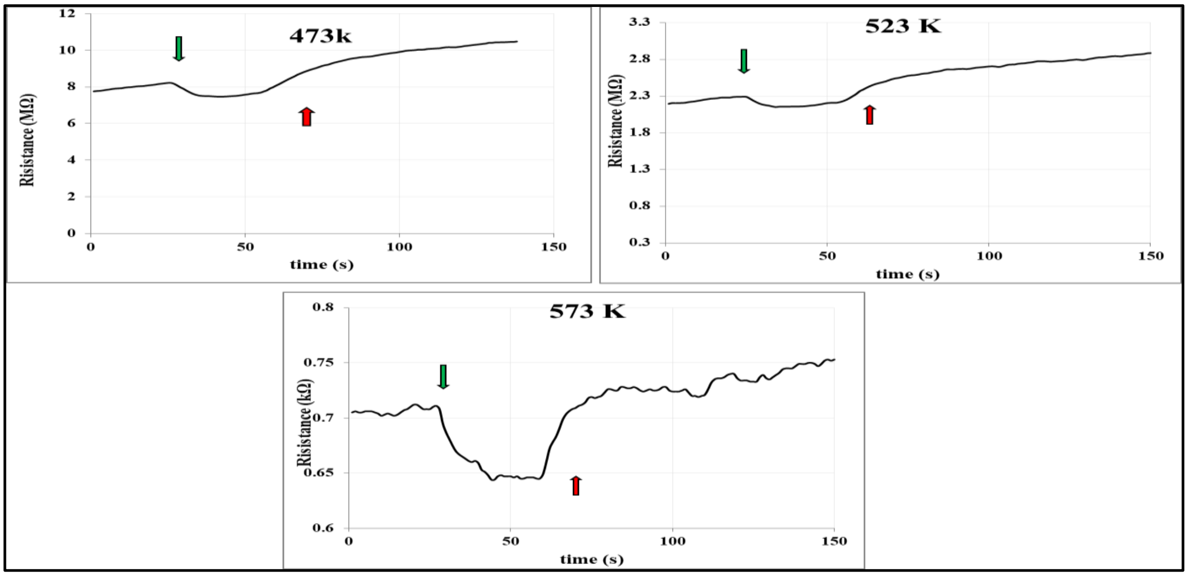

**Figure (4-27): Sample resistance change of PbS at laser energy (200 mJ) upon opening and closing of $NH_3$ gas at (473,523,573)K**

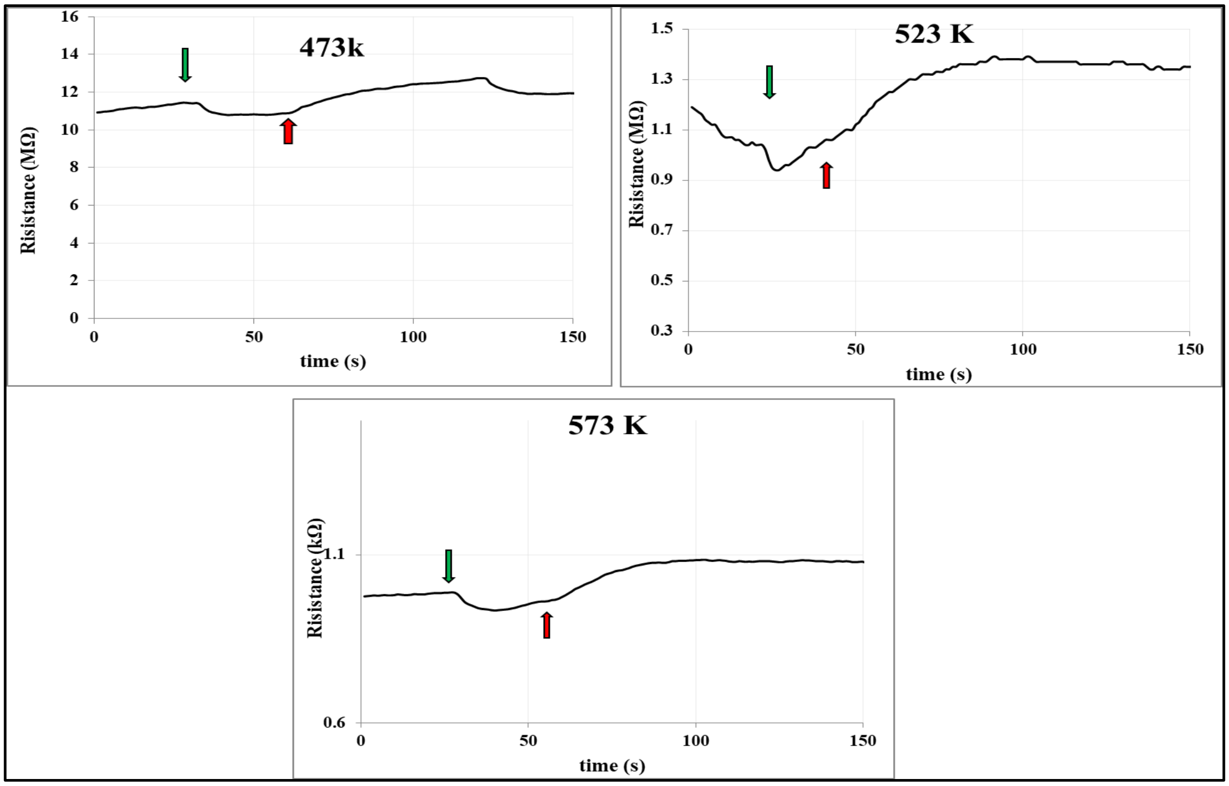

**Figure (4-28): Sample resistance change of PbS at laser energy (250 mJ) upon opening and closing of $NH_3$ gas at (473,523,573)K**

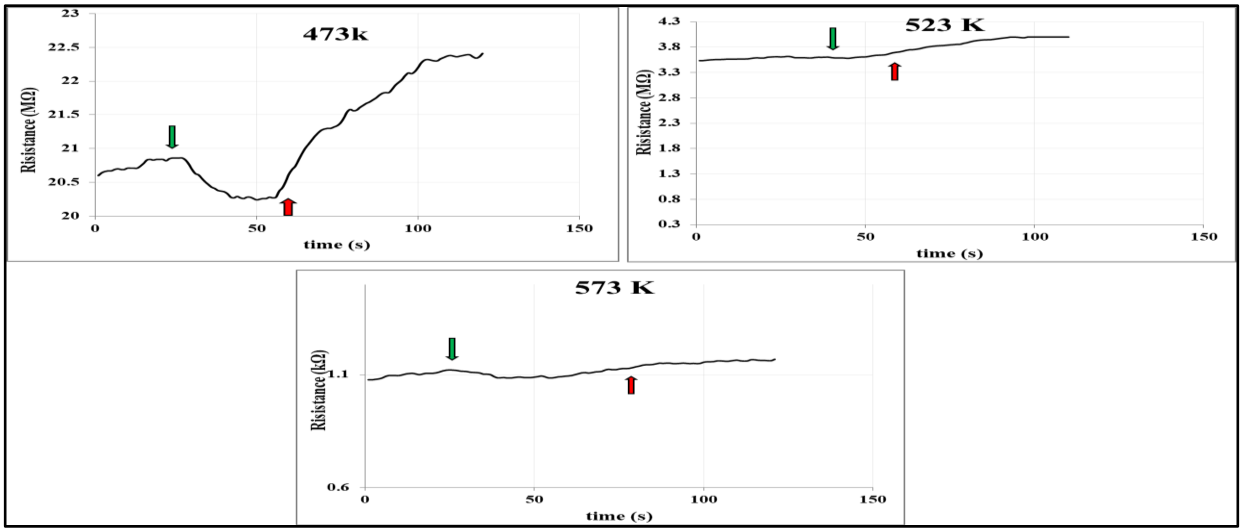

**Figure (4-29): Sample resistance change of PbS at laser energy (300 mJ) upon opening and closing of $NH_3$ gas at (473,523,573)K**

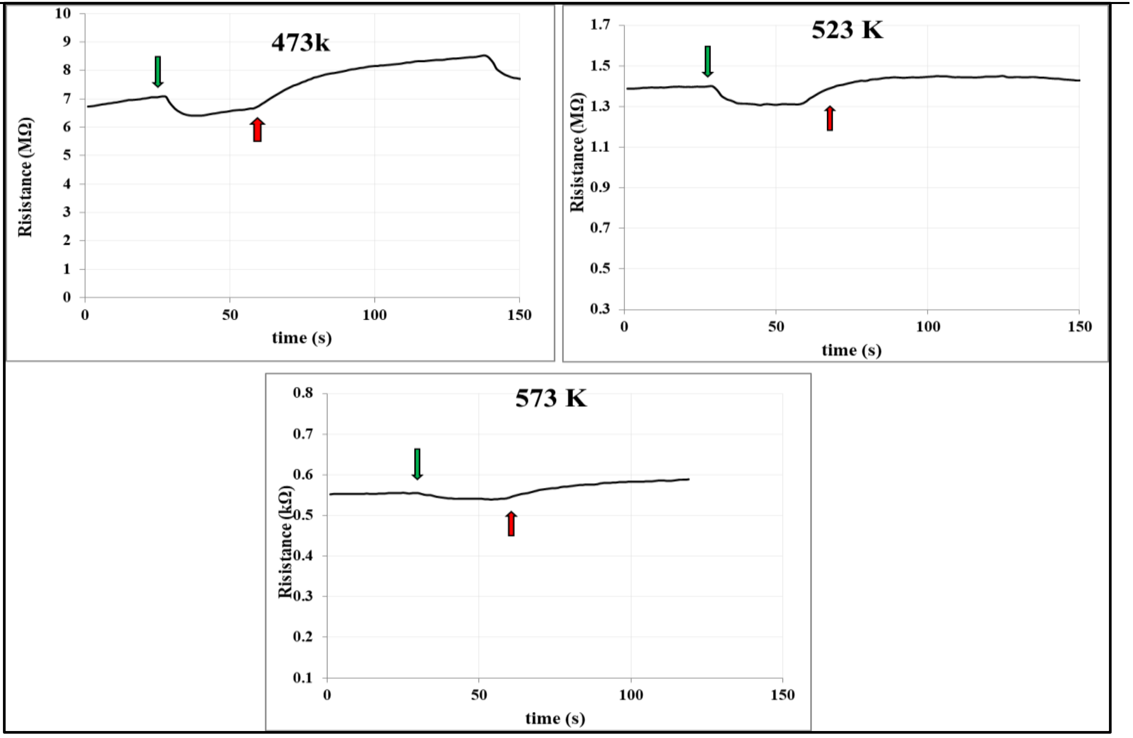

Figure (4-30): Sample resistance change of PbS at laser energy (350 mJ) upon opening and closing of $NH_3$ gas at (473,523,573)K

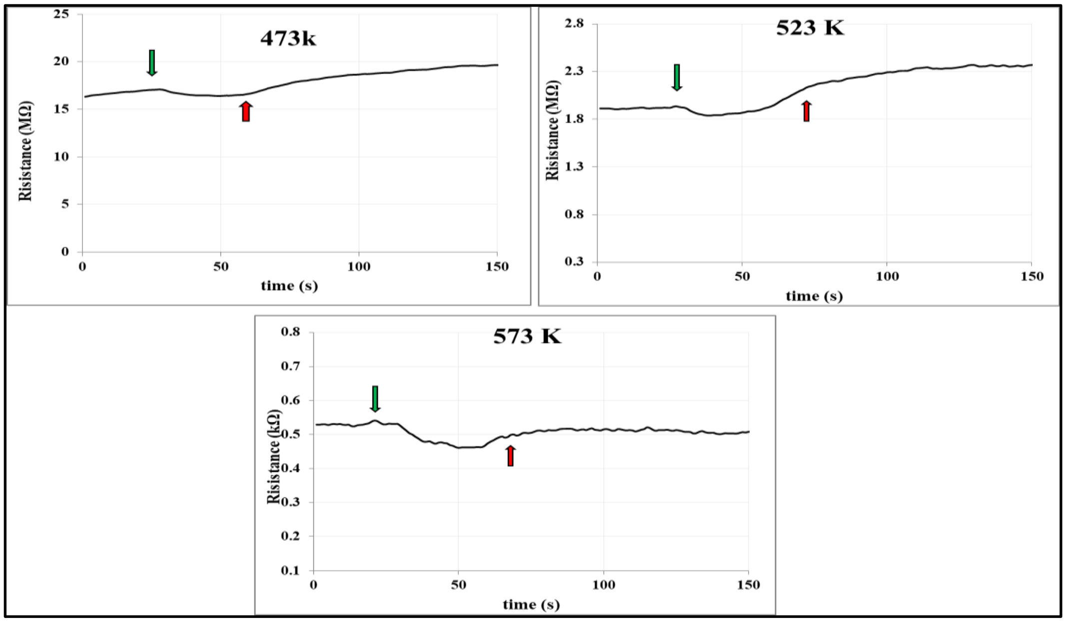

Figure (4-31): Sample resistance change of PbS:Cd at doping ratio(X=2%) upon opening and closing of $NH_3$ gas at (473,523,573)K

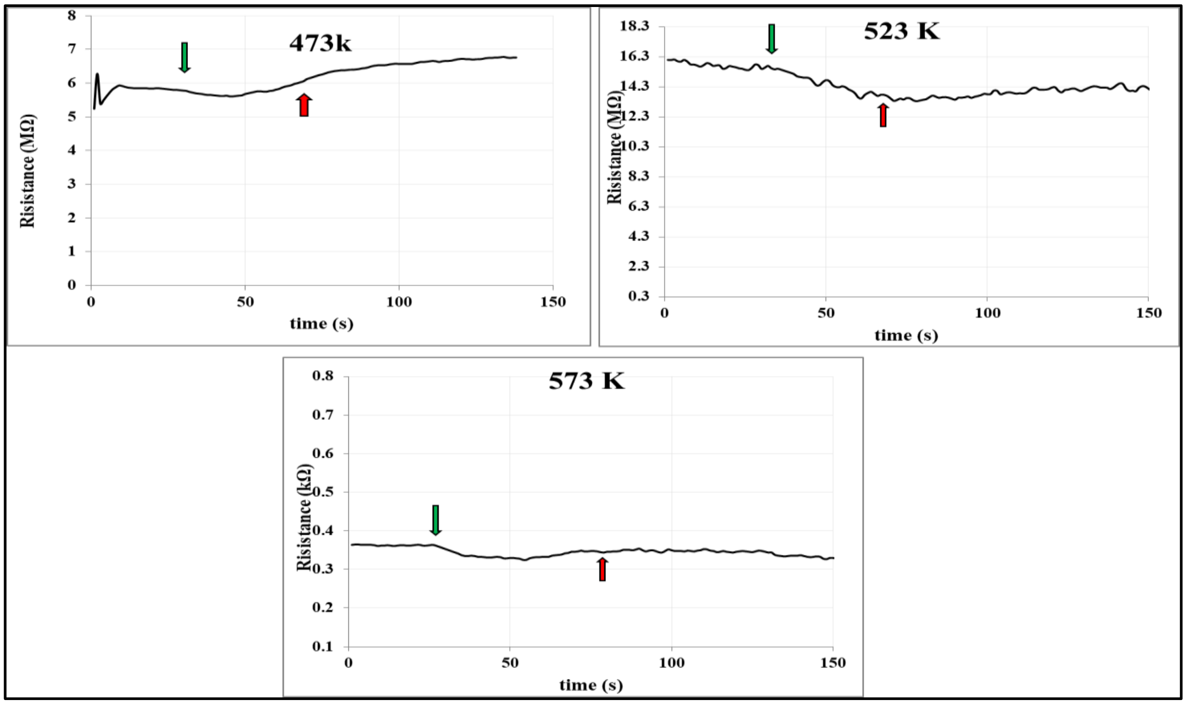

**Figure (4-32): Sample resistance change of PbS:Cd at doping ratio(X=4%) upon opening and closing of $NH_3$ gas at (473,523,573)K**

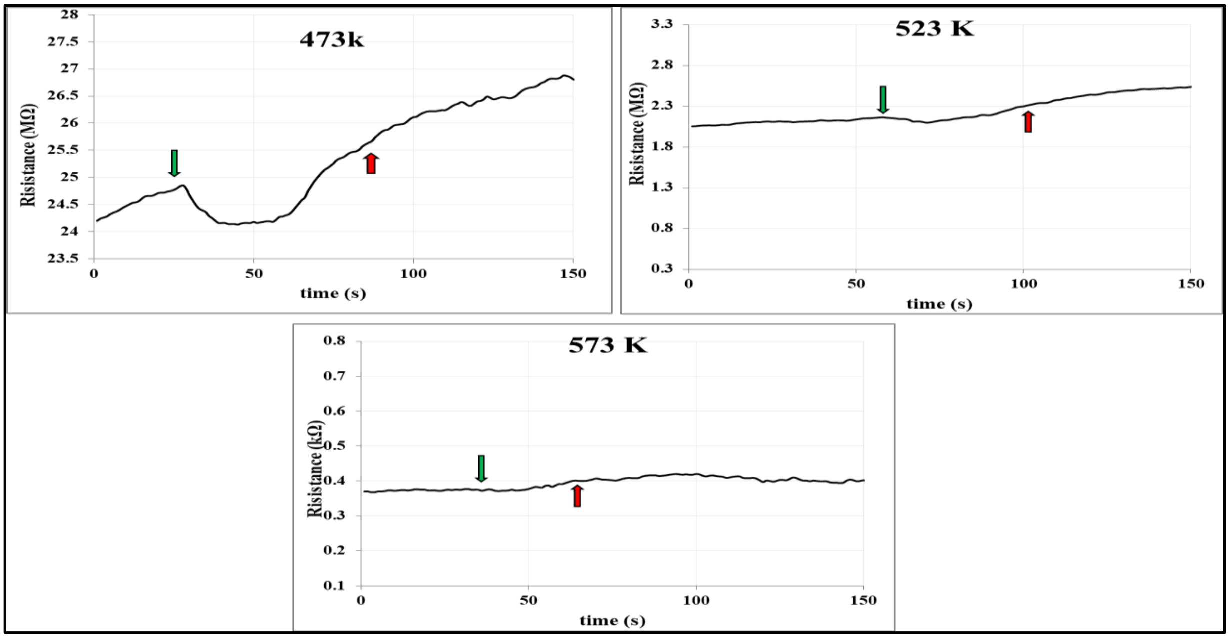

**Figure (4-33): Sample resistance change of PbS:Cd at doping ratio(X=6%) upon opening and closing of $NH_3$ gas at (473,523,573)K**

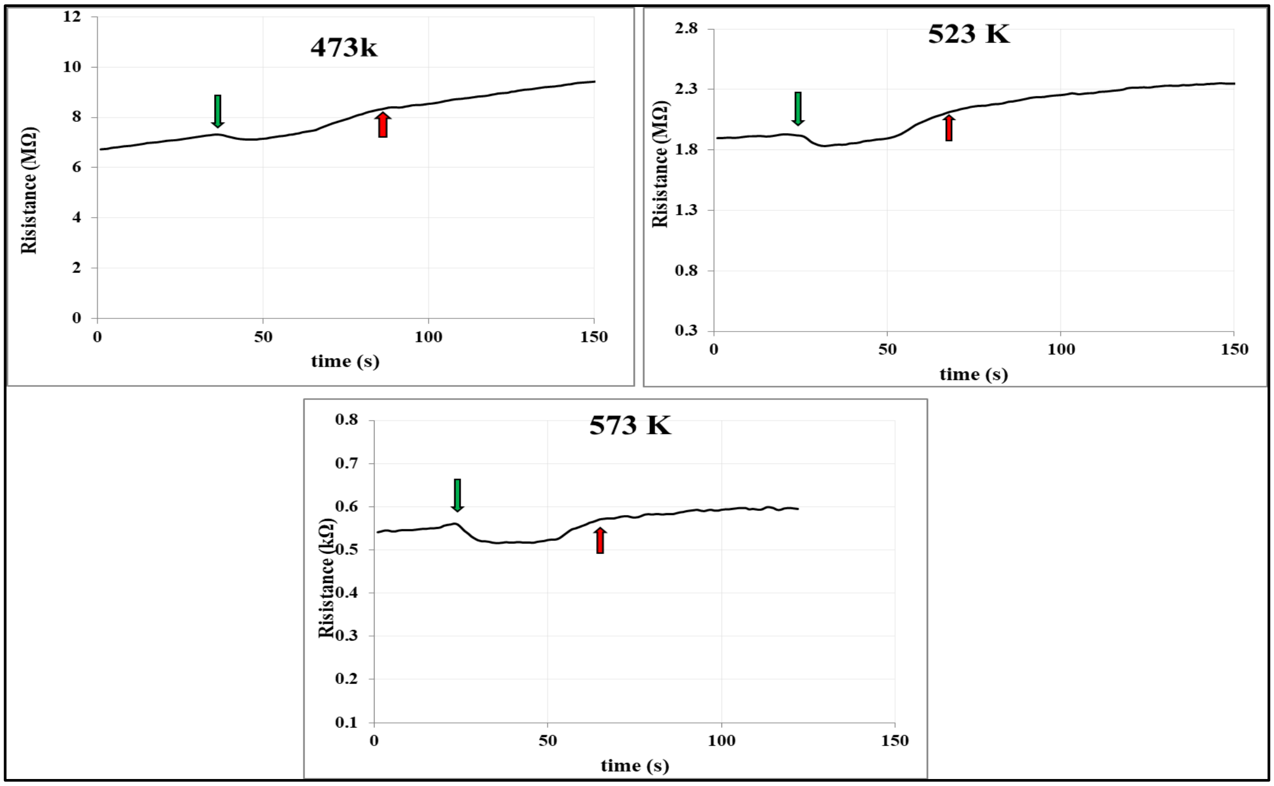

**Figure (4-34): Sample resistance change of PbS:Cr at doping ratio(X=2%) upon opening and closing of $NH_3$ gas at (473,523,573)K**

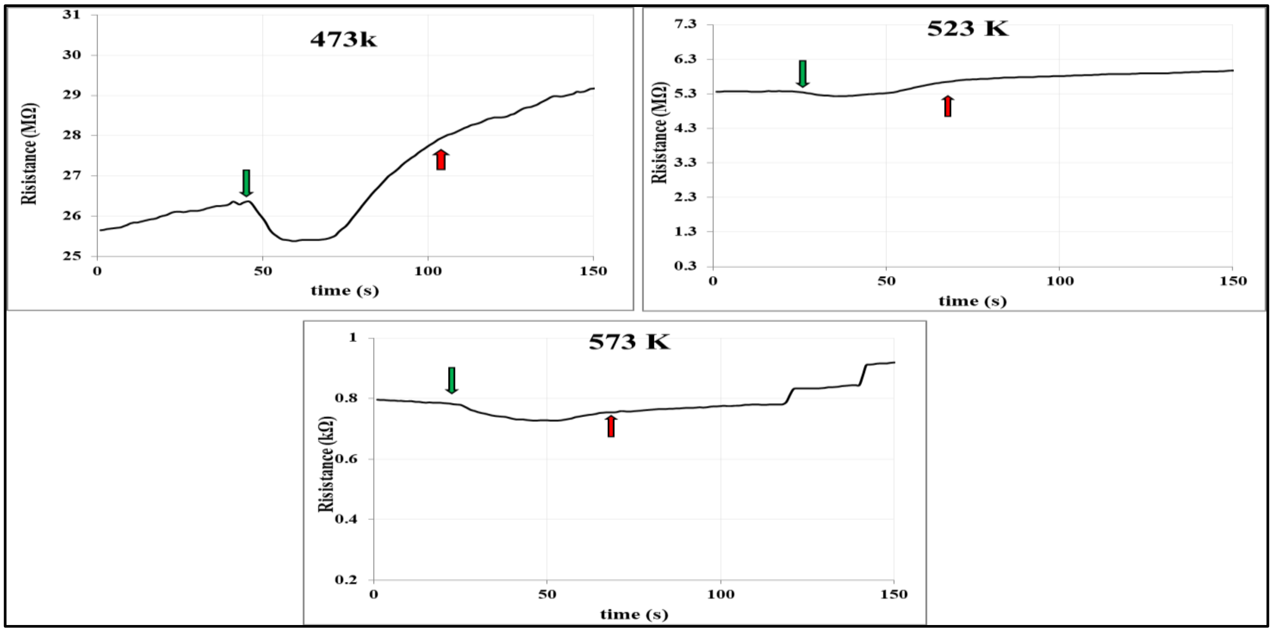

**Figure (4-35): Sample resistance change of PbS:Cr at doping ratio(X=4%) upon opening and closing of $NH_3$ gas at (473,523,573)K**

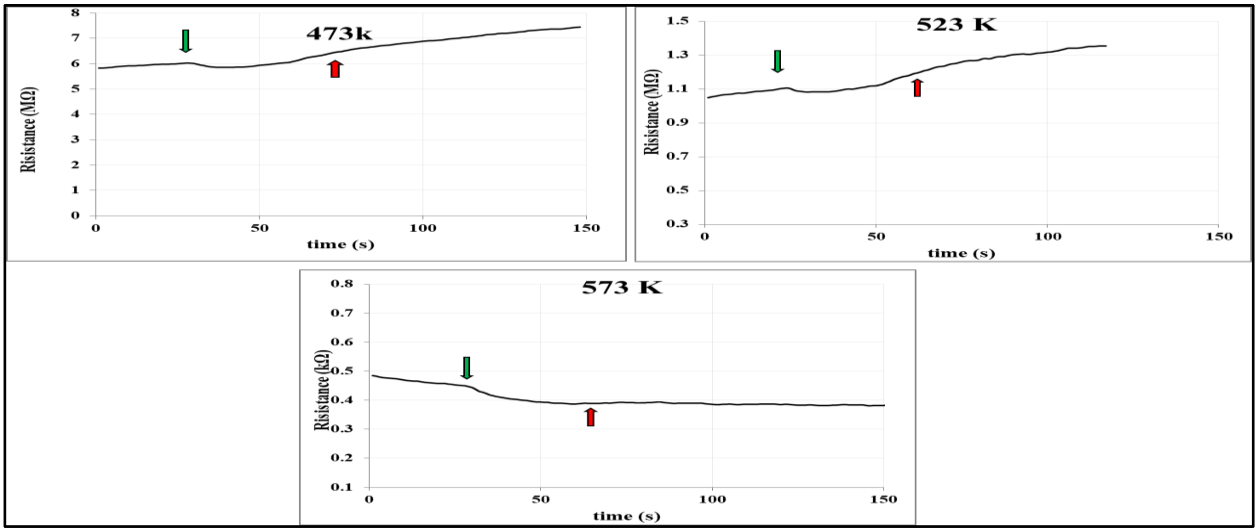

**Figure (4-36): Sample resistance change of PbS:Cr at doping ratio(X=6%) upon opening and closing of $NH_3$ gas at (473,523,573)K**

**Table (4-7) The sensing measurements data for PbS, PbS:Cd/p-Si and PbS:Cr/n-Si as reducing gas sensors($NH_3$).**

| Sample | Temp (K) | Sensitivity % | Response time (s) | Recovery time (s) |
|---|---|---|---|---|
| Pbs<br>E= 200 mJ | 473 | 9.504 | 16.2 | 53.1 |
| | 523 | 5.754 | 15.3 | 56.7 |
| | 573 | 9.737 | 21.6 | 48.6 |
| E= 250 mJ | 473 | 5.180 | 18 | 58.5 |
| | 523 | 19.008 | 28.8 | 39.6 |
| | 573 | 5.454 | 14.4 | 54.9 |
| E= 300 mJ | 473 | 2.662 | 22.5 | 47.7 |
| | 523 | 0.557 | 18 | 34.2 |
| | 573 | 2.846 | 18.9 | 31.5 |
| E= 350 mJ | 473 | 9.657 | 12.6 | 57.6 |
| | 523 | 6.483 | 18.9 | 51.3 |
| | 573 | 2.772 | 18.9 | 30.6 |
| Pbs:Cd<br>X= 2% | 473 | 3.593 | 22.5 | 64.8 |
| | 523 | 4.288 | 16.2 | 53.1 |
| | 573 | 14.470 | 21.6 | 45.9 |
| X= 4% | 473 | 3.730 | 18.9 | 53.1 |
| | 523 | 10.984 | 27.9 | 55.8 |
| | 573 | 10.334 | 20.7 | 33.3 |
| X=6% | 473 | 2.652 | 18 | 49.5 |
| | 523 | 11.644 | 54.9 | 71.1 |
| | 573 | 10.120 | 36.9 | 49.5 |
| Pbs:Cr<br>X= 2% | 473 | 1.404 | 14.4 | 48.6 |
| | 523 | 4.730 | 12.6 | 59.4 |
| | 573 | 8.510 | 12.6 | 38.7 |
| X= 4% | 473 | 3.346 | 19.8 | 55.8 |
| | 523 | 2.285 | 10.8 | 61.2 |
| | 573 | 7.427 | 21.6 | 47.7 |
| X=6% | 473 | 2.218 | 13.5 | 54.9 |
| | 523 | 1.566 | 13.5 | 38.7 |
| | 573 | 15.856 | 25.2 | 42.3 |

## 4-6-2 Gas Sensing measurements of (PbS, PbS:Cd and PbS:Cr)/Si toward oxidizing gas ($NO_2$)

Figures (4-37 to 4-46) show the variation of resistance as a function of time. As low gas sensors at different working temperatures of the PbS, PbS:Cd/p-Si and PbS:Cr/n-Si. Resistance fluctuation as a function of time when $NO_2$ gas was introduced at 5% concentration and heated at various working temperatures, (473, 523, and 573) K. Table (4-8) shows the estimated sensitivity. The shape of the response plot versus time of the sensing cell, which is evident from the shape of the response plot versus time of the PbS, PbS:Cd/p-Si and PbS:Cr/n-Si sensing cell when exposed to $NO_2$ gas, is well known to depend on the surface shape and degree of crystallization as well as the chemical composition. For all working temperatures under exposure to $NO_2$ gas, the resistance increases. While the resistance return to decreases when the exposure to $NO_2$ is stopped and let to air admittance [112]. Because $NO_2$ is an oxidizing gas, this behavior demonstrates the p-type sensor's nature as a result of PbS, PbS:Cd/p-Si semiconductor nature. Under NO2 gas exposure, the resistance increases, whereas all other sensor cells behave for all operating temperatures. The resistance lowers and returns to its original value when nitrogen dioxide is removed and air is supplied. This behavior demonstrates the n-type sensor's nature, which is due to PbS:Cr/n-Si n-type semiconductor nature; the PbS:Cr/n-Si sensor's reversibility is good. When air is reintroduced, the exit signal tries to restore to the air value. The sensitivity of the sensor cell with the content of high (x) was found to grow with the operating temperature of the sensor cell, but the sensitivity of the sensor cell with the higher content (x) content was found to increase but randomly. At a temperature of 523 K, when the absorbance becomes the absorption of $NO_2$, the maximum sensitivity (137 %) of the (Cd) X=4% at 523K° cell composite sensors is seen [111], which is close to what has been published globally. High operating temperature was discovered to minimize the sensor's initial resistance.

The reason for this is that as the temperature rises, more electrons in the valence band escape PbS:Cr/n-Si and enter the conduction band, increasing the conductivity. Table (4-8) shows the response and recovery times of the gas sensor in the presence of $NO_2$ at various temperatures. It is obvious that adding cadmium and chromium to the host material speeds up the response time, especially at higher levels. Temperatures at work due to the crystal structure of the gas sensor cell. The gas sensor cell has relatively quick dynamic times. This shape allows for rapid mass transfer of $NO_2$ molecules to and from the inside of the sensor, as well as increased charge carrier mobility[113]. The sensor mechanism is based on the chemical adsorption of $NO_2$ gas according to the following reaction. As the temperature rises, the response and recovery times decrease due to quicker gas diffusion [116].

$$NO_2 \text{ gas} + e^- \rightarrow NO_2^-$$

Electrons are removed from the sample's surface area, increasing the sample's resistance. The $NO_2$ ion is subsequently split into NO and O gases using the process below.

$$NO_2 \rightarrow NO \text{ gas} + O^-$$

Due to differences in charge carrier density, there is a variation in gas sensitivity between samples. Extreme sensitivity when exposed to high quantities. The difference in particle size and the roughness of the surface are other factors. The depletion regions in n-type metal oxide semiconductors are smaller than the grain size, and the change in depletion region thickness due to adsorbed gases causes a change in the amount of Schottky barrier between adjacent grains, allowing electron junctions to form while preventing them from unraveling the gas [117].

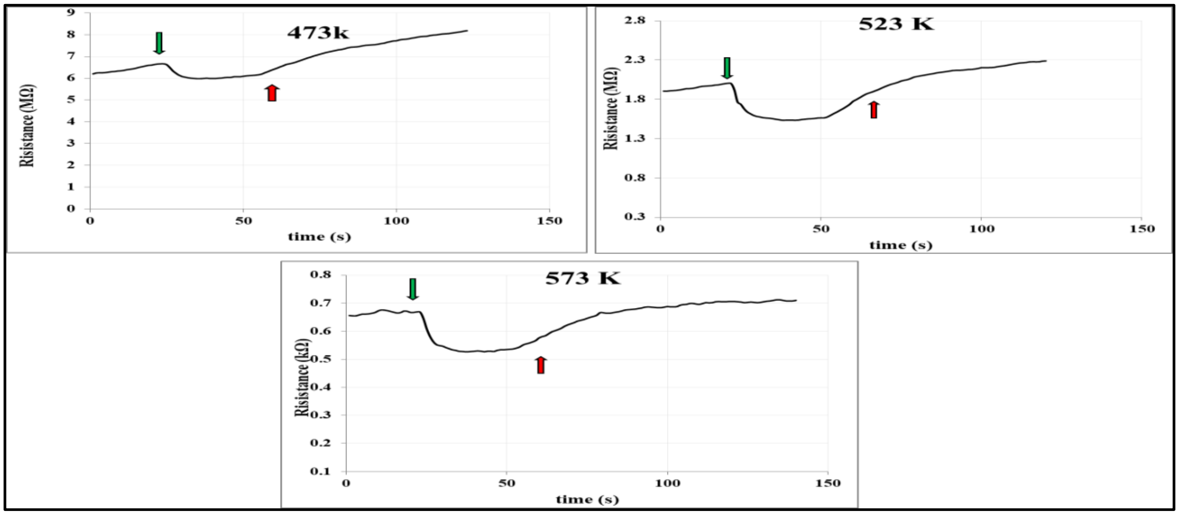

**Figure (4-37): Sample resistance change of PbS at laser energy (200 mJ) upon opening and closing of NO2 gas at (473,523,573)K**

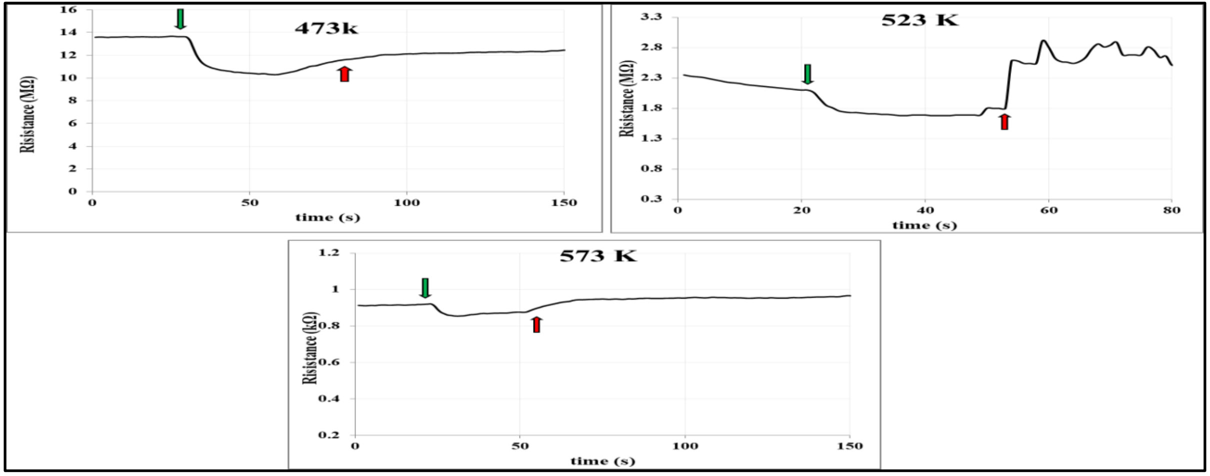

**Figure (4-38): Sample resistance change of PbS at laser energy (250 mJ) upon opening and closing of $NO_2$ gas at (473,523,573)K**

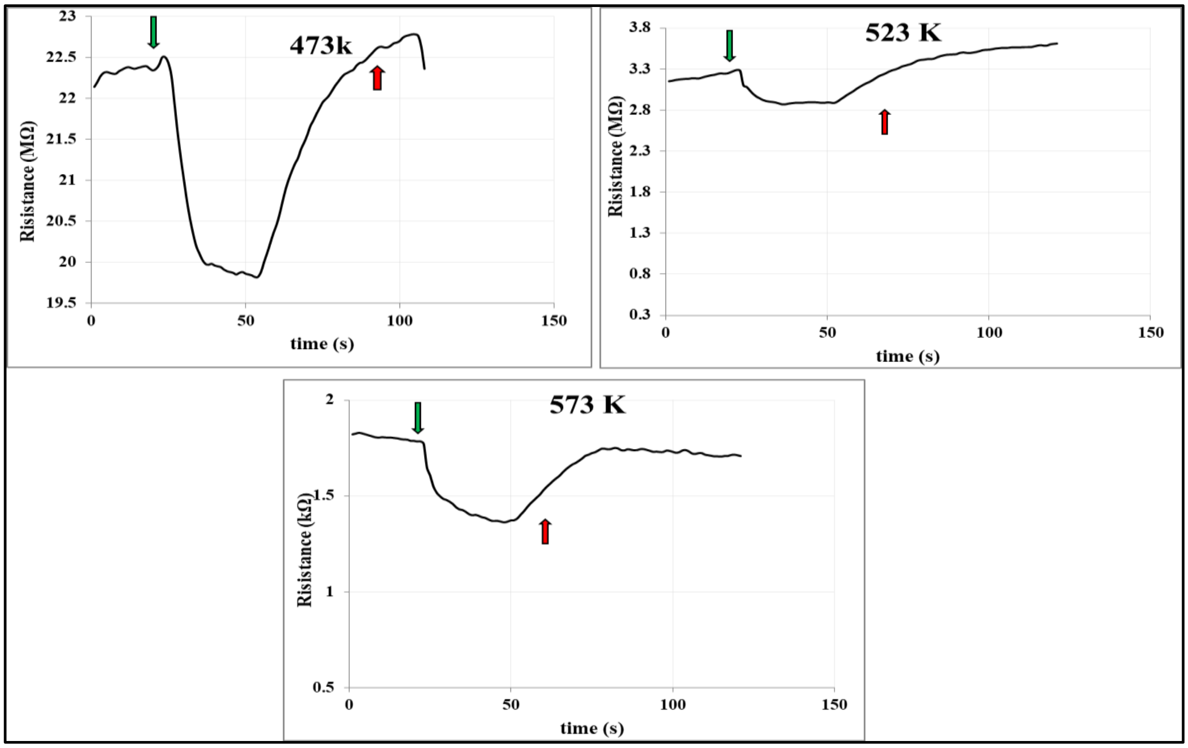

**Figure (4-39): Sample resistance change of PbS at laser energy (300 mJ) upon opening and closing of NO2 gas at (473,523,573)K**

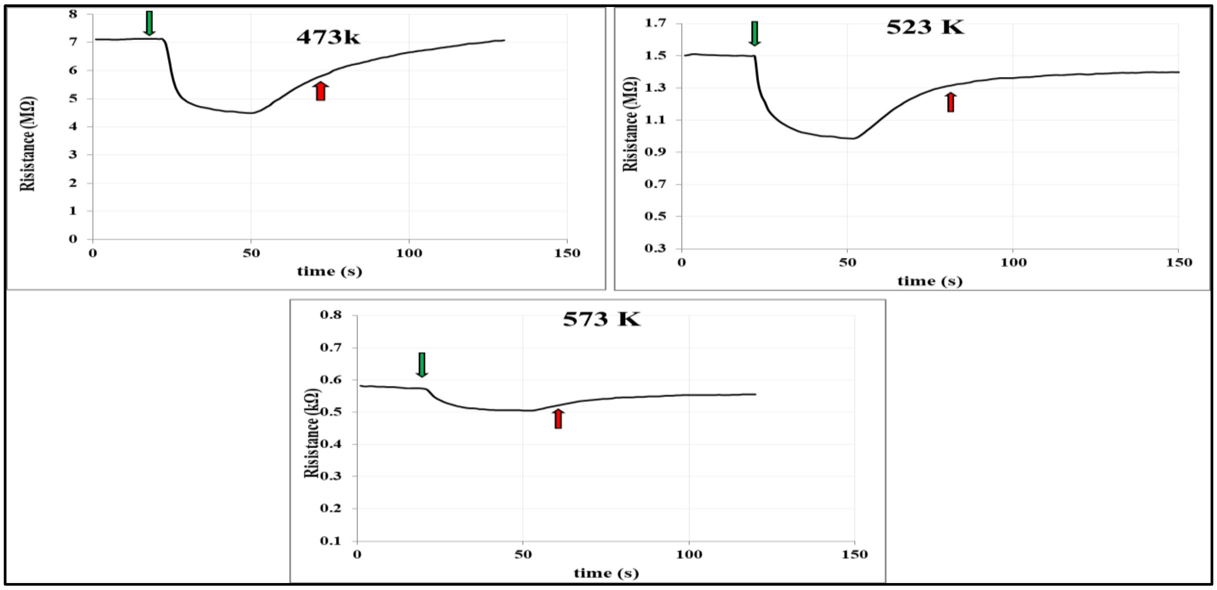

**Figure (4-40): Sample resistance change of PbS at laser energy (350 mJ) upon opening and closing of $NO_2$ gas at (473,523,573)K**

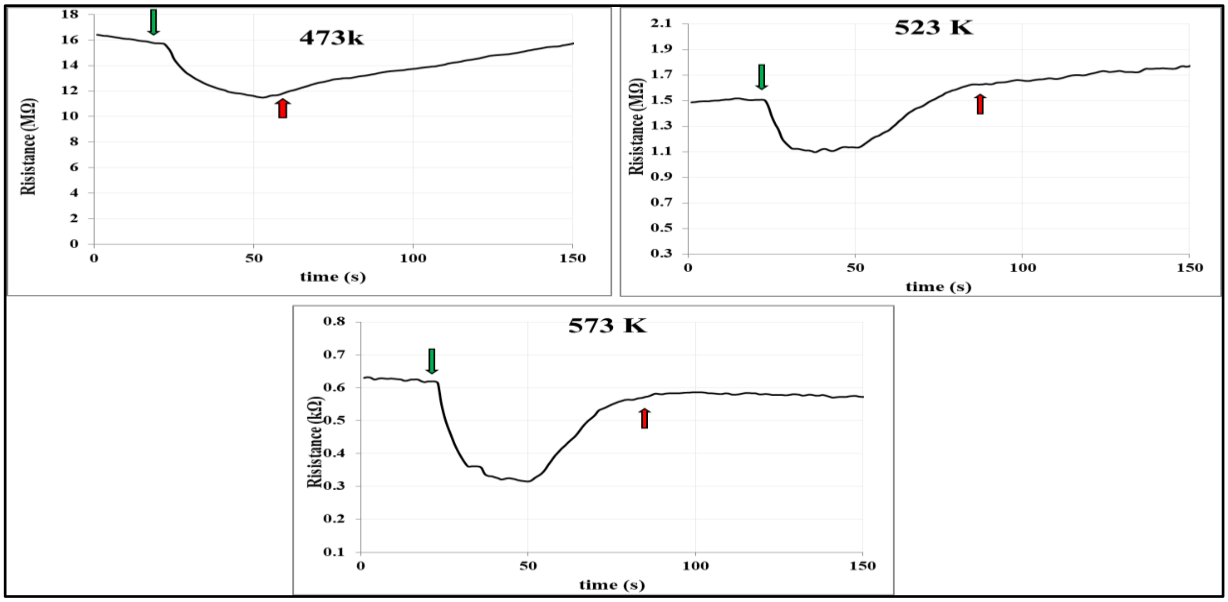

**Figure (4-41): Sample resistance change of PbS:Cd at doping ratio(X=2%) upon opening and closing of $NO_2$ gas at (473,523,573)K**

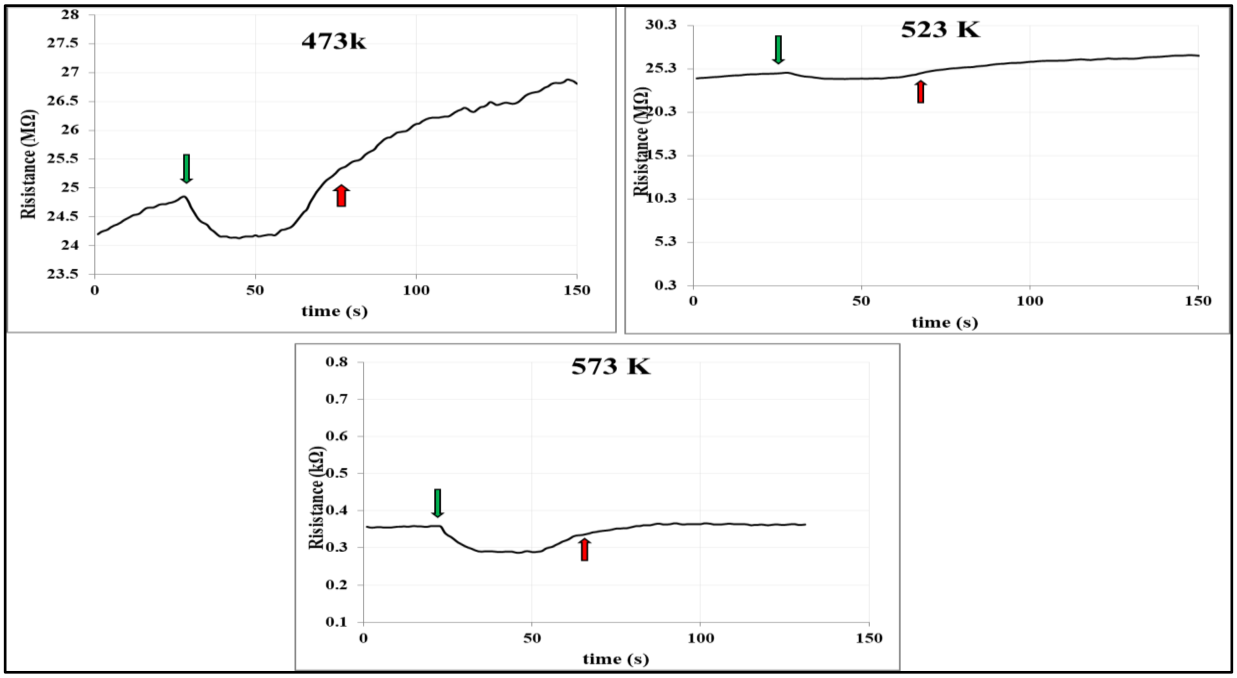

**Figure (4-42): Sample resistance change of PbS:Cd at doping ratio(X=4%) upon opening and closing of $NO_2$ gas at (473,523,573)K**

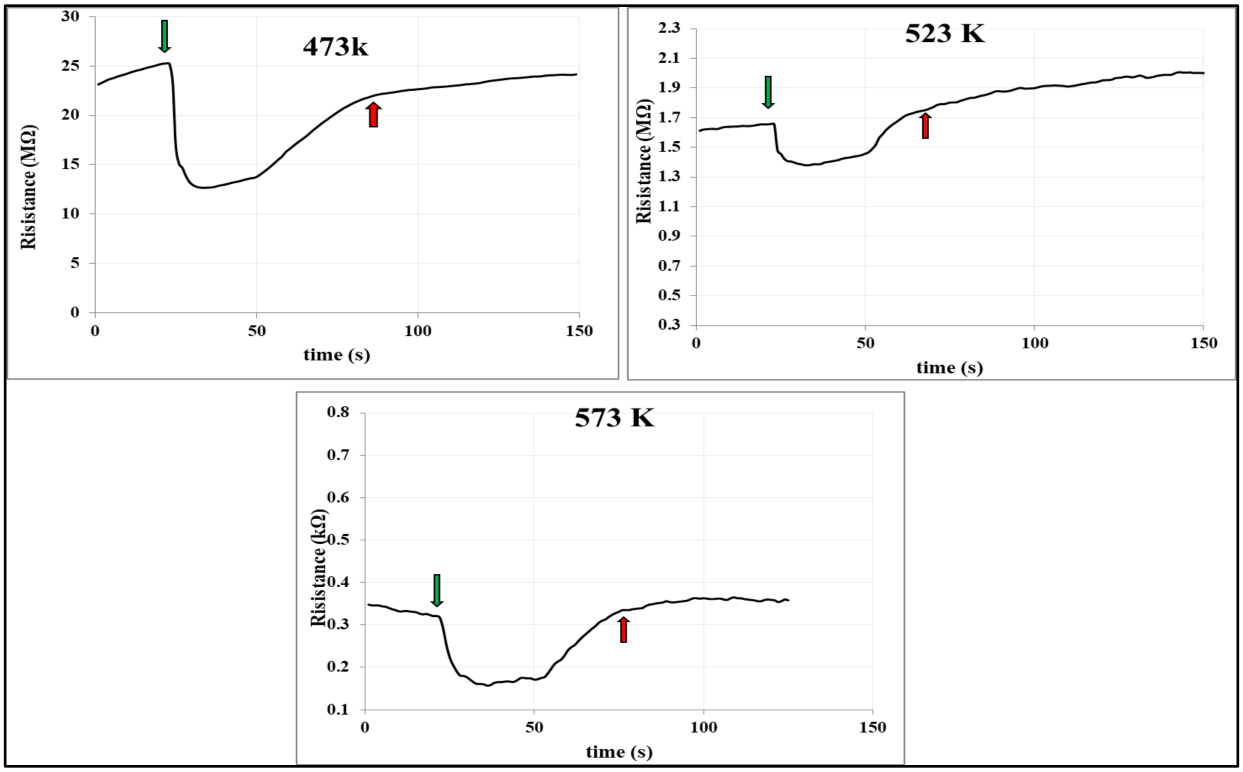

**Figure (4-43): Sample resistance change of PbS:Cd at doping ratio(X=6%) upon opening and closing of $NO_2$ gas at (473,523,573)K**

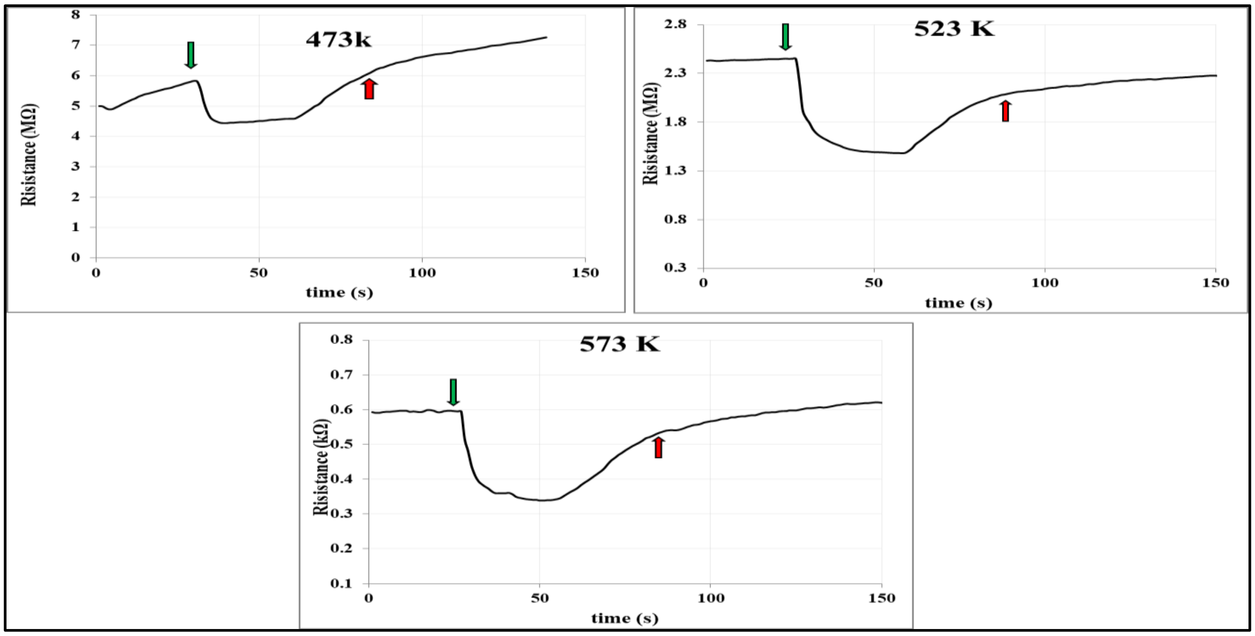

**Figure (4-44): Sample resistance change of PbS:Cr at doping ratio(X=2%) upon opening and closing of $NO_2$ gas at (473,523,573)K**

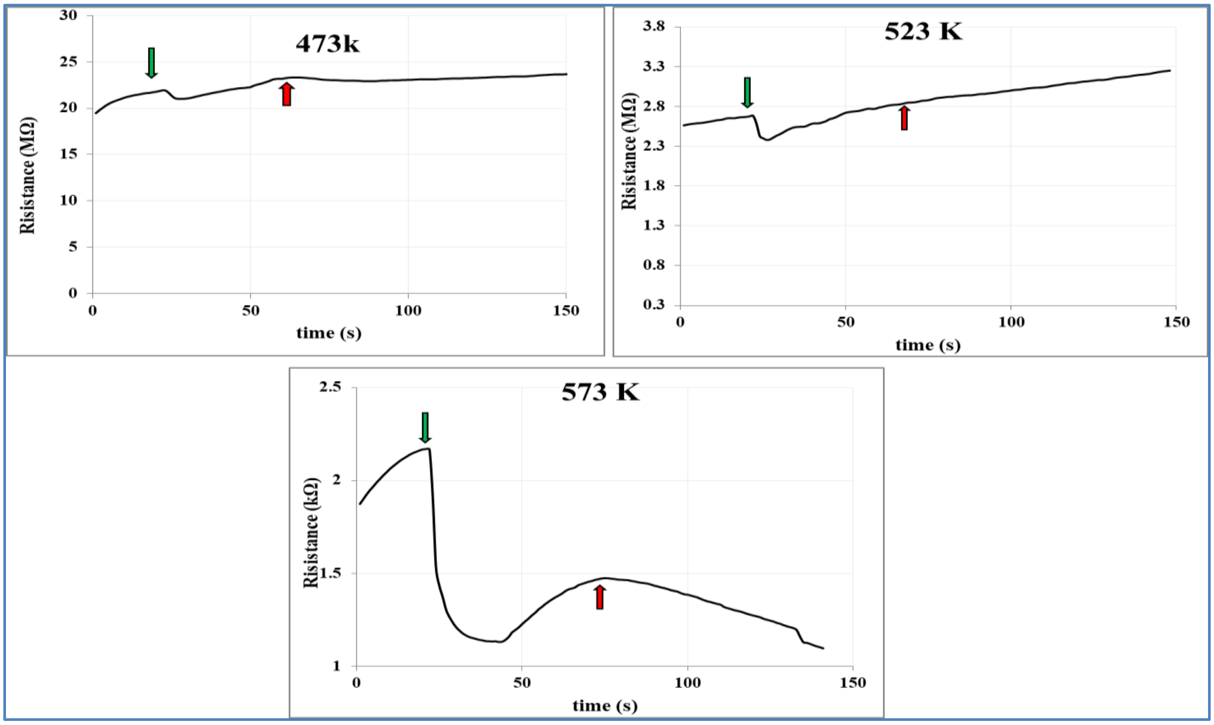

**Figure (4-45): Sample resistance change of PbS:Cr at doping ratio(X=4%) upon opening and closing of $NO_2$ gas at (473,523,573)K**

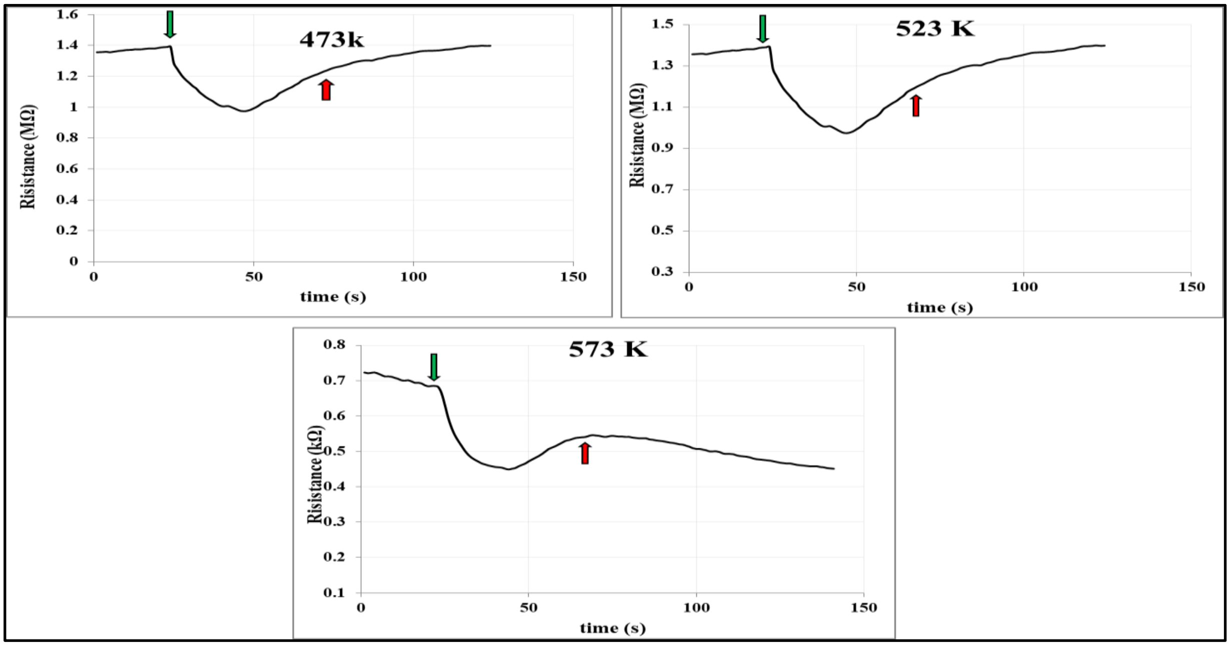

**Figure (4-46): Sample resistance change of PbS:Cr at doping ratio(X=6%) upon opening and closing of $NO_2$ gas at (473,523,573)K**

**Table (4-8) The sensing measurements data for PbS, PbS:Cd/p-Si and PbS:Cr/n-Si as oxidizing gas sensors($NO_2$).**

| Sample | Temp(K) | Sensitivity % | Response time (s) | Recovery time (s) |
|---|---|---|---|---|
| Pbs<br>E= 200 mJ | 473 | 9.774 | 14.4 | 55.8 |
| | 523 | 22.679 | 15.3 | 47.7 |
| | 573 | 21.076 | 12.6 | 48.6 |
| E= 250 mJ | 473 | 23.189 | 18.9 | 47.7 |
| | 523 | 19.811 | 12.6 | 50.4 |
| | 573 | 5.549 | 15.3 | 28.8 |
| E= 300 mJ | 473 | 11.644 | 19.8 | 49.5 |
| | 523 | 11.552 | 15.3 | 47.7 |
| | 573 | 22.755 | 19.8 | 43.2 |
| E= 350 mJ | 473 | 35.814 | 18 | 62.1 |
| | 523 | 32.733 | 18 | 54 |
| | 573 | 11.672 | 18.9 | 44.1 |
| Pbs:Cd<br>X= 2% | 473 | 26.012 | 25.2 | 64.8 |
| | 523 | 26.644 | 15.3 | 43.2 |
| | 573 | 47.325 | 18.9 | 48.6 |
| X= 4% | 473 | 80.440 | 21.6 | 65.7 |
| | 523 | 137.840 | 23.4 | 42.3 |
| | 573 | 18.941 | 14.4 | 42.3 |
| X=6% | 473 | 49.503 | 10.8 | 61.2 |
| | 523 | 16.253 | 9.9 | 62.1 |
| | 573 | 50.461 | 12.6 | 59.4 |
| Pbs:Cr<br>X= 2% | 473 | 22.530 | 15.3 | 49.5 |
| | 523 | 38.979 | 23.4 | 72.9 |
| | 573 | 42.713 | 20.7 | 65.7 |
| X= 4% | 473 | 3.775 | 28.8 | 88.2 |
| | 523 | 8.899 | 3.6 | 50.4 |
| | 573 | 46.922 | 14.4 | 57.6 |
| X=6% | 473 | 13.884 | 12.6 | 56.7 |
| | 523 | 28.478 | 20.7 | 59.4 |
| | 573 | 32.846 | 15.3 | 37.8 |

## 4-7 Conclusions

The structural, morphological, optical properties and gas sensor sensitivity of the cadmium-chromium-doped PbS thin films deposited on glass and silicon substrate with different laser energies and doping ratios prepared by PLD technique were studied. The main conclusions that can be drawn from this work are:

1- By studying the properties of cadmium and chromium saturated thin films deposited with PLD technique, it was found that the laser energy and the doping ratio were very effective in changing the properties of the films.

2- It was concluded that the increase in laser energy and doping ratios leads to an increase in films absorption, refractive index, extinction coefficient and optical energy bandgap.

3- The sensitivity of the gas sensor increases in most samples with increases laser energy and doping ratios for cadmium and chromium-doped PbS films.

## 4-8 Suggestions for Future works

1. Study of electrical and magnetic properties of cadmium and chromium-doped PbS films deposited on glass and silicon substrates.
2. Preparation and fabrication of PbS films as an IR detector.
3. Study of the effect of gamma -rays irradiation on the structural and optical properties of cadmium and chromium-doped PbS films prepared by PLD technique.
4. Study of the coordination of plasma generated during thin films deposition (PbS, PbS: Cd and PbS: Cr) PLD process using optical spectrometers.

# References

[1] D. J. Dahm, P. Horn, G. R. Johnson, M. G. Miles, and J. D. Wilson, “Classification of electrically conducting ‘electron-transfer’compounds by crystal structure,” J. Cryst. Mol. Struct., vol. 5, no. 1, pp. 27–34, 1975.

[2] S. S. AL-Rawi,S.J. Shakir and y. M. Hassan,“Solid state physics”, AlMousal University,(1990).

[3] B. H. Kear and G. Skandan, "Overview: status and current developments in nanomaterials," *International journal of powder metallurgy,* vol. 35, pp. 35-37, 1999.

[4] R. Zamiri, H. A. Ahangar, A. Zakaria, G. Zamiri, M. Shabani, B. Singh, "The structural and optical constants of Ag 2 S semiconductor nanostructure in the Far-Infrared," *Chemistry Central Journal,* vol. 9, p. 28, 2015.

[5] J. M. Hancock, W. M. Rankin, T. M. Hammad, J. S. Salem, K. Chesnel, and R. G. Harrison, "Optical and magnetic properties of ZnO nanoparticles doped with Co, Ni and Mn and synthesized at low temperature," *Journal of nanoscience and nanotechnology,* vol. 15, pp. 3809-3815, 2015.

[6] T. M. Hammad, J. K. Salem, S. Kuhn, N. M. A. Shanab, and R. Hempelmann, "Surface morphology and optical properties of PVA/PbS nanoparticles," *Journal of Luminescence,* vol. 157, pp. 88-92, 2015.

[7] N. Sinha, J. Ma, J.T. Yeow, Carbon nanotube-based sensors, Journal of nanoscience and nanotechnology, 6 (2006) 573-590

[8] K. Chopra, "Thin Film Phenomena MC Graw Hill Co," *New York, USA,* 1969.

[9] L. Eckertova, *Physics of thin films*: Springer Science & Business Media, 2012.

[10] D. R. Biswas, "Deposition processes for films and coatings," *Journal of materials science,* vol. 21, pp. 2217-2223, 1986.

[11] B. Lojek, *History of semiconductor engineering*: Springer, 2007.

[12] A. Obaid, M. Mahdi, Z. Hassan, and M. Bououdina, "Characterization of nanocrystalline PbS *Materials* ",assisted chemical bath deposition-ilms prepared using microwavethin f .,571-vol. 15, pp. 564 *,Science in Semiconductor Processing* 2012.

[13] H. R. Fallah, M. Ghasemi, A. Hassanzadeh, and H. Steki, “The effect of deposition rate on electrical, optical and structural properties of tin-doped indium oxide (ITO) films on glass at low substrate temperature,” *Phys. B Condens. Matter,* vol. 373, no. 2, pp. 274–279, 2006.

[14] S. J. Oh., “Designing high-performance PbS and PbSe nanocrystal electronic devices through stepwise, post-synthesis, colloidal atomic layer deposition,” *Nano Lett.*, vol. 14, no. 3, pp. 1559–1566, 2014.

[15] M. E. Weeks, “The discovery of the elements. VII. Columbium, tantalum, and vanadium,” *J. Chem. Educ.*, vol. 9, no. 5, p. 863, 1932.

[16] W. B. Jensen, “The place of zinc, cadmium, and mercury in the periodic table,” *J. Chem. Educ.*, vol. 80, no. 8, p. 952, 2003.

[17] A. Imbrie, “Roger Sessions: In Honor of His Sixty-fifth Birthday,” *Perspect. New Music*, pp. 117–147, 1962.

[18] L. F. Mondolfo, N. L. Parisi, and G. J. Kardys, “Interfacial energies in low melting point metals,” *Mater. Sci. Eng.*, vol. 68, no. 2, pp. 249–266, 1985.

[19] A. R. Chakhmouradian and F. Wall, “Rare earth elements: minerals, mines, magnets (and more),” *Elements*, vol. 8, no. 5, pp. 333–340, 2012.

[20] J. R. Huizenga, P. F. Grieger, and F. T. Wall, “Electrolytic Properties of Aqueous Solutions of Polyacrylic Acid and Sodium Hydroxide. I. Transference Experiments Using Radioactive Sodium1,” *J. Am. Chem. Soc.*, vol. 72, no. 6, pp. 2636–2642, 1950.

[21] A. Z. Miric and A. Grusd, “Lead-free alloys,” *Solder. Surf. Mt. Technol.*, 1998.

[22] S. V Vassilev and C. G. Vassileva, “A new approach for the combined chemical and mineral classification of the inorganic matter in coal. 1. Chemical and mineral classification systems,” *Fuel*, vol. 88, no. 2, pp. 235–245, 2009.

[23] H. Gladfelder, *Criminality and narrative in eighteenth-century England: Beyond the law*. JHU Press, 2001.

[24] W. Ensinger and M. Kiuchi, “Cubic nitrides of the sixth group of transition metals formed by nitrogen ion irradiation during metal condensation,” *Surf. Coatings Technol.*, vol. 84, no. 1–3, pp. 425–428, 1996.

[25] R. Wever and K. Kustin, “Vanadium: a biologically relevant element,” in *Advances in inorganic chemistry*, vol. 35, Elsevier, 1990, pp. 81–115.

[26] Y. R. Murthy, S. K. Tripathy, and C. R. Kumar, “Chrome ore beneficiation challenges & opportunities–A review,” *Miner. Eng.*, vol. 24, no. 5, pp. 375–380, 2011.

[27] L. Jorhem and B. Sundström, “Levels of lead, cadmium, zinc, copper, nickel, chromium, manganese, and cobalt in foods on the Swedish market, 1983–1990,” *J. food Compos. Anal.*, vol. 6, no. 3, pp. 223–241, 1993.

[28] J. Banhart, “Manufacture, characterisation and application of cellular metals and metal foams,” *Prog. Mater. Sci.*, vol. 46, no. 6, pp. 559–632, 2001.

[29] A. Agrawal, V. Kumar, and B. D. Pandey, “Remediation options for the treatment of electroplating and leather tanning effluent containing chromium—a review,” *Miner. Process. Extr. Metall. Rev.*, vol. 27, no. 2, pp. 99–130, 2006.

[30] M. M. Abbas, A. A.-M. Shehab, N. A. Hassan, and A. K. Al-Samuraee, “Effect of temperature and deposition time on the optical properties of chemically deposited nanostructure PbS thin films,” Thin Solid Films, vol. 519, no. 15, pp. 4917–4922, 2011.

[31] S. B. Pawar “Facile and low cost chemosynthesis of nanostructured PbS with tunable optical properties,” Appl. Surf. Sci., vol. 258, no. 5, pp. 1869–1875, 2011.

[32] S. Bandyopadhyay, “Performance of nanocrystalline PbS gas sensor with improved cross-sensitivity,” Part. Sci. Technol., vol. 30, no. 1, pp. 43–54, 2012.

[33] R. Das and R. Kumar, “Preparation of nanocrystalline PbS thin films and effect of Sn doping and annealing on their structural and optical properties,” Mater. Res. Bull., vol. 47, no. 2, pp. 239–246, 2012.

[34] S. I. Sadovnikov and A. I. Gusev, “Structure and properties of PbS films,” J. Alloys Compd., vol. 573, pp. 65–75, 2013.

[35] A. S. Obaid, M. A. Mahdi, Y. Yusof, M. Bououdina, and Z. Hassan, “Structural and optical properties of nanocrystalline lead sulfide thin films prepared by microwave-assisted chemical bath deposition,” Mater. Sci. Semicond. Process., vol. 16, no. 3, pp. 971–979, 2013.

[36] F. Göde, E. Güneri, F. M. Emen, V. E. Kafadar, and S. Ünlü, “Synthesis, structural, optical, electrical and thermoluminescence properties of chemically deposited PbS thin films,” J. Lumin., vol. 147, pp. 41–48, 2014.

[37] R. Kumar, R. Das, M. Gupta, and V. Ganesan, “Preparation of nanocrystalline Sb doped PbS thin films and their structural, optical, and electrical characterization,” Superlattices Microstruct., vol. 75, pp. 601–612, 2014.

[38] R. N. Bharathi and S. Sankar, "Mg doping effects on the physical properties of lead sulphide thin films," Int. J. ChemTech Res, vol. 7, pp. 980-986, 2015

[39] C. Rajashree, A. R. Balu, and V. S. Nagarethinam, “Properties of Cd doped PbS thin films: doping concentration effect,” Surf. Eng., vol. 31, no. 4, pp. 316–321, 2015.

[40] E. Nasir and M. Abass, "Characterization, Morphology and Electrical Properties of Chemically Deposited Nanocrystalline PbS/Si Heterojunction Thin Films," Chalcogenide Letters, vol. 13, pp. 271-279, 2016.

[41] B. Touati, A. Gassoumi, I. Dobryden, M. M. Natile, A. Vomiero, and N. K. Turki, “Engineering of electronic and optical properties of PbS thin films via Cu doping,” Superlattices Microstruct., vol. 97, pp. 519–528, 2016.

[42] E. Yücel and Y. Yücel, “Fabrication and characterization of Sr-doped PbS thin films grown by CBD,” Ceram. Int., vol. 43, no. 1, pp. 407–413, 2017.

[43] O. A. Carrasco-Jaim, O. Ceballos-Sanchez, L. M. Torres-Martínez, E. Moctezuma, and C. Gómez-Solís, “Synthesis and characterization of PbS/ZnO thin film for photocatalytic hydrogen production,” J. Photochem. Photobiol. A Chem., vol. 347, pp. 98–104, 2017.

[44] D. Kumar, S. Chaudhary, and D. K. Pandya, “Fabrication of PbS quantum dots and their applications in solar cells based on ZnO nanorod arrays,” in AIP Conference Proceedings, 2018, vol. 1953, no. 1, p. 30038.

[45] B. Abdallah, A. Ismail, H. Kashoua, and W. Zetoun, "Effects of deposition time on the morphology, structure, and optical properties of PbS thin films prepared by chemical bath deposition," Journal of Nanomaterials, vol. 2018, 2018.

[46] Ö. Şahin, A. Ekinci, and S. Horoz, "Synthesis of PbS: Mo (3%) thin film and investigation of its properties," Journal of Materials Science: Materials in Electronics, vol. 30, pp. 7600-7605, 2019

[47] J. Huo, W. Li, and T. Wang, "Effect of Cr doping concentration on the structural, optical, and electrical properties of lead sulfide (PbS) nanofilms," Coatings, vol. 9, p. 376, 2019.

[48] F. Mitri, A. De Iacovo, M. De Luca, A. Pecora, and L. Colace, “Lead sulphide colloidal quantum dots for room temperature NO 2 gas sensors,” Sci. Rep., vol. 10, no. 1, pp. 1–9, 2020.

[49] E. J. Mohammed, A. K. Abbas, and K. A. Aadim, “Pulsed laser deposition to investigate structural and optical properties of lead sulfide nanostructure,” Iraqi J. Phys., vol. 18, no. 47, pp. 21–32, 2020.

[50] O. G. Schmidt and K. Eberl, “Thin solid films roll up into nanotubes,” Nature, vol. 410, no. 6825, p. 168, 2001.

[51] A. Jilani, M. S. Abdel-Wahab, and A. H. Hammad, “Advance deposition techniques for thin film and coating,” Mod. Technol. Creat. Thin-film Syst. Coatings, vol. 2, pp. 137–149, 2017.

[52] K. Seshan and D. Schepis, Handbook of thin film deposition. William Andrew, 2018.

[53] C. Kisielowski “Strain-related phenomena in GaN thin films,” Phys. Rev. B, vol. 54, no. 24, p. 17745, 1996.

[54] K. Seshan and D. Schepis, *Handbook of thin film deposition*. William Andrew, 2018.

[55] C. Kisielowski., “Strain-related phenomena in GaN thin films,” *Phys. Rev. B*, vol. 54, no. 24, p. 17745, 1996.

[56] H.-U. Krebs “Pulsed laser deposition (PLD)--a versatile thin film technique,” in *Advances in Solid State Physics*, Springer, 2003, pp. 505–518.

[57] R. Eason, *Pulsed laser deposition of thin films: applications-led growth of functional materials*. John Wiley & Sons, 2007.

[58] K. A. Aadim, A. E. Ibrahim, and Q. A. Abduljabbar, “Optical and Electrical Properties of (SnO2) X (In2O3) thin Films Prepared by Pulse Laser Deposition,” *Int. J. Phys.*, vol. 5, no. 4, pp. 116–120, 2017.

[59] R. E. Hummel, *Understanding materials science: history, properties, applications*: Springer Science & Business Media, 2004.

[60] B. G. Streetman and S. Banerjee, *Solid state electronic devices* vol. 4: Prentice Hall Englewood Cliffs, NJ, 1995.

[61] B. G. Streetman and S. K. Benerjee**,** “Solid State Electronic Devices”, Pearson Education, 6th edition, (2006).

[62] S.O. Kasap, “Principles of Electronic Materials and Devices”, McGraw Hill, 2nd edition, (2002

[63] B. Holt, “The growth and structure of epitaxial films and heterojunctions of II–VI compounds”, Thin Solid Films, vol. 24, pp. 167, (1974).

[64] R. E. Hummel, *Understanding materials science: history, properties, applications*: Springer Science & Business Media, 2004.

[65] B. G. Streetman and S. Banerjee, *Solid state electronic devices*, vol. 4. Prentice hall Englewood Cliffs, NJ, 1995.

[66] S. M. Sze and K. K. Ng, *Physics of semiconductor devices*. John wiley & sons, 2006.

[67] C. Kittel, P. McEuen, and P. McEuen, *Introduction to solid state physics*, vol. 8. Wiley New York, 1996.

# References

[68] C. H. Kwon "Thick-film zinc-oxide gas sensor for the control of lean air-to-fuel ratio in domestic combustion systems," *Sensors Actuators B Chem.*, vol. 25, no. 1–3, pp. 610–613, 1995.

[69] R. Sanderson, "Chemical Periodicity, Reinhold Pub," *Corp., New York,* p. 24, 1960.

[70] D. R. Askeland, P. P. Fulay, and W. J. Wright, *The science and engineering of materials*: Nelson Education, 2011.

[71] W. Jones and N. H. March, *Theoretical Solid State Physics: Perfect Lattices in Equilibrium* vol. 1: Courier Corporation, 1985.

[72] A. Guinier and D. Sainte-Marie Lorrain, "X-ray Crystallography.(Book Reviews: X-Ray Diffraction in Crystals, Imperfect Crystals, and Amorphous Bodies)," *Science,* vol. 142, p. 1564, 1963.

[73] P. J. Goodhew, J. Humphreys, and R. Beanland, *Electron microscopy and analysis*: CRC Press, 2014.

[74] W. H. Bragg and W. L. Bragg, *X-rays and Crystal Structure*: G. Bell and sons, Limited, 1918.

[75] D. Halliday, J. Walker, and R. Resnick, *Fundamentals of physics*: John Wiley & Sons, 2013.

[76] C. Kittel, "Introduction to Solid State Physics, 7th edn., Chapter 15," ed: John Wiley & Sons (Asia) Pte. Ltd., Singapore, 1995.

[77] A. L. Patterson, "The Scherrer formula for X-ray particle size determination," *Phys. Rev.*, vol. 56, no. 10, p. 978, 1939.

[78] D. A. Neamen, *Semiconductor physics and devices: basic principles*: New York, NY: McGraw-Hill, 2012.

[79] C. Hogarth and M. Nadeem, "The optical absorption edge in amorphous thin films of germania and of germania with barium oxide," *physica status solidi (a),* vol. 68, pp. K181-K184, 1981.

[80] G. Busch, H. Schade, and J. L. Birman, "Lectures on Solid State Physics," *Physics Today,* vol. 32, p. 74, 1979.

# References

[81] M. Yan, M. Lane, C. Kannewurf, and R. P. Chang, "Highly conductive epitaxial CdO thin films prepared by pulsed laser deposition," *Applied Physics Letters,* vol. 78, pp. 2342-2344, 2001.

[82] F. Wooten, *Optical properties of solids*. Academic press, 2013.

[83] Y. U. Peter and M. Cardona, *Fundamentals of semiconductors: physics and materials properties*. Springer Science & Business Media, 2010.

[84] J. Martín-Sánchez "Strain-tuning of the optical properties of semiconductor nanomaterials by integration onto piezoelectric actuators," *Semicond. Sci. Technol.*, vol. 33, no. 1, p. 13001, 2017.

[85] D. K. Ferry, *Semiconductors*. Macmillan New York, 1991.

[86] K. Segger, "Semiconductors Physics", Springer-Verlag Wien (1973).

[87] W. C. Dickinson and P. N. Cheremisinoff, "Solar energy technology handbook. Part B-Applications, systems design, and economics," in *New York, Marcel Dekker, Inc.(Energy, Energy, and Environment. Volume 6), 1980. 817 p,* 1980.

[88] A. Fahrenbruch and R. Bube, *Fundamentals of solar cells: photovoltaic solar energy conversion*. Elsevier, 2012.

[89] J. Parkove, "Optical process in semiconductors," ed: Dover Publications Inc, New York, 1971.

[90] R. Levy, *Principles of solid state physics*. Elsevier, 2012.

[91] J. Bardeen, F. Blatt, and L. Hall, "Photoconductivity conference," *Wiley, New York,* vol. 195623, p. 146, 1956.

[92] G. Burns, "Solid State Physics Academic Press Inc," *New York*, 1985.

[93] K. Chopra, *Thin film device applications*. Springer Science & Business Media, 2012.

[94] A. Clark, "Polycrystalline and amorphous thin films and devices," *Academic Press, NY,* 1980.

[95] C. W. Frank, *Organic Thin Films: Structure and Applications*: Amer Chemical Society, 1998.

[96] R. H. French, H. Müllejans, and D. J. Jones, "Optical properties of aluminum oxide: determined from vacuum ultraviolet and electron energy-loss spectroscopies," *Journal of the American Ceramic Society,* vol. 81, pp. 2549-2557, 1998.

[97] J. Banhart, *Advanced tomographic methods in materials research and engineering* vol. 66: Oxford University Press, 2008.

[98] R. S. Popovic, *Hall effect devices: magnetic sensors and characterization of semiconductors*: CRC Press, 2003.

[99] E. Contés-de Jesús, J. Li, and C. R. Cabrera, "Latest advances in modified/functionalized carbon nanotube-based gas sensors," *Synth. Appl. Carbon Nanotub. Their Compos.*, pp. 337–366, 2013.

[100] K. G. Ong, K. Zeng, and C. A. Grimes, "A wireless, passive carbon nanotube-based gas sensor," *IEEE Sens. J.*, vol. 2, no. 2, pp. 82–88, 2002.

[101] K. Dew, *"Gas Sensing Using Mononuclear and Binuclear Phthalocyanine Films,"*

(2012).

[102] A. A. Ramadhan, *"Characterization of CuPcTs/PEDOT:PSS, Alq3 Bulk Heterojunction Blend for Sensor Application"*, Ph. D. Thesis, Baghdad university, (2017).

[103] G. Korotcenkov, "Handbook of gas sensor materials," *Vol. 1 Conv. Approaches*, 2013.

[104] B. Maniscalco, P. M. Kaminski, and J. M. Walls, "Thin film thickness measurements using scanning white light interferometry," *Thin Solid Films*, vol. 550, pp. 10–16, 2014.

[105] R. K. Jamal, M. A. Hameed, and K. A. Adem, "Optical properties of nanostructured ZnO prepared by a pulsed laser deposition technique," *Mater. Lett.*, vol. 132, pp. 31–33, 2014.

[106] M. Chougule, S. Nalage, S. Sen, V. Patil, Development of nanostructured ZnO thin film sensor for NO2 detection, Journal of Experimental Nanoscience, 9 (2014) 482-490.

[107] C. Rajashree, A. R. Balu, and V. S. Nagarethinam, "Properties of Cd doped PbS thin films: doping concentration effect," Surf. Eng., vol. 31, no. 4, pp. 316–321, 2015.

[108] A. M. Ahmed, M. Rabia, and M. Shaban, "The structure and photoelectrochemical activity of Cr-doped PbS thin films grown by chemical bath deposition," RSC Adv., vol. 10, no. 24, pp. 14458–14470, 2020.

[109] J. J. Valenzuela-Jauregui, R. Ramırez-Bon, A. Mendoza-Galvan, and M. Sotelo-Lerma, "Optical properties of PbS thin films chemically deposited at different temperatures," Thin Solid Films, vol. 441, no. 1–2, pp. 104–110, 2003.

[110] K. Aadim, A. Ibrahim, and J. Marie, "Structural and optical properties of PbS thin films deposited by pulsed laser deposited (PLD) technique at different annealing temperature," Int. J. Phys., vol. 5, no. 1, pp. 1–8, 2017.

[111] Y. Liu , "ppb level ammonia detection of 3-D PbS quantum dots/reduced graphene oxide nanococoons at room temperature and Schottky barrier modulated behavior," *Sensors*

*Actuators B Chem.*, vol. 255, pp. 2979–2987, 2018.

[112] T. V Beatriceveena, E. Prabhu, A. S. R. Murthy, V. Jayaraman, and K. I. Gnanasekar, “Highly selective PbS thin film based ammonia sensor for inert ambient: In-situ Hall and photoelectron studies,” *Appl. Surf. Sci.*, vol. 456, pp. 430–436, 2018.

[113] P. Sun, X. Zhou, C. Wang, B. Wang, X. Xu, and G. Lu, “One-step synthesis and gas sensing properties of hierarchical Cd-doped SnO2 nanostructures,” *Sensors Actuators B Chem.*, vol. 190, pp. 32–39, 2014.

[114] G. K. Mani and J. B. B. Rayappan, “A highly selective and wide range ammonia sensor—Nanostructured ZnO: Co thin film,” *Mater. Sci. Eng. B*, vol. 191, pp. 41–50, 2015.

[115] C. S. Rout, M. Hegde, A. Govindaraj, and C. N. R. Rao, “Ammonia sensors based on metal oxide nanostructures,” *Nanotechnology*, vol. 18, no. 20, p. 205504, 2007.

[116] S. S. Kim, H. G. Na, H. W. Kim, V. Kulish, and P. Wu, “Promotion of acceptor formation in SnO 2 nanowires by e-beam bombardment and impacts to sensor application,” *Sci. Rep.*, vol. 5, no. 1, pp. 1–12, 2015.

[117] C. Wang, L. Yin, L. Zhang, D. Xiang, and R. Gao, “Metal oxide gas sensors: sensitivity and influencing factors,” *sensors*, vol. 10, no. 3, pp. 2088–2106, 2010.

# الخلاصة

في هذا العمل ، تم ترسيب الأغشية الرقيقة PbS المطعمة بالكادميوم والكروميوم (X=2,4,6) Wt% على قاعدة زجاجية في درجة حرارة الغرفة بواسطة تقنية الترسيب بالليزر النبضي. تم دراسة تأثير زيادة طاقة الليزر ونسب التطعيم على الخصائص التركيبية والبصرية لأغشية pbs باستخدام الليزر Nd:YAG ذو طاقات ليزر مختلفة من (200-350) ملي جول بزياده 50 ملي جول لكل خطوة. ضبطت نبضات الليزر بشكل ثابت على 100 نبضة لكل عينة.

تم دراسة تراكيب مسحوق(PbS) (PbS: Cd , PbS: Cr) الأغشية الرقيقة باستخدام تقنية حيود الأشعة السينية .حيث أظهرت دراسة الأشعة السينية أن الهيكل متعدد البلورات وأحادي الميل مع مستوى اتجاه مفضل (200) وأن حجم البلورة يزداد مع زيادة طاقة الليزر وزيادة نسبة التطعيم .

أكدت القياسات المجهرية للقوة الذرية (AFM) أن الأغشية تمت ترسيبها بتقنية PLD لها سطح بلوري جيد ومتجانس. وبلغ متوسط قطر الجسيمات لجميع الأفلام المعدة أقل من 100 نانومتر ، لذا فهو يقع ضمن نطاق المواد النانوية.

اجريت القياسات البصرية باستخدام مقياس الطيف الضوئي UV-ViS ، حيث أظهرت النتائج أن الأغشية الرقيقة (PbS) ، (PbS:Cr) (PbS: Cd)لها انتقال مباشر لفجوة الطاقة وزيادة امتصاص الأغشية مع زيادة طاقة الليزر ونسب التطعيم. كما تم حساب الثوابت البصرية مثل معامل الانكسار (n) ومعامل الامتصاص (α)ومعامل الخمود (k) وثابت العزل الكهربائي للجزء الحقيقي والخيال( $\varepsilon_i$ , $\varepsilon_r$ )، .اما فجوة الطاقة فأنها تزداد مع زيادة طاقة الليزر وزيادة نسبة التطعيم (1.5 - 2.8) الكترون-فولت عن طريق التطعيم بالكادميوم و (1.6 - 1.8) الكترون-فولت عن طريق التطعيم بالكروم.

أظهرت قياسات مستشعر الغاز أن أفضل مستشعر لغاز $NO_2$ كان للعينة بنسبة 5٪ (PbS: Cd) X = 4% مع حساسية( 137%) عند 523كلفن وانخفضت حساسية العينة PbS وغاز $NH_3$ وطاقة ليزر 250 ملي جول عند درجة حرارة 523 كلفن إلى 19٪.

جمهورية العراق

وزارة التعليم العالي والبحث العلمي

جامعة كربلاء- كلية العلوم

قسم الفيزياء

# تحضير وتوصيف أغشية كبريتيد الرصاص المطعمة بالكادميوم والكروم بطريقة الترسيب بالليزر النبضي لتطبيقات المتحسس الغازي

رسالة تقدم بها

**خضير عبيس محمود**

**بكالوريوس في علوم الفيزياء (2010-2011)**

**الى مجلس كلية العلوم في جامعة كربلاء وهي جزء من متطلبات نيل درجة**

**ماجستير في علوم الفيزياء**

**بإشراف**

**أ.م. د. ماجد حسين دويج** **أ. د. كاظم عبد الواحد عادم**

**1443هـ** **2021 م**